Università degli Studi di Cagliari

Facoltà di Ingegneria

D.I.Me.Ca.

Dottorato di Ricerca in Ingegneria Industriale

XIX Ciclo

Numerical Simulations of the Atmospheric Boundary Layer

Giorgio Crasto

TUTOR	**COORDINATORE DEL CICLO**
Prof. Pierpaolo Puddu	Prof.ssa Alessandra Fanni

Cagliari, Febbraio 2007

TABLE OF CONTENTS

RINGRAZIAMENTI (ANKNOWLODGEMENTS)

Vorrei ringraziare il gruppo di lavoro di cui ho fatto parte nel dipartimento di meccanica dell'Università di Cagliari per il supporto datomi in questi anni. Prima di tutto Prof. Mandas che mi ha introdotto nel campo della fluidodinamica sperimentale e dell'energia eolica, sin dai tempi dell'ultimo anno del corso di laurea e come relatore del lavoro di tesi di laurea.

Sono particolarmente riconoscente nei confronti dell'Ing. Cambuli, che mi ha strettamente seguito durante il lavoro svolto. I mei colleghi, in particolare Giorgio Melis, Carlo Enrico Carcangiu, Roberto Fuliotto e Marco Pau, ovvero il CFD Group, con cui ho avuto la fortuna e il piacere di lavorare ma anche di condividere momenti importanti di questi anni. Ringrazio inoltre il mio tutor, il Prof. Puddu, sempre pronto ad ascoltarer e dare preziosi consigli in merito alle attività di dottorato.

Fase intensa delle attività svolte è stata durante il Diplome Course 2005-06 presso il von Karman Institute. Vorrei ringraziare tutti i giovani ingegneri che anno preso parte al corso e soprattutto quelli che mi hanno sostenuto in maniera fraterna e con cui ho convissuto questi intensi mesi: Marco Pau (ancora lui!), Emmett Dempsey, Javier Gonzalez Castano, Julien Bodart, Domenico Verrastro, Filippo Coletti, Flora Tomasoni, Anna Müeller, Valentina Taviani, Mike Bilka, Gökhan Balik e inoltre Alessandro Gambale e Raf Theunissen.

Il lavoro presso il VKI non sarebbe stato inoltre possibile senza la supervisione del Prof. Carlo Benocci e di Patrick Rambaud.

I would like to thanks the cheerful and welcoming people I found in Norway at the Vector A.S.. Arne Reidar Gravdahl, Tine Vølstad and her husband Asbjørn with the kids, and Andrea Vignaroli, my housemate and colleague. All of them made the permanence in Norway pleasant and unforgettable. I wish to thank also Arancha Pera Gilaberte that I met only for few days in Norway but that showed to be a very good friend in the following months.

I wish to thank also Prof. Peter Taylor and collaborators who provided the experimental data of the Askervein hill project with the orography maps.

Un particolare ringraziamento va alla mia famiglia: Carlo, Paola ed i miei genitori Antonio e Giuseppina che continuano a sostenermi giornalmente e a credere in certe mie presunte potenzialità.

NOMENCLATURE

Roman

B		constant (~5,45) in the logarithmic law, equation (2.31)
C		proportionality constant, equation (1.2)
C_w, C_{w2}, C_{w3}, C_{b1}, C_{b2}, C_{prod}		parameters of the SA model
C_S		Smagorinsky constant; roughness constant in modeling of boundary layer over rough surfaces
C_μ, $C_{1\varepsilon}$, $C_{2\varepsilon}$		k-ε model's constants
C_{DES}		DES model's constant
C1	[s^{-1}]	drag coefficient of momentum source term proportional to velocity
C2	[m^{-1}]	drag coefficient of momentum source term proportional to the square of velocity
$\tilde{d}$	[m]	modified wall distance in SA based DES model, equation (2.29)
d	[m]	wall distance; displacement length in forest modeling according to equation (6.2)
d_f	[m]	displacement length of the florest floor according to sketch of Figure 6.1
E	[-]	constant (= $\exp(\kappa B) \simeq 9{,}81$)
f		Coriolis parameter $2\pi\Omega\sin\phi$
f_i, F_i	[m s^{-2}]	specific force in x_i direction
f_{v1}, f_{v2}, f_w		parameters of the SA model
k	[m^2 s^{-2}]	turbulent kinetic energy (TKE)
g	[-]	parameter of the SA model
G		filter function
G_ν	[kg m^{-1} s^{-2}]	production term (SA model) in equation (2.8)
G_k, G_b	[kg m^{-1} s^{-3}]	production of TKE due to the mean velocity gradients and buoyancy

G_ω	[kg m^{-3} s^{-2}]	production term of ω in the ω transport equation (k-ω model), equation (2.13)
h	[m]	height of wall adjacent cell
$\overline{h}$, h_C	[m]	height of the canopy
H	[m]	height of an isolated hill
K_S^+		normalized
K_S	[m]	roughness elements' size (equivalent sand)
ℓ_S	[m]	length scale in the eddy viscosity models
L	[m]	half width of the hill measured at half height H/2
L_S	[m]	mixing length in the SGS eddy viscosity definition, equation (2.24)
L_x, L_y	[m]	length of the computational domain in x, y directions
N		total number of cells in a computational grid
N_x, N_y		number of subdivisions of a computational grid in the x and y directions
$\overline{p}$	[Pa]	space filtered pressure
r		parameter of the SA model
S	[s^{-1}]	module of the rate-of-strain tensor, equation (2.26)
S_ω	[kg m^{-3} s^{-2}]	source term of ω in the ω transport equation (k-ω model), equation (2.13)
$\tilde{S}$	[s^{-1}]	modified S (SA model)
$\overline{S_{ij}}$	[s^{-1}]	rate-of-strain tensor for resolved scale, equation (2.25)
t	[s]	time
u*, u_τ	[m s^{-1}]	friction velocity
u_i	[m s^{-1}]	velocity along the Cartesian coordinate x_i
u,v,w	[m s^{-1}]	velocities along the Cartesian axes x, y, z
u^+, y^+		wall coordinates
U, V, W	[m s^{-1}]	time averaged velocities along the Cartesian axes x, y, z
V	[m^3]	volume of a general cell
V_S	[m s^{-1}]	velocity scale for eddy-viscosity models
x_i	[m]	Cartesian coordinates

x, y, z	[m]	Cartesian coordinates
x	[m]	position vector
Y_ω	[kg m^{-3} s^{-2}]	dissipation term of ω in the ω transport equation (k-ω model), equation (2.13)
Y_ν	[kg m^{-1} s^{-2}]	destruction term of $\tilde{\nu}$, (SA model) equation (2.8)
z_0	[m]	roughness length
z_{0f}	[m]	roughness length of the forest floor, according to sketch in Figure 6.1
z_h	[m]	gradient's height (or height of the ABL)

Greek

α		expansion ratio in a computational grid
α	[m^2]	permeability
α^*		k-ω model's parameter
β		volume porosity
β_S		surface porosity
Γ_k, Γ_ω		diffusive coefficient for k and ω in the k-ω model
δ_{ij}		Kronecker delta
Δ	[m]	length scale used in the modification of wall distance $\tilde{d}$
ΔB		shift of u^+ in the modified logarithmic law for rough surfaces (2.32)
Δx, Δy, Δz	[m]	resolution of a mesh in the x, y, z directions
ε	[m^2 s^{-3}]	dissipation rate of turbulent kinetic energy (TDR)
κ		von Karman constant (~0,42)
μ	[Pa s]	dynamic viscosity
μ_t	[Pa s]	turbulent (or eddy) dynamic viscosity, SGS turbulent (or eddy) dynamic viscosity
μ_{t-sgs}	[m^2 s^{-1}]	SGS dynamic eddy-viscosity
ν	[m^2 s^{-1}]	kinematic viscosity
$\tilde{\nu}$	[m^2 s^{-1}]	modified eddy viscosity in the SA model
ν_{t-sgs}	[m^2 s^{-1}]	SGS kinematic eddy-viscosity

ξ	[m]	position vector
ρ	[kg m^{-3}]	air density
ϕ	[ϕ]	generic variable, latitude
ϕ_m	[-]	normalized wind shear, defined in equation (1.4)
$\overline{\phi}$	[ϕ]	time averaged generic variable $\phi(\mathbf{x},t)$, spatial filtered generic variable $\phi(\mathbf{x},t)$
$\sigma_{\tilde{\nu}}$	[-]	constant diffusive term (SA model), equation (2.8)
$\sigma_k, \sigma_\varepsilon$	[-]	turbulent Prandtl numbers for k and ε (k-ε model)
σ_k, σ_ω	[-]	turbulent Prandtl numbers for k and ω (k-ω model)
τ_w	[Pa]	wall shear stresses
τ_{ij}	[Pa]	SGS shear stresses, equation (2.22)
ω	[s^{-1}]	specific dissipation rate
χ	[-]	ratio modified eddy to laminar viscosity (SA model)
Ω	[s^{-1}]	computational domain, hearth's rotational speed
Ω_{ij}	[s^{-1}]	rotation rate tensor

Special notations

‘	(primes)	fluctuating component in a Reynolds decomposition
¯	(overbar)	time averaged (or space filtered) component
$\langle\ \rangle$	space averaging over horizontal plane	

Acronyms

ABL	Atmospheric Boundary Layer
AEP	Annual Energy Production
a.g.l.	above ground level
CFD	Computational Fluid Dynamics
CP	Center Point (Askervein hill topography)
CWE	Computational Wind Engineering
DES	Detached Eddy Simulation
DNS	Direct Numerical Simulation
HT	Hill Top (Askervein hill topography)
KE	k-ε model

LES	Large Eddy Simulation
NS	Navier Stokes equations
PBL	Planetary Boundary Layer
PDE	Partial Differential Equation(s)
RANS	Reynolds Averaged Navier Stokes
RC	Roughness Constant (Fluent's parameter for rough walls)
RH	Roughness Height (Fluent's parameter for rough walls)
RKE	Realizable k-ε model
RNG	Re-Normalization Group
RS	Reference Site (Askervein hill topography)
RSM	Reynolds Stress Model
SA	Spalart Allmaras
SFS	Sub Filter Scale
SGS	Sub Grid Scale
SKE	Standard k-ε model
SL	Smagorinsky-Lilly
SST	Shear Stress Transport
TDR	Turbulence Dissipation Rate
TKE	Turbulent Kinetic Energy
UDF	User Defined Function
URANS	Unsteady Reynolds Averaged Navier Stokes
WALE	Wall-Adapting Local Eddy-viscosity (SGS model)
WMLES	Wall Modeled LES

ABSTRACT

Nowadays there is a wide public interest for the exploitation of renewable energies sources and energy saving policies, the European Union is clearly aiming at increasing the production of energy from renewable sources and, at the same time, promoting among the European citizens an attention to avoid the waste of energy.

The development of renewable energies, particularly energy from wind, water, solar power and biomass, is a central task of the European Union's energy policy. There are several reasons for this orientation:

- Renewable energy has an important role to play in reducing Carbon Dioxide (CO_2) emissions, a major European Community objective.
- Increasing the share of renewable energy in the energy balance enhances sustainability.

It also helps to improve the security of energy supply by reducing the European Community's dependence on imported energy sources, mainly oil and natural gas.

Renewable energy sources are expected to be economically competitive with conventional energy sources in the medium to long term.

Several renewable energy technologies, especially wind energy, have achieved a level of maturity which allows them to compete to the standard energy sources even without the help of economic incentives as green certificates.

The numerical simulations of the Atmospheric Boundary Layer (ABL) afforded in the present PhD thesis can be seen as part of a more general framework of the Computational Wind Engineering (CWE). The increase of computational capacities for commonly used PCs and workstations and the relatively high and stable price of wind tunnel facilities guide nowadays the wind engineering to a wider usage of computational resources rather than experimental facilities.

Although the increased importance of the CWE, the wind-tunnel and on-site activities keep on being complementary and not alternative to computations as can be stated for most of the engineering branches.

The numerical simulations of the ABL are applied to the evaluation of the wind loads on structures, pollutants dispersion, the natural ventilation of buildings, the assessment of the pedestrian comfort in a urban environment, the sails aerodynamics of sails and many other topics.

For instance, CFD computations on given terrains coupled with the meteorological data are the starting point for a business plan of a wind farm.

Some numerical tools able to predict the Annual Energy Production (AEP) of a wind farm basing their analysis upon empirical relations are spread in the wind engineering community. The empirical relations commonly used for the computation of the speed-up due to the topography are prone to fail or loose accuracy when dealing with complex terrains.

A terrain can be considered complex when its steepness exceeds a certain threshold and above this level the empirical relations don't guarantee any success. In fact, in the flow around steep terrains, hills separation bubbles are very likely to occur and the level of turbulence is supposed to be quite high, furthermore also unsteady phenomena like shedding of vortices can occur. This kind of flows lead the commonly used empirical models to fail and the numerical solution of the RANS equations remains therefore only analysis able to reproduce the correct behaviour of the flow.

The present thesis focuses on the application of two commercial finite-volume CFD codes for the numerical simulations of the ABL flow. The first one is the more general finite volume solver Fluent and the second one, WindSim, is devoted to wind energy assessment using the general RANS finite-volume solver PHOENICS.

After a description of some topics regarding part of the physics of the ABL discussed on the Chapter 1, the following Chapter 2 treats the modelling of the ABL with finite volume solvers by integration of the Navier-Stokes equations modified for turbulence modelling.

Numerical simulations of the ABL are presented in the following sections: in Chapter 3 2D simulations while 3D simulations over an isolated hill (Askervein hill) are described in the Chapter 4; the test case of Askervein has been chosen since the wide range of anemometric data, gathered during two experimental campaigns and published in the two reports by Taylor and Teunissen (1985, 1986), [36] and [37].

A particular attention has been paid on the application of different turbulence models. Numerical results have been compared to data from Askervein Hill experimental campaign. The RANS equations have been solved with the k-ε (standard, RNG and realizable), k-ω and RSM when the code Fluent has been used, while only the standard k-ε model has been used with the code WindSim when solving the Askervein Hill case.

More advanced techniques as DES and LES have been also considered applied on flat terrains flow simulations, using the commercial code Fluent. This part of the research project has been carried out in collaboration with von Karman Institute for fluid dynamics during the 2005-06 Diploma Course, therefore the Chapter 5 is a modification of the final report for the von Karman Institute.

The last chapter of the PhD thesis is devoted to the description of a canopy model implemented in WindSim in order to emulate the flow over a forested area. A new canopy model has been proposed, based on the flow through porous media and the simulations reported in the chapter are the results of the three months training (april-june 2005) in the Vector A.S., Norway, and of the following and still active collaboration between the author and the developers of the code WindSim.

Chapter 1 THE ATMOSPHERIC BOUNDARY LAYER

1.1 THE ATMOSPHERIC BOUNDARY LAYER (ABL)

The Atmospheric Boundary Layer (ABL), or Planetary Boundary Layer (PBL), can be described like the "lowest 1-2 km of the atmosphere, the region most directly influenced by the exchange of momentum, heat, and water vapour at the earth's surface", *Kaimal and Finnigan* (1994) [17].

Stull (1988) [33] instead defines the boundary layer as "that part of the atmosphere that is directly influenced by the presence of the earth's surface, and responds to surface forcings with a timescale of about an hour or less". Moreover *Stull* (1988) [33] mentions several forcings perturbing the boundary layer, i.e. frictional drag, evaporation, heat and pollutants transfer, modifications of the flow due to topography. According to *Stull* (1988) [33] the ABL depth ranges from one hundred metres to few kilometres, depending on the forcings.

As regards the flows and phenomena inside an ABL a typical time scale is one hour (as already stated) while typical space scales are few kilometres; these scales are important to be also accounted for when numerical simulations have to be performed.

1.2 VELOCITY VERTICAL PROFILE IN ABL

A neutral ABL, where heat transfer is negligible, can be subdivided into several sub-layers, as sketched in Figure 1.1: a canopy layer attached to the ground surface, where the obstacles constituting the roughness elements are displaced; above the canopy layer there is the surface layer, where the effects of Coriolis force are still negligible. It is normally considered extending up to one tenth of the total height of the ABL; the outer layer of the ABL, or Ekman layer, which is instead affected by the rotation of the Earth by means of the Coriolis force. A rotation of the wind direction is therefore observed, gradually passing

from a crossing-isobars wind in the boundary layer to a parallel isobars wind (Geostrophic wind) in the free atmosphere where frictional forces are negligible.

The crossing isobars flow and the Geostrophic wind are due to the balance of friction, pressure gradient and Coriolis forces, in the surface layer the only important forces are friction and pressure gradient therefore it's not observed a significant variation of horizontal wind direction within it.

Geostrophic wind and wind in the Ekman layer are sketched in Figure 1.2.

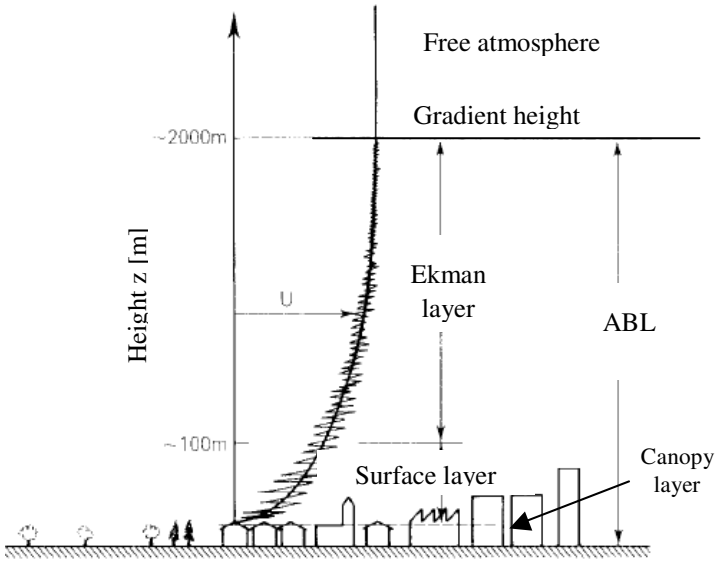

Figure 1.1 – Subdivision of the ABL (or PBL) into further sub-layers.

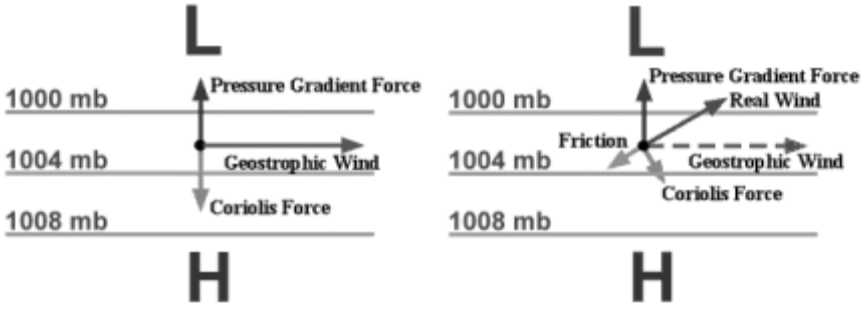

Figure 1.2 – Geostrophic wind and wind in the Ekman layer.

Theoretical considerations (Tennekes, 1982 [38]) lead to assume the boundary layer to have a depth proportional to u_τ/f, where u_τ is the friction velocity defined in (1.1) and f is the Coriolis parameter $2\pi\Omega\sin\phi$, Ω being the hearth's rotational speed and ϕ the latitude. The ABL height, in the case of neutral stratification, can be expressed by the (1.2).

$$u_\tau = \sqrt{\frac{\tau_w}{\rho}} \qquad \textbf{(1.1)}$$

$$z_h = C\left(\frac{u_\tau}{f}\right) \qquad \textbf{(1.2)}$$

A value of C = 0.25 yields boundary layer heights close to observed daytime heights.

If Coriolis, friction and pressure gradients are responsible for the wind flow in the outer layer and free atmosphere, in the surface layer the Coriolis force looses its importance while the roughness of the ground becomes a more significant parameter, affecting both the velocity profile and the angle of incidence of wind at the ground level and the isobars.

The roughness of the terrain influences the depth of the ABL as it's sketched in Figure 1.3, the rougher the terrain and the higher the ABL.

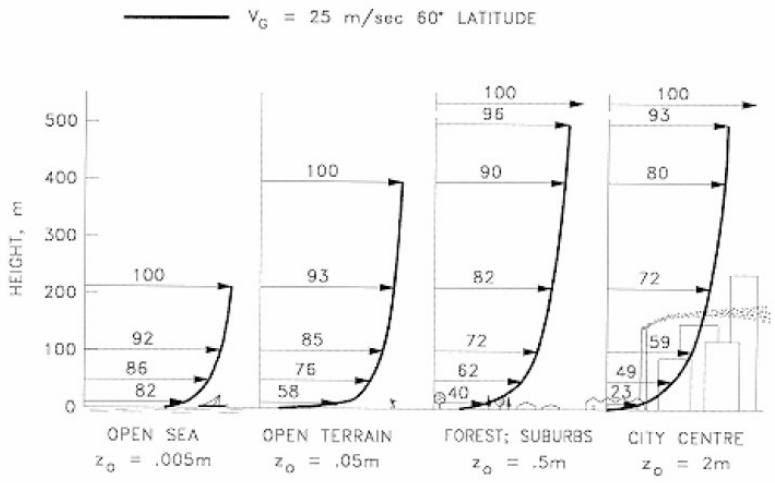

Figure 1.3 – different velocity profiles for four kinds of terrain typologies.

In Figure 1.3 the roughness of the terrain is described by the parameter z_0 which is called aerodynamic roughness length, or just roughness length, whose meaning will be introduced in the successive paragraph on similarity theory.

1.3 SIMILARITY THEORY

1.3.1 Introduction

Similarity theory provides a way to organize and group the variables of interest in dimensionless groups. This procedure is helpful to a better understanding of fluid-dynamics phenomena and provides guidelines for correct scaling in the experimental facilities.

A proper choice of the dimensionless groups should allow to establish "universal" relationships between the groups, valid in each condition, that can be represented in graphs, numerical tables or regression curves.

Several kind of similarities approaches have been proposed in literature for the ABL. In this paragraph only few relations are reported together with a similarity theory known also as Monin-Obukhov theory or surface-layer similarity so called since it is valid in the surface layer. For further information on similarity theories on the ABL it is suggested to refer to Stull (1988) [33].

1.3.2 Vertical profiles of velocity

A similarity study can be carried out to describe vertical profiles of turbulence statistics in the ABL when fully developed conditions (and therefore horizontal homogeneity) are reached. In the surface layer the mean horizontal velocity is commonly described by a log profile in neutral conditions (1.3). A neutral condition stands when thermal effects are negligible.

$$\frac{U(z)}{u_\tau} = \frac{1}{\kappa}\ln\left(\frac{z}{z_0}\right) \qquad \textbf{(1.3)}$$

In the equation (1.3) the mean horizontal velocity U is normalised it by the friction velocity u_τ, defined by (1.1), while the height z is compared to the

roughness length z_0 (the height where the mean velocity would go to zero according always to (1.3)) and κ is the von Karman constant (~0.4).

The typologies of terrain can be classified by their roughness length z_0, according to the classification proposed in the European Wind Atlas [39].

Table 1.1 – Classification of terrains by their roughness length, partially adapted from the European Wind Atlas (1989) [39]

class	terrains	z_0 [m]
I	Muddy terrains, wetlands, icepack	$10^{-5} \div 3\ 10^{-5}$
	Water areas *	$3\ 10^{-5} \div 0{,}0002$
II	Sand	$0{,}0002 \div 0{,}001$
III	Airport runway areas, mown grass	$0{,}001 \div 0{,}01$
IV	Farmland/Airports with very few trees, buildings, *etc.*	$0{,}01 \div 0{,}04$
V	Many trees and/or bushes	$0{,}04 \div 0{,}1$
VI	Forests, suburbs	$0{,}1 \div 1$
VII	Cities	$1 \div 4$

* Air and sea form a dynamically coupled system, the determination of the roughness length of open sea and water surfaces is usually obtained by models taking into account shapes and dimensions of the waves.

The first derivative of the mean horizontal velocity is referred as the wind shear, which can be combined with κ, z and u_τ to build a dimensionless group ϕ_m (1.4), which in neutral stability conditions equals one. In these conditions it leads to the log-law (1.3) while in non-neutral conditions it is generally expressed as a function of the dimensionless height z/L, where L is the Monin-Obukhov length.

$$\phi_m = \frac{\kappa z}{u_\tau}\frac{\partial U}{\partial z} \qquad \textbf{(1.4)}$$

1.3.3 Vertical profiles of second moments of velocities (Reynolds stresses)

Different vertical profiles for higher moments of the velocities have been also proposed, which pretend to be universal. According to Stull (1988) [33], the turbulent momentum flux for a neutral boundary layer can be considered decreasing linearly with the height z.

$$\frac{\overline{u'w'}}{\left(\overline{u'w'}\right)_S} = 1 - \frac{z}{z_h} \qquad \textbf{(1.5)}$$

For the variances of the velocities, Stull (1988) [33]:

$$\frac{\overline{u'^2}}{u_\tau^2} = 6\left(1 - \frac{z}{z_h}\right)^2 + \frac{z}{z_h}\frac{\overline{u'^2}_{top}}{u_\tau^2} \quad \textbf{for stream direction} \qquad \textbf{(1.6)}$$

$$\frac{\overline{v'^2}}{u_\tau^2} = 3\left(1 - \frac{z}{z_h}\right)^2 + \frac{z}{z_h}\frac{\overline{v'^2}_{top}}{u_\tau^2} \quad \textbf{for span direction} \qquad \textbf{(1.7)}$$

$$\frac{\overline{w'^2}}{u_\tau^2} = \left(1 - \frac{z}{z_h}\right)^{1/2} \quad \textbf{for vertical direction} \qquad \textbf{(1.8)}$$

As can be noticed in these expressions for the momentum flux and variances of velocity components (1.6)-(1.8) the altitude z is normalized against the depth of the boundary layer z_i rather than with the roughness length z_0.

In the expressions for the variances of the horizontal velocities (1.6) and (1.7) the values at the top of the boundary (assuming known a well-defined top height z_i), normalized by the surface stress, do appear. Although this ratio is expected to vary, during the KONTUR experiment (Grant, 1986) [14] it was found to equal 2.0 for both equations.

Taking into account the equations (1.6) to (1.8) and the definition of TKE (1.9) it follows also a vertical profile for the normalised TKE (1.10).

$$k = \frac{1}{2}\left(\overline{u'^2} + \overline{v'^2} + \overline{w'^2}\right) \tag{1.9}$$

$$\frac{k}{u_\tau^2} = \frac{1}{2}\left(\frac{\overline{u'^2}}{u_\tau^2} + \frac{\overline{v'^2}}{u_\tau^2} + \frac{\overline{w'^2}}{u_\tau^2}\right) =$$

$$= \frac{1}{2}\left(6\left(1-\frac{z}{z_h}\right)^2 + \frac{z}{z_h}\frac{\overline{u'^2}_{top}}{u_\tau^2} + 3\left(1-\frac{z}{z_h}\right)^2 + \frac{z}{z_h}\frac{\overline{v'^2}_{top}}{u_\tau^2} + \left(1-\frac{z}{z_h}\right)^{1/2}\right)$$

$$\frac{k}{u_\tau^2} = \frac{1}{2}\left(\frac{\overline{u'^2}}{u_\tau^2} + \frac{\overline{v'^2}}{u_\tau^2} + \frac{\overline{w'^2}}{u_\tau^2}\right) = \frac{1}{2}\left(9\left(1-\frac{z}{z_h}\right)^2 + 4\frac{z}{z_h} + \left(1-\frac{z}{z_h}\right)^{1/2}\right) \tag{1.10}$$

Chapter 2 CFD MODELLING OF THE ABL

2.1 THE NAVIER-STOKES EQUATIONS

The equations ruling the fluid mechanics are the mathematical expressions of three physical principles:

- the conservation of mass;
- the conservation of momentum;
- the conservation of energy.

Two of the mentioned principles (conservation of mass and energy) lead to two scalar expressions while the conservation of momentum turns into a vector one. The primitive equations of fluid mechanics that are always valid can be furthermore simplified; if the fluid is Newtonian and the flow incompressible only the continuity (mass conservation) and momentum equations can be considered, also called Navier-Stokes equations from the scientists that firstly derived them. The Navier-Stokes equations can be written in different forms and notations; they can be expressed, using the summation notation, by:

conservation of mass ("continuity equation"),

$$\frac{\partial}{\partial x_i}\left(u_i\right) = 0 \qquad \textbf{(2.1)}$$

conservation of momentum ("momentum equation"),

$$\rho\left(\frac{\partial}{\partial t}u_i + u_k\frac{\partial u_i}{\partial x_k}\right) = -\frac{\partial p}{\partial x_i} + \rho f_i + \frac{\partial}{\partial x_k}\left(\mu\frac{\partial u_i}{\partial x_k}\right) \qquad \textbf{(2.2)}$$

The equations of motion can be written in four different forms: in conservative (Eulerian reference frame) or non-conservative form (Lagrangian reference frame), in integral or differential form. When a particular flow has to be studied the equations of motion have to be integrated with given boundary conditions. In most of the cases the equations of motion can't be solved analytically and numerical solutions remain the only possible way.

From the purely theoretical point of view, the four forms are equivalent but they are not from the numerical point of view since some numerical procedures are referred to particular forms of the governing equations. For instance, in the finite-volume technique the Navier-Stokes equations are considered in their conservative integral form and applied to control volumes usually called cells that cover the whole computational domain.

The present thesis deals with the numerical simulations of the neutral ABL in micro-scale domains, which means dimensions of few kilometres; in such kind of flows both compressibility and thermal effects are negligible.

What instead is not negligible and plays an important role in an ABL is the turbulence. Turbulent flows can be solved directly in simulations named DNS which are affordable nowadays only to study very low Reynolds number cases and only by means of high performance computers. In a typical ABL the Reynolds number ranges between 10^5 and 10^{10} making these kind of flows affordable by time-averaged Navier-Stokes equations (RANS) and, in smaller domains, also with Wall Modelled Large Eddy Simulation (WMLES) and hybrid methodologies RANS/LES as the Detached Eddy Simulation (DES). All these methodologies will be described in the following sections dedicated to turbulence modelling.

2.2 TURBULENCE MODELLING

A classical approach in the study of turbulence is carried out by means of the Reynolds decomposition: the variables fluctuating in a turbulent flow can be decomposed into a mean and a fluctuating term.

The time-averaged (or Reynolds averaged) Navier-Stokes equations, shortly RANS, are obtained applying the Reynolds decomposition to the unknowns appearing in the Navier-Stokes equations and time averaging. The RANS contain further unknowns called Reynolds stresses which are due to all scales turbulence and need to be modelled in order to close the set of equations. The biggest advantage of using the RANS in simulating turbulence flows is that they allow to treat the turbulence as a steady phenomena, i.e. if a flow is unsteady

only because of turbulence the RANS simulation will be a steady simulation, with great saving of computational means.

The RANS based turbulence models are usually classified by the number of additional differential equations needed to close the original set of PDE Some of turbulence models used to close the RANS are:

- algebraic or zero equation model: mixing length;
- one equation model: Spalart Allmaras
- two equations model: k-ε (e.g. standard, RNG, realizable)
- two equations model: k-ω (e.g. standard, SST)
- five (2D) and seven equations (3D): RSM (Reynolds Stress Model)

A second approach to the turbulence modelling which is gaining more and more applications is the Large Eddy Simulation (LES), which is based on the space filtered Navier-Stokes equations.

The finite volume technique is equivalent to apply a space filter to the Navier-Stokes equations; in this fashion only the big eddies whose dimensions are larger than the filter width, which is connected to the cell's dimensions, are computed directly. The non resolvable eddies or sub-filter eddies are modelled with specific turbulence models named Sub Grid Scale (SGS) or Sub Filter Scale (SFS) turbulence models.

Due to the fact that the biggest eddies have to be calculated directly, a LES simulation can be only 3D and unsteady. Even if in some particular cases, for instance for some external aerodynamics, good solutions can be obtained in 2D but always with unsteady simulations.

It's well known that RANS turbulence models are characterised by few constants that have to be tuned to best simulate the given problem. In some way the RANS turbulence models are all problem dependent and this is one big defect of the RANS models. Big eddies are strongly anisotropic and depend upon boundary conditions and mean flow; considering instead smaller and smaller eddies they loose information about mean flow and boundary

conditions, small vortices are also more homogeneously spread and more isotropic. There is hope that small scale vortices are universal and that SGS models can work for every kind of turbulence if the filter width is applied at the proper size.

The LES still requires the usage of supercomputing for high Reynolds numbers and the main reason of that is the fine grid needed to discretize the near wall region in wall bounded flows. When the walls are smooth and pure LES is desired than the constraints for the resolution of the grid for the wall adjacent cells is about 100 wall units streamwise and 20 spanwise, while only one wall unit normally to the wall. Among the methodologies born to treat high Reynolds numbers the hybrid LES-RANS named Detached Eddy Simulation (DES) have to be mentioned. With these techniques the near wall region is modelled with a RANS approach and the zone distant from the wall the flow is treated with a LES approach. The DES is constructed by modifying the usual RANS model (SA, k-ε, k-ω) which acts in the standard way close to the wall and in a modified one at a certain distance from the wall, as a SGS model. The DES was born to deal with external aerodynamics issues, for instance to compute the flow around an airfoil in stall conditions and the model is conceived to treat the attached boundary layer with the URANS methodology and the detached vortices with LES.

2.3 THE RANS EQUATIONS

The turbulent flows can be treat as steady if the flow statistics remain constant when calculated over a period T large enough; in this case the flow is called statistically steady.

The Navier-Stokes equation can be time averaged over a period T large enough to mean the turbulent fluctuations in order to obtain the Reynolds Averaged Navier-Stokes (RANS) equations.

A generic variable, fluctuating because of the turbulence, can be decomposed in a mean part and a fluctuating part according to the Reynolds decomposition.

$\phi(t)=\bar{\phi}+\phi'(t)$ Reynolds decomposition

In the present thesis both overbar and capital letter notation have been used to identify a time averaged variable.

Where the mean value is obtained by:

$$\bar{\phi}=\frac{1}{T}\int_0^T \phi(t)dt \qquad \textbf{(2.3)}$$

And the integration time must be such that the average of the fluctuating component is zero.

$$\overline{\phi'}=\frac{1}{T}\int_0^T \phi'(t)dt=0 \qquad \textbf{(2.4)}$$

The integration time T over which a general variable ϕ is observed in order to smooth the fluctuations due to turbulence is comparable to several turn-over periods of the vortices.

After applying the Reynolds decomposition and time averaging the NS equations the RANS are obtained, for instance written for Cartesian coordinates and uncompressible flow in (2.5), continuity, and (2.6) momentum equation.

Further unknowns are hence introduced, $-\rho\overline{u'_i u'_j}$, named the Reynolds stresses which need to be modelled to close the set of equations. Even if the Reynolds stresses are originated by time averaging the convective term of the Navier-Stokes they are usually grouped in the diffusive term of the RANS momentum, like in first term of the right hand side of the (2.6). In fact they are responsible for the turbulent diffusion of momentum which in a fully turbulent flows is several order of magnitude higher than the molecular diffusion due to viscosity.

$$\frac{\partial U_j}{\partial x_j}=0 \qquad \textbf{(2.5)}$$

$$U_j \frac{\partial U_i}{\partial x_j} = \frac{1}{\rho}\frac{\partial}{\partial x_j}\left(\tau_{ij} - \rho\overline{u_i' u_j'}\right) - \frac{1}{\rho}\frac{\partial P}{\partial x_i} + F_i \qquad \textbf{(2.6)}$$

A way to model the Reynolds stresses, which account for six variables in 3D and three in 2D, is by assuming true the Boussinesq hypothesis to relate the Reynolds stresses to the mean velocity gradients introducing in this way the eddy-viscosity concept.

$$-\rho\overline{u_i' u_j'} = \mu_t\left(\frac{\partial U_i}{\partial x_j} + \frac{\partial U_j}{\partial x_i}\right) - \frac{2}{3}\left(\rho k + \mu_t \frac{\partial U_i}{\partial x_i}\right)\delta_{ij} \qquad \textbf{(2.7)}$$

The set of PDE could be closed by imposing a constant eddy-viscosity, resulting in a very poor turbulence modelling. More often a transport equation is used for the (modified) eddy viscosity like in the SA model, or the eddy viscosity is computed with an algebraic equation taking into account a length scale and a velocity scale of the turbulence, computed by other two variables linked to turbulence and transported by two further PDE.

The turbulence models that close the set of equations are usually classified by the number of additional transport equations: a one equation model is the SA, while largely employed two equations models are the k-ε, the k-ω and their modifications.

A way to close the RANS without the Boussinesq hypothesis is to apply a transport equation for each Reynolds stress. This approach is followed in the RSM model, which in 3D is a 7 equations model, 6 equations for Reynolds stresses and one for dissipation.

Even if the RSM model is capable to simulate the anisotropy of the turbulence it requires a large computational cost. This one reason why nowadays is more common to perform unsteady simulations URANS, DES or LES rather than steady RSM.

In the following sections some turbulence treatments will be described, in particular eddy viscosity models in paragraph 2.4 and eddy solving methodologies LES and DES in paragraph 0.

2.4 EDDY VISCOSITY MODELS

2.4.1 A one equation turbulence model: the Spalart-Allmaras (SA) model

The basic concepts of the Spalart-Allmaras model are now recalled in order to make more comprehensible its modification leading to the SA based DES model.

In the SA model a further transport equation (2.8) for a modified turbulent viscosity $\tilde{\nu}$ is used to close the system of RANS equations.

$$\frac{\partial}{\partial t}(\rho\tilde{\nu})+\frac{\partial}{\partial x_i}(\rho\tilde{\nu}u_i)=G_\nu+\frac{1}{\sigma_{\tilde{\nu}}}\left[\frac{\partial}{\partial x_j}\left\{(\mu+\rho\tilde{\nu})\frac{\partial\tilde{\nu}}{\partial x_j}\right\}+C_{b2}\rho\left(\frac{\partial\tilde{\nu}}{\partial x_j}\right)^2\right]-Y_\nu \qquad \textbf{(2.8)}$$

where G_ν is the production of turbulent viscosity and Y_ν is the destruction of turbulent viscosity that occurs in the near-wall region due to wall blocking and viscous damping. $\sigma_{\tilde{\nu}}$ and C_{b2} are constants and ν is the molecular kinematic viscosity.

The turbulent viscosity is computed by:

$$\mu_t=\rho\tilde{\nu}f_{v1} \qquad \textbf{(2.9)}$$

$$f_{v1}=\frac{\chi^3}{\chi^3+C_{v1}^3}$$

$$\chi\equiv\frac{\tilde{\nu}}{\nu}$$

The production term G_ν is modelled by

$$G_\nu=C_{b1}\rho\tilde{S}\tilde{\nu}$$

and,

$$\tilde{S}\equiv S+\frac{\tilde{\nu}}{\kappa^2 d^2}f_{v2}$$

Where C_{b1} is a constant of the model, ρ the density of the fluid and $\tilde{S}$ given by the previous equation, defined as the sum of S, depending on deformation

and rotation tensor, and a term accounting for the vicinity of the wall through the distance to the nearest wall d; κ is the von Karman constant (~0,4187 in Fluent 6.2) and the function f_{v2} is evaluated by:

$$f_{v2} = 1 - \frac{\chi}{1 + \chi f_{v1}}.$$

In the original form of the SA model the scalar S is computed by the magnitude of the rotation-rate tensor Ω_{ij}.

$$S = \sqrt{2\left(\Omega_{ij}\,\Omega_{ij}\right)}$$

with

$$\Omega_{ij} = \frac{1}{2}\left(\frac{\partial U_i}{\partial x_j} - \frac{\partial U_j}{\partial x_i}\right)$$

And this is also the default value for S in the Fluent Spalart-Allmaras option. The second option available in Fluent for the choice of S is:

$$S \equiv \left|\Omega_{ij}\right| + C_{prod}\,\min\left(0, \left|S_{ij}\right| - \left|\Omega_{ij}\right|\right) \qquad \textbf{(2.10)}$$

Being S_{ij} the element of strain-rate tensor.

$$S_{ij} = \frac{1}{2}\left(\frac{\partial U_i}{\partial x_j} + \frac{\partial U_j}{\partial x_i}\right)$$

With C_{prod} = 2.0 as default value. The destruction term Y_ν is modelled by:

$$Y_v = C_w \rho f_w \left(\frac{\tilde{\nu}}{d}\right)^2$$

$$f_w = g\left[\frac{1+C_{w3}^6}{g^6+C_{w3}^6}\right]^{1/6}$$

$$g = r + C_{w2}\left(r^6 - r\right)$$

$$r \equiv \frac{\tilde{\nu}}{\tilde{S}\kappa^2 d^2}$$

The default values for the SA model constants are given in table below:

Table 2.1 - default values in Fluent 6.2 for the Spalart-Allmaras model constants

$C_{b1} = 0.1355$	$C_{b2} = 0.622$
$\sigma_{\tilde{\nu}} = \frac{2}{3}$	$C_{v1} = 7.1$
$C_{w1} = \frac{C_{b1}}{\kappa^2} + \frac{(1+C_{b2})}{\sigma_{\tilde{\nu}}}$	$C_{w2} = 0.3$
$C_{w3} = 2.0$	$\kappa = 0.4187$

The standard Spalart-Allmaras model uses the distance to the closest wall as the definition for the length scale *d*, which plays a major role in determining the level of production and destruction of turbulent viscosity.

2.4.2 Two equations turbulence models

In the two equations turbulence models the eddy viscosity is generally defined by means of a velocity scale V_S and a length scale ℓ_S using the (2.11). A velocity scale which is generally accepted to describe turbulence is the square root of the turbulent kinetic energy k, while for the length scale different choices are available, velocity and length scale for the k-ε and k-ω model are reported in Table 2.2.

$$\mu_t = \rho C_\mu V_S \ell_S \qquad \textbf{(2.11)}$$

Table 2.2 – Velocity scale and length scale for k-ε and k-ω models

	V_S	ℓ_S
k-ε	$k^{1/2}$	$k^{3/2}/\varepsilon$
k-ω	$k^{1/2}$	$k^{1/2}/\omega$

- **Model k-ε: standard and RNG**

The standard *k-ε* model is a two equations model based on the transport equations for the turbulence kinetic energy (k) and its dissipation rate (ε):

$$\frac{\partial}{\partial t}(\rho k)+\frac{\partial}{\partial x_i}(\rho k u_i)=\frac{\partial}{\partial x_j}\left[\left(\mu+\frac{\mu_t}{\sigma_k}\right)\frac{\partial k}{\partial x_j}\right]+G_k+G_b-\rho\varepsilon-Y_M+S_k$$

$$\frac{\partial}{\partial t}(\rho\varepsilon)+\frac{\partial}{\partial x_i}(\rho\varepsilon u_i)=$$
$$=\frac{\partial}{\partial x_j}\left[\left(\mu+\frac{\mu_t}{\sigma_\varepsilon}\right)\frac{\partial \varepsilon}{\partial x_j}\right]+C_{1\varepsilon}\frac{\varepsilon}{k}(G_k+C_{3\varepsilon}G_b)-C_{2\varepsilon}\rho\frac{\varepsilon^2}{k}+S_\varepsilon$$

In the additional transport equations two production terms do appear i.e. G_k and G_b, respectively the generation of TKE due to velocity gradients and buoyancies. The term Y_M takes into account compressibility effects while the source terms are labelled with S; for a neutral ABL the generation due to buoyancies is negligible, as well as the compressibility effects and there are no sources, therefore the two transport equations for k and ε can be simplified:

$$\frac{\partial}{\partial t}(\rho k)+\frac{\partial}{\partial x_i}(\rho k u_i)=\frac{\partial}{\partial x_j}\left[\left(\mu+\frac{\mu_t}{\sigma_k}\right)\frac{\partial k}{\partial x_j}\right]+G_k-\rho\varepsilon$$

$$\frac{\partial}{\partial t}(\rho\varepsilon)+\frac{\partial}{\partial x_i}(\rho\varepsilon u_i)=\frac{\partial}{\partial x_j}\left[\left(\mu+\frac{\mu_t}{\sigma_\varepsilon}\right)\frac{\partial \varepsilon}{\partial x_j}\right]+C_{1\varepsilon}\frac{\varepsilon}{k}G_k-C_{2\varepsilon}\rho\frac{\varepsilon^2}{k}$$

In the standard k-ε model the eddy viscosity is modelled by the equation (2.11) with scales as in Table 2.2. The TKE generation term is modelled by $\mu_t S^2$ where S is the magnitude of rate-of-strain tensor.

Constants appear in the standard k-ε formulation: their values are far to being universal and some values are generally accepted since they produce right level of turbulence in common industrial flows.

In the case of neutral ABL flows other values of constants have been proposed, Crasto *et al.* (2004) [8] and Mandas *et al.* (2004) [23], in order to produce a proper level of turbulence in proximity of the ground. The default values adopted in Fluent 6.2 for the model constants and the modified set of constants as in Crasto *et al.* (2004) [8] and Mandas *et al.* (2004) [23] are shown in Table 2.3.

Table 2.3 – standard k-ε *model constants*

	C_μ	$C_{1\varepsilon}$	$C_{2\varepsilon}$	σ_k	σ_ε
Default	0,09	1,44	1,92	1	1,3
Modified	0,03	1,44	2,223	1	1,3

In the commercial code Fluent 6.2 two k-ε models derived from the standard one are available: the RNG k-ε and the realizable k-ε. Further information about these two modifications of the standard k-ε are provided in the Fluent User's Guide [10].

The RNG modification of the k-ε model provides the possibility to compute the effective viscosity by the use of a further differential equation, in this fashion the algebraic equation (2.11) is not any more employed. If the option is

activated the model acts fairly well in low Reynolds conditions hence near-wall flows. An improvement is therefore expected also for ABL simulations.

The RNG k-ε does make also use of constants which have to be properly set to achieve best results for each flow condition. The default values of constants for the RNG k-ε model in Fluent 6.2 and the modification proposed are given in the table below.

Table 2.4 – RNG k-ε *model constants*

	C_μ	$C_{1\varepsilon}$	$C_{2\varepsilon}$
Default	0.0845	1.42	1.68
Modified	0.05	1.42	1.68

- **Model k-ω: standard and SST (Shear-Stress Transport)**

The standard k-ω model is characterized by the two transport equations:

$$\frac{\partial}{\partial t}(\rho k)+\frac{\partial}{\partial x_i}(\rho k u_i)=\frac{\partial}{\partial x_i}\left(\Gamma_k \frac{\partial k}{\partial x_i}\right)+G_k-Y_k+S_k \qquad \textbf{(2.12)}$$

$$\frac{\partial}{\partial t}(\rho \omega)+\frac{\partial}{\partial x_i}(\rho \omega u_i)=\frac{\partial}{\partial x_i}\left(\Gamma_\omega \frac{\partial \omega}{\partial x_i}\right)+G_\omega-Y_\omega+S_\omega \qquad \textbf{(2.13)}$$

Where G_k e G_ω are respectively the production of k and ω due to velocity gradients, Γ_k and Γ_ω diffusive coefficients, Y are dissipation terms and with S are labelled the sources.

The diffusive coefficients are modelled as in the standard k-ε by:

$$\Gamma_k=\mu+\frac{\mu_t}{\sigma_k} \qquad \textbf{(2.14)}$$

$$\Gamma_\omega=\mu+\frac{\mu_t}{\sigma_\omega} \qquad \textbf{(2.15)}$$

The molecular viscosity μ is incorporated in the diffusive terms while σ_k and σ_ω are turbulent Prandtl numbers for k and ω. The turbulent viscosity is computed in the k-ω turbulence model by the (2.16).

$$\mu_t = \alpha^* \frac{\rho k}{\omega} \qquad \textbf{(2.16)}$$

Obviously the parameter α^* has the same meaning of C_μ employed in the standard k-ε model but in the k-ω model α^* changes dynamically in order to make the model fit to low Reynolds regions. It's for this reason that the k-ω model is naturally more suitable than the SKE for wall bounding flows.

The k-ω model, as all the RANS models, is completed with a set of parameters whose optimal value changes quite a lot depending on the flow features: mean flow and level of turbulence.

In addition to the standard k-ω model described in the previous section the standard k- ω model, FLUENT also provides a variation called the shear-stress transport (SST) k- ω model, called in this way since the definition of the turbulent viscosity is modified to account for the transport of the principal turbulent shear stress. The transport equations for the SST k- ω model and its features are reported in Fluent User's Guide [10].

2.5 EDDIES SOLVING METHODOLOGIES: LES AND DES

2.5.1 Filtered Navier-Stokes equations

Increasing computational capabilities and the possibility to build clusters of computers allow nowadays to perform simulations of the ABL with eddies solving methodologies like the LES (or more correctly with Wall Modelled LES, WMLES) and hybrid methodologies RANS/LES as the DES.

In the LES model the governing equations are space filtered rather than time averaged as in RANS. A general variable $\phi(\xi,t)$ space filtered is:

$$\bar{\phi}(\mathbf{x},t)=\int_{\Omega}\phi(\xi,t)G(\xi,\mathbf{x})d\xi \qquad \textbf{(2.17)}$$

Where G is a filter function and the volume integral is extended on the whole computational domain Ω. If the filter function has a compact support the integral is reduced to the support of the filter function.

For finite volume solvers like Fluent or PHOENICS the grid itself acts as a Top-Hat filter, considering a domain subdivided in a mesh, in a inner cell of volume *V*:

$$G(\xi,\mathbf{x})=\begin{cases}1/V, & \xi\in V\\ 0, & \xi\notin V\end{cases} \qquad \textbf{(2.18)}$$

In this fashion the mesh itself acts as a spatial filter; other types of filters can be used, for instance the Gaussian filter or the sharp Fourier cut-off. It follows also that the filter width is directly connected to the cubic root of the cell volume.

Application of the (2.17) and (2.18) brings to a filtered function $\bar{\phi}$ given by:

$$\bar{\phi}(\mathbf{x},t)=\frac{1}{V}\int_{V}\phi(\xi,t)d\xi, \qquad \xi\in V \qquad \textbf{(2.19)}$$

Where now the overbar is used to indicate a space filtering procedure. The filtered Navier-Stokes equations for the case of incompressible isothermal flows are given by:

$$\frac{\partial\rho}{\partial t}+\frac{\partial}{\partial x_i}\left(\rho\overline{u_i}\right)=0 \qquad \textbf{(2.20)}$$

$$\frac{\partial}{\partial t}\left(\rho\overline{u_i}\right)+\frac{\partial}{\partial x_j}\left(\rho\overline{u_i u_j}\right)=\frac{\partial}{\partial x_j}\left(\mu\frac{\partial\overline{u_i}}{\partial x_j}\right)-\frac{\partial\overline{p}}{\partial x_i}-\frac{\partial\tau_{ij}}{\partial x_j} \qquad \textbf{(2.21)}$$

With the filtering of the Navier-Stokes equations a closure problem is also introduced since the τ_{ij}, named SFS shear stresses, depend on further unknowns $\overline{u_i u_j}$.

$$\tau_{ij} = \rho\overline{u_i u_j} - \rho\overline{u_i}\,\overline{u_j} \qquad \textbf{(2.22)}$$

In order to close the set of equations the SFS stress terms have to be modelled. The basic idea of the LES is that small scale vortices are universal, do not depend on mean flow and boundary conditions. Therefore if the filter width is set to a proper value, i.e. if the mesh is enough refined the SFS model should be universal and acts correctly regardless the type of flow.

2.5.2 Sub Filter Scale (SFS) modelling

As introduced in the previous paragraph, the filtered NS equations introduce a closure problem; the turbulence closure is assigned to the SFS model that is devoted to simulate the filtered turbulence i.e. the shear stress term in the momentum equation (2.22).

Pioneering work of Smagorinsky (1963) [29] on LES employed the concept of SGS eddy viscosity (2.24); while equations (2.23)-(2.27) describe the Smagorinsky-Lilly model how is implemented in Fluent 6.2.

Eddy viscosity models do not allow back-scatter of energy from small eddies to bigger eddies which is not negligible when dealing with small scale turbulence and for flows close to the wall. Attempts to cure the lack of back-scatter in boundary layer flows have been proposed by Mason &Thomson (1992) [24] by adding a stochastic forcing to the velocities in the wall adjacent cells. The technique of the stochastic forcing allows to obtain a velocity profile closer to the logarithmic profile.

$$\tau_{ij} - \frac{1}{3}\tau_{kk}\delta_{ij} = -2\mu_t\overline{S_{ij}} \qquad \textbf{(2.23)}$$

$$\mu_t = \rho L_S^2 S \qquad \textbf{(2.24)}$$

$$\overline{S_{ij}} = \frac{1}{2}\left(\frac{\partial\overline{u_i}}{\partial x_j} + \frac{\partial\overline{u_j}}{\partial x_i}\right) \qquad \textbf{(2.25)}$$

$$S = \sqrt{2\overline{S_{ij}}\,\overline{S_{ij}}} \tag{2.26}$$

$$L_S = \min\left(\kappa d, C_S V^{1/3}\right) \tag{2.27}$$

The Smagorinsky constant C_S employed in the Smagorinsky model more realistically varies in a range of values depending on the local turbulence. A way to improve the Smagorinsky model is to compute dynamically the Smagorinsky constant as a function of the flow features, a dynamic Smagorinsky model like the one proposed by Germano *et al.* (1991) [13] and subsequently modified by Lilly (1992) [22] which is implemented in the code Fluent 6.2 as described in Kim (2004) [19].

A different approach to the turbulent closure for the filtered Navier-Stokes equations and further improvements to SGS modelling have been made by Bardina *et al.* (1983) [2] with the first scale-similarity model. In the scale-similarity models the unfiltered velocity is expressed as a function of the filtered velocity $u_i \approx f(\overline{u_i})$; for instance the unfiltered velocity can be written as a truncated Taylor series of the filtered resolved velocity. The simplest scale-similarity model is the one proposed by Bardina *et al.* (1983) [2] where the authors proposed that the velocity could be approximated with the filtered velocity $u_i \approx \overline{u_i}$. In this way the SFS stress term of (2.22) becomes:

$$\tau_{ij} = \rho\overline{\overline{u_i}\,\overline{u_j}} - \rho\overline{\overline{u_i}}\,\overline{\overline{u_j}} \tag{2.28}$$

Mixed models of scale similarity and dynamic eddy-viscosity have been also proposed, for instance in Zang *et al.* (1993) [42]. Mixed models are able to compute both back-scatter and forward-scatter of energy respectively from small-scale vortices to bigger-scale and vice versa and viscous dissipation, hence a behaviour closer to the reality compared to pure eddy-viscosity models which don't allow back-scatter.

Although in the code employed Fluent 6.2 four types of eddy-viscosity SGS models are available, these models resulted to be not applicable in the case of

ABL since the LES option in Fluent can be performed only for smooth surfaces. In the Chapter 5 the results of simulations of the ABL over flat terrains are illustrated. Some of them obtained by applying the DES module of Fluent and other by using an UDF defining a Smagorinsky model; both the methodologies were coupled with wall-functions for rough surfaces. Therefore a WMLES approach rather than a proper LES.

2.5.3 Hybrid RANS/LES models. The SA based DES model

The Detached Eddy Simulation (DES) model belongs to the class of LES/RANS hybrid models usually obtained by modifications of turbulence models originally born to close the RANS equations; the modified models act in their original form close to the wall while at a certain distance from the wall the modification is activated and the model provides an SGS eddy-viscosity.

The main aim of hybrid RANS/LES modelling is to work in applications in which pure LES is not affordable since the high number of cells required, i.e. high Reynolds number flows. The DES models were originally born for external aerodynamics applications where the attached boundary layers were supposed to be solved completely by the URANS models while the LES zone was aimed at solving the detached vortices. Also in flows over complex terrains the DES models can find an area of application even this is not the case for which they have been originally conceived. When DES is applied to the ABL the URANS zone solves only part of the boundary layer while the grey zone URANS/LES resides inside the logarithmic region and a typical shift of velocity is generally observed in the interface region.

The DES model was originally proposed by Spalart *et al.* (1997) [31] by modification of the Spalart-Allmaras RANS model.

In FLUENT 6.2 the only DES model available by default is based on the one-equation Spalart-Allmaras model. Two-equations DES models have been also proposed, based on transport equations of k and ε and also of k and ω; two equations DES models have been only recently introduced in the newest version of Fluent, the 6.3, which has not been used for the present project.

The SA based DES model implemented in Fluent, as proposed by Shur *et al.* (1999) [28] replaces the distance to the nearest wall *d* both in the production and destruction terms of the SA model with a new length scale $\tilde{d}$, defined as:

$$\tilde{d} = \min\left(d, C_{DES}\,\Delta\right) \qquad \textbf{(2.29)}$$

When the equation (2.29) is substituted in the SA model, in a time marching procedure the effect obtained is to have a URANS zone close to the wall where ($d < C_{DES}\,\Delta$) while the rest of the domain is treated in a LES way using the modified SA as SFS model.

The filter size Δ by default in Fluent 6.2 is based on the largest cell dimension while the empirical constant C_{DES} has a default value of 0,65.

The constant C_{DES} affects both the position of the interface separating the RANS and the LES zone but also the value of SGS turbulent viscosity in the LES zone as it will be described in Chapter 5.

2.6 WALL FUNCTIONS FOR ROUGH SURFACES

According to the theory proposed by Cebeci and Bradshaw (1977) [6] a turbulent boundary layer bounding a rough surface can be described with three kinds of fluid dynamic regimes depending upon a Reynolds number K_S^+ based on the dimension of roughness elements K_S (equivalent sand diameter) and the friction velocity u_τ.

$$K_S^+ = \frac{\rho K_S u_\tau}{\mu} \qquad \textbf{(2.30)}$$

Cebeci and Bradshaw (1977) [6] proposed that the universal log-law for smooth walls (2.31) could be modified for rough surfaces (2.32) by subtracting a function ΔB.

$$u^+ = \frac{1}{\kappa}\ln\left(y^+\right) + B \qquad \textbf{(2.31)}$$

$$u^+ = \frac{u}{u_\tau};\ y^+ = \frac{\rho\, y\, u_\tau}{\mu}$$ **Wall coordinates**

Where u^+ and y^+ are the wall coordinates, κ is the von Karman constant and B an experimental constant which is found to be around 5,45.

$$u^+ = \frac{1}{\kappa}\ln\left(y^+\right) + B - \Delta B \qquad \textbf{(2.32)}$$

The three hydro dynamic flow regimes previously mentioned are:

- Hydro-dynamically smooth ($K_S^+ < 2.25$)
- Transitional ($2.25 < K_S^+ < 90$)
- Fully rough ($K_S^+ > 90$)

The new term ΔB can be expressed as function of the dimensionless roughness height K_S^+. In Fluent 6.2 the expressions of ΔB for the three different regimes are given by

- in hydro-dynamically smooth regime:

  $\Delta B = 0$

- in transitional regime:

  $$\Delta B = \frac{1}{\kappa}\ln\left(\frac{K_S^+ - 2.25}{87.75} + C_S K_S^+\right)\sin\left[0.4258\left(\ln K_S^+ - 0.811\right)\right]$$

- in fully-rough regime:

  $$\Delta B = \frac{1}{\kappa}\ln\left(1 + C_S K_S^+\right)$$

Two parameters are used in Fluent to describe the roughness of a wall: the constant C_S and the roughness height K_S. Fluent first computes the friction velocity u_τ which is used to evaluate the dimensionless roughness height K_S^+ that is used to calculate the ΔB and finally the velocity at the wall adjacent cell by means of the (1.32).

Experience and suggestions in the Fluent User's Guide [10] about the proper usage of the wall functions for rough surfaces ensure that the height of the wall adjacent cells has to be at least twice the roughness height K_S, hence if a more refined grid (normally to the wall) is desired the constant C_S has to be increased keeping constant the product $C_S K_S$.

By comparison of the equation (1.3) with the (2.32) in fully rough regime after some algebra a simple relation is found between the product $C_S K_S$ and the aerodynamic roughness length z_0.

$$C_S K_S \approx E z_0 \qquad \textbf{(2.33)}$$

Where E equals $\exp(\kappa B)$.

From a theoretical point of view the wall functions are correct only if the horizontal pressure gradients are negligible (in equilibrium conditions) but in the common usage of the code the wall functions are applied as boundary conditions in every kind of wall bounding flow without penalising too much the solution.

The mathematical procedure followed to derive the equation (2.33) is reported in Appendix B.

2.7 CONCLUSIONS

In the present Chapter some basis of ABL modelling are presented. Firstly an overview of the time averaged (or Reynolds Averaged) Navier-Stokes equations is made; the RANS introduce a closure problem because of the introduction of new unknowns, the Reynolds stresses. The closure of the equations is obtained with turbulence models, which are generally classified with the number of transport equations constituting a model.

Further approaches for solving of equations for turbulent flows like WMLES and DES have been also described.

The described methodologies have been tested in CFD simulations. Results of RANS simulations carried out with the code Fluent 6.2 on flat terrains aimed at a proper setting of roughness parameters and turbulence modelling are presented in Chapter 1. 3D RANS simulations on a isolated hill (Askervein Hill) performed with the codes Fluent 6.2 and WindSim 4.5 and 4.6 are presented in the Chapter 1.

In Chapter 5 a first investigation of the use of the DES and LES options of the commercial code Fluent 6.2 for the simulation of a neutral ABL is presented. The Chapter 5 reports with some modifications part of the Diploma Course project's thesis Crasto G. (2006) [9] carried out by the author in 2005-06 at the von Karman institute.

Chapter 3 2D RANS SIMULATIONS

3.1 SETTINGS OF ROUGHNESS PARAMETERS

A series of 2D RANS simulations have been performed with the code Fluent 6.2 in order to set the proper values for the roughness parameters K_S and C_S and the minimum height of the wall adjacent cell compatible with the wall functions for rough surfaces. The dimension of the wall adjacent cells normally to the wall should be at least twice the roughness parameters K_S representing the dimension of the roughness elements. Simulations have been performed for each class of roughness defined in Table 1.1.

In the values of roughness parameters and cell height h in Table 3.1 C_S has been always fixed to one since it is the maximum allowed without importing in the code files named "profile files" in the code's user manual [10], equation (2.33) leads to a value for K_S for a given value of roughness length z_0.

If a more vertically refined grid is desired the constant parameter C_S in Fluent 6.2 has to be higher than one and therefore assigned by profile files. For instance if C_S equals E than K_S equals z_0 and h at least twice z_0.

Table 3.1 – Classification in roughness classes, values of K_S, C_S *and height of the ground adjacent cell h for the given mean* z_0.

class	mean z_0 [m]	K_S [m]	C_S	h [m]	z_0 [m]
I	0,0001	0,000981	1	0.002	$10^{-5} \div 0{,}0002$
II	0,0005	0,004905	1	0.01	0,0002 ÷ 0,001
III	0,005	0,04905	1	0.1	0,001÷0,01
IV	0,03	0,2943	1	0.6	0,01 ÷ 0,04
V	0,07	0,6867	1	1.4	0,04 ÷ 0,1
VI	0,55	5,3955	1	10.8	0,1 ÷ 1
VII	2,5	24,525	1	50	1 ÷ 4

3.2 GEOMETRY AND GRIDS

The 2D tests performed to evaluate the effects of the different turbulence models have been performed on a simple domain 6 km long and 1 km high. A uniform spacing has been used for the horizontal direction, while vertically a fixed expansion ratio α has been employed which is the ratio of the heights of two adjacent cells; the height of the first cell h is in accordance with Table 3.1. The geometric characteristics of the used grids are summarised in Table 3.2.

Table 3.2 – geometric characteristics of the used grids.

height of the domain (y direction)	**Ly**	1000 m
length of the domain (x direction)	**Lx**	6000 m
length of the cell (stream-wise)	**Δx**	20 m
number of horizontal intervals	**Nx**	300

class	**h [m]**	**α**	**Ny**	**N**
I	0.002	1.100	114	34200
II	0.01	1.22	50	15000
III	0.1	1.126	60	18000
IV	0.6	1.086	60	18000
V	1.4	1.117	40	12000
VI	10.8	1.023	50	15000
VII	50	1.000	20	6000

3.3 BOUNDARY CONDITIONS

Physically an ABL has only one border, the terrain, but computational domains have to be bounded in all directions and other unphysical borders have to be introduced. Even if the terrain is the only physical border for the ABL it

provides some difficulties in modelling, difficulties connected to the roughness of the ground, which force to the use of wall-functions.

As regards the other boundaries, the top of the domain is treated as symmetry plane, the inlet as a velocity inlet, condition that needs the assignment of velocity and turbulence, given as profiles of mean velocity, TKE and TDR. The outlet is instead treated as outflow, i.e. all the normal gradients but the pressure gradients are imposed zero at the outlet (Neumann condition).

The vertical profiles of velocity and turbulence assigned at the inlet were supposed to regard a fully developed boundary layer for a given roughness, the same roughness assigned to the ground; in this way the profiles of velocity and turbulence should not change within the domain.

The difference of profiles observed between outlet and inlet in simulation of fully developed flows are therefore due to errors in the expression of the inlet profiles and usage of wall boundary condition.

The analytical expression of mean velocity, TKE and TDR vertical profiles assigned at the inlet are:

Mean velocity $$U(z) = \frac{u_\tau}{\kappa} \ln\left(\frac{z}{z_0}\right) \quad \Rightarrow \quad \phi_m = 1 \qquad \textbf{(3.1)}$$

TKE $$k(z) = \frac{u_\tau^2}{\sqrt{C_\mu}}\left[1 - \left(\frac{z}{z_h}\right)\right]^2 \qquad \textbf{(3.2)}$$

TDR $$\varepsilon(z) = \frac{1}{\kappa}\frac{u_\tau^3}{z} \qquad \textbf{(3.3)}$$

Where the (3.1) is the log-law introduced in the paragraph 1.3 on similarity theory; the (3.2) and (3.3) match the boundary conditions for TKE and TDR used in the code at the wall and provide also a proper reduction of TKE and TDR from the wall to the free flow, they have been also used quite successfully in Mandas *et al.* (2004) [23] using Fluent and by Leroy (1999) [21] using the finite-volume CFD code PHOENICS.

Further velocity and turbulence profiles could be obtained for instance by using transitional periodic conditions (streamwise) over flat terrains. In the periodic streamwise condition the variables calculated at the outlet are assigned to the inlet, with the possibility to point to a given mass flow, in this way a fully developed flow can be obtained. Even if not reported some RANS simulation have been performed using transitional periodic boundaries, especially as starting point for the LES/DES simulations reported in Chapter 5. Periodic conditions that are in this way useful to test furthermore the wall functions modified for rough surfaces by verifying the settings of the roughness parameters K_S (RH) and C_S (RC).

3.4 RESULTS: VELOCITY PROFILES

The aim of the 2D numerical simulations of flat terrains is to confirm that the vertical profiles of velocity and turbulence given by equations (3.1)-(3.3) are typical of a fully developed boundary layer. Moreover, simulations on flat terrains allow to understand how to set the roughness parameters RH and RC in order to reproduce the same roughness length of the profiles imposed at the inlet. In this set of simulations the desired flow field is a fully developed, fully-rough turbulent boundary layer, hence with the advective term that should drop to zero in the whole domain.

In the present paragraph the numerical results u(z) and ϕ_m observed at the outlet of the domain are presented for a roughness length z_0 0,03 m (RH 0,2943 m, RC 1, h 0,6 m), in Figure 3.1 and Figure 3.3. The velocity profile observed at the outlet of the domain is fairly logarithmic and the points are scattered with a squared correlation factor R^2 of 0,9979 for an exponential regression computed over the first seven nodes. The roughness length at the outlet computed with the regression is 0,0439 m while the desired value is 0,03 m. There are two ways to further improve the prediction of the roughness length: the first one is to slightly reduce the RH factor (or K_S) keeping constant RC (or C_S) while the second one is to increase RC and assign RH according to equation (2.33) ($C_S K_S \approx E z_0$) and then adjust RH if necessary. Roughness constants RC higher than one in

Fluent 6.2 must be assigned with "profile" files, whose structure and procedure for reading is explained in code users' manual [10]. It's important to note that reducing the roughness height RH allows to refine furthermore the grid in wall normal direction since the height of the wall adjacent cell has to be at least twice RH. For instance, with RH 0,25 m and RC 1 a better prediction of roughness length is obtained for a target of z_0 0,03 m, see Figure 3.2.

The normalised wind-shear ϕ_m, defined in the section on similarity theory in Chapter 1, equals one in a perfectly logarithmic velocity profile. In Figure 3.3 the normalised wind shear obtained in the same conditions of Figure 3.1 is equals to 1 ± 0,1 which is clearly acceptable; the behaviour observed close to the top of the domain in Figure 3.3 is forced by the symmetry boundary condition and not disturbing the flow field since confined to the very upper region.

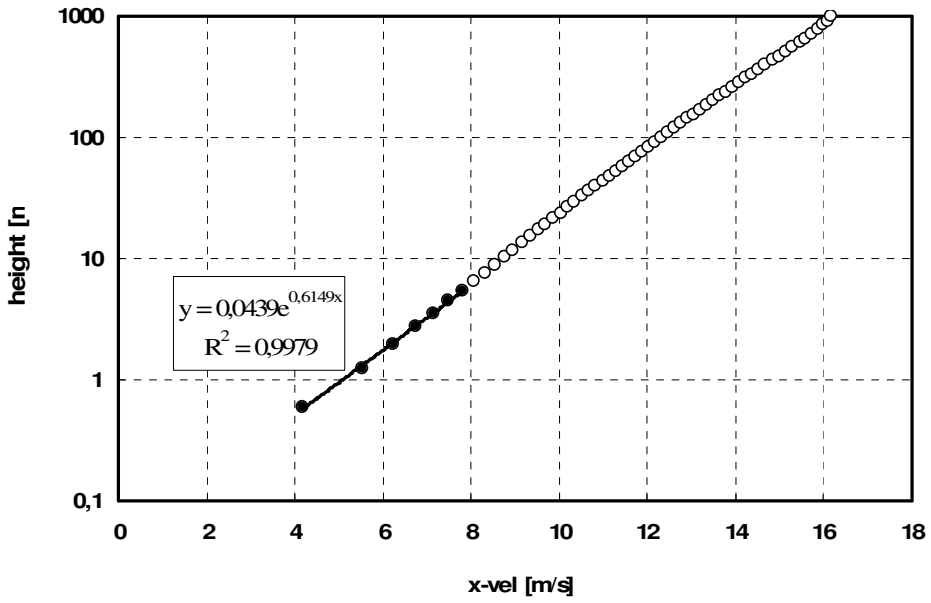

Figure 3.1 – velocity profile at outlet for RH 0,2943 m as in Table 3.1 and according to equation (2.33).

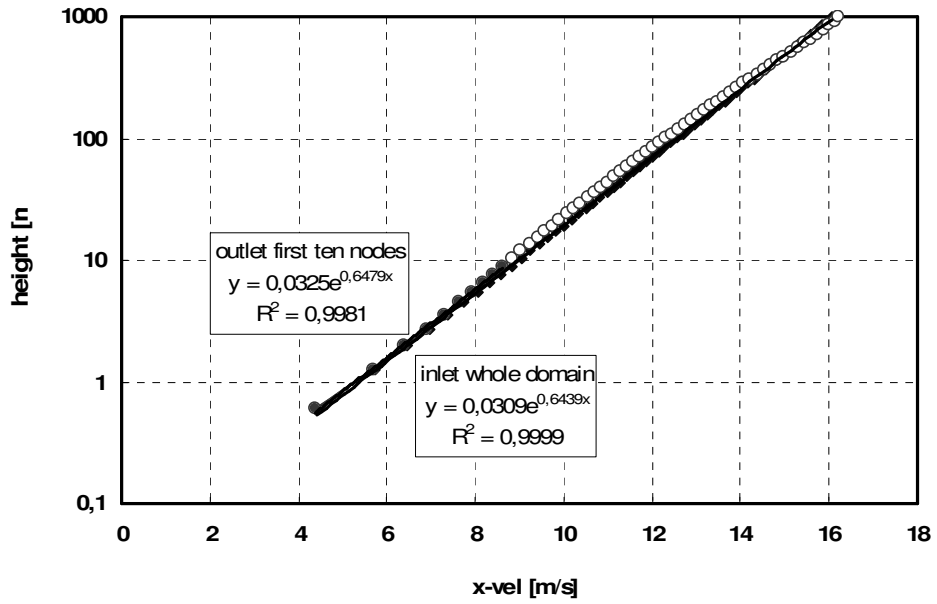

Figure 3.2 – velocity profiles at inlet and outlet for the same settings of Figure 3.1 except RH 0,25 m.

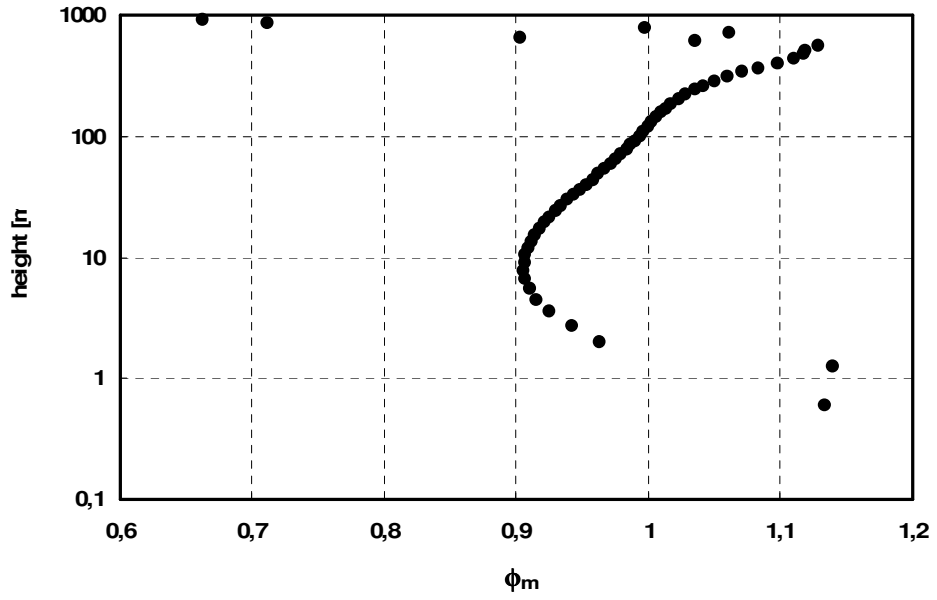

Figure 3.3 – normalised wind shear extracted at the same section and for the same simulation of Figure 3.1.

For other two cases the roughness constant RH has been tuned to obtain a better prediction of the roughness length z_0; both first attempt and tuned values are reported in Table 3.3 where the correlation factor is referred to the first five nodes, excluded the one on the ground.

Table 3.3 – Tuned values of RH parameter for better prediction of roughness length z_0.

Class	inlet z_0	RH [m]		RC	h [m]	z_0 predicted with tuned RH	R^2
		First	Tuned				
IV	0,03 m	0,2943	0,25	1	0,6	0,0325 m	0,9981
VI	0,16 m	1,567	1,17	1	3,2	0,199 m	0,9981
VI	0,55 m	5,3955	2,61	1	10,8	0,5397 m	0,9985

Some tests have been performed also with RC = E, RH = z_0 and h slightly higher that twice RH. More accurate predictions of roughness length are obtained in RANS steady simulations but not so satisfactory when dealing with LES/DES simulations since in this way several cells are used inside the canopy layer while the logarithmic law is valid only in the surface layer.

3.5 COMPARISON OF TURBULENCE MODELS

The simulations for the comparison of the turbulence models have been performed on a rectangular domain 1 km high and 6 km long for a roughness length z_0 0.03 m (roughness class IV).

The models tested are:

- Standard k-ε with default constants
- Standard k-ε with modified constants
- RNG k-ε with default constants
- RNG k-ε with modified constants
- Realizable k-ε with default constants

The models and relative modified constants have been already described in the previous chapter about general settings of the numerical simulations. The default and modified constant for the SKE and RNG k-ε models are reported in Table 2.3 and Table 2.4 while the other models default constants are reported in the Fluent's guide [10]. For the RSM model, some differences exist between the 2D and the 3D versions and therefore the 2D RSM tests could not be completely satisfactory in the preparation of 3D simulations. Some CFD results obtained with the RSM will be presented directly in the next chapter for 3D simulations over an isolated hill.

Several simulations have been carried out to evaluate the different behaviours of the turbulence models on a flat terrain. Geometries and meshes remain the same described in the previous paragraph. Further tests on different turbulence models will be presented in the next Chapter 1 where the flow field of the isolated hill of Askervein is investigated. The test case of Askervein is very useful to understand the performances of the turbulence models, especially in the prediction of the flow in the lee side of the hill, in an adverse pressure situation where turbulence modelling is important.

Once the turbulence profiles (3.2) and (3.3) are substituted in the equation (2.11) an eddy viscosity vertical profile is computed, shown in Figure 3.4. The value of eddy viscosity in Figure 3.4 do not depend upon the constant C_μ while depends on the friction velocity u_τ.

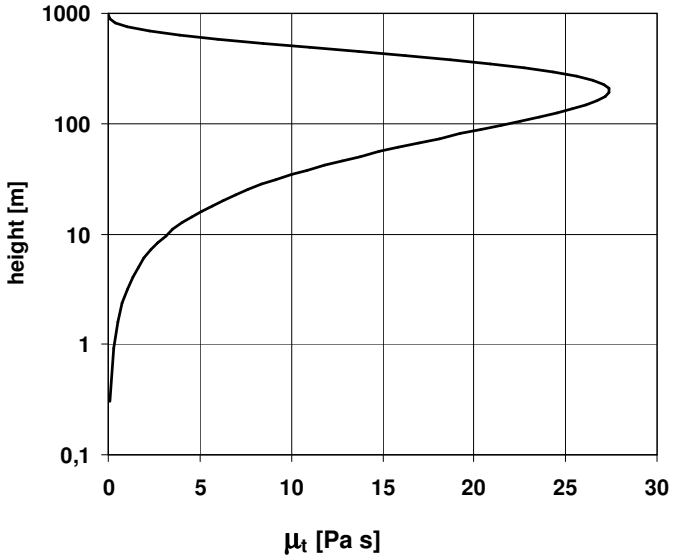

Figure 3.4 – Vertical profile of eddy viscosity according to equation (2.11) and turbulence profiles (3.2) and (3.3).

3.5.1 Profiles observed at the outlet

In the next graphs (Figure 3.5 and Figure 3.6) the TKE profile assigned at the inlet of the domain and observed at the outlet are plotted respectively for the SKE and RNG k-ε models. When an eddy viscosity model is applied it computes at each iteration the eddy viscosity which is then plugged in the momentum RANS equation. It's interesting therefore to see also if the eddy viscosity assigned at the inlet by the turbulence parameters k and ε is kept unperturbed through the whole domain to the outlet. The vertical profiles of eddy viscosity are shown in the following Figure 3.7 and Figure 3.8 for the SKE and RNG k-ε; it can be seen that in both models the TKE is slightly reduced in the domain compared to the inlet condition, but this is not so dramatic, also the eddy viscosity is maintained in all the cases but the RNG with modified constants. Therefore the SKE and the RNG can be used in the reproduction of a neutral ABL with the default constants. When there is the need to reproduce a neutral ABL, and the ratio TKE/u_τ^2 at the ground is known from experimental

data, the SKE model can be used with modified constants. The procedure for the modification of the SKE model's constants is reported in Appendix A.

The usage of the modified constants for the RNG, as in Table 2.4 is not suggested since effects caused to the eddy viscosity profile of Figure 3.8 are not satisfying. It would be necessary to derive a new set of constants for the RNG model, for instance by following a procedure similar to the one described in Appendix A for the SKE model.

3.6 2D SIMULATIONS ON AN ISOLATED HILL

Simulations on a given topography like an isolated hill rather than on a flat terrain are more significant in order to set the effects of the horizontal refinement and the discretization schemes employed. Therefore 2D tests have been performed on a hill with a symmetric shape given by the equation (3.4).

$$z(x) = \frac{H}{1 + \left(\frac{x}{L}\right)^2} \qquad \textbf{(3.4)}$$

Where the height of the hill is named H and L is half width of the hill (x = L) measured at its half height (z = H/2).

The domain analysed was 1 km high and 7 km long, the top of the hill was positioned at 1.5 km from the inlet, the hill top H was 116 m and L = 250 m.

The roughness length chosen for this series of tests was 0,03 m therefore the height of the first cell was set to 0,6m (RC = 1, RH = 0.2943 m).

Further characteristics of geometry, grids, and settings are reported in the Table 3.4.

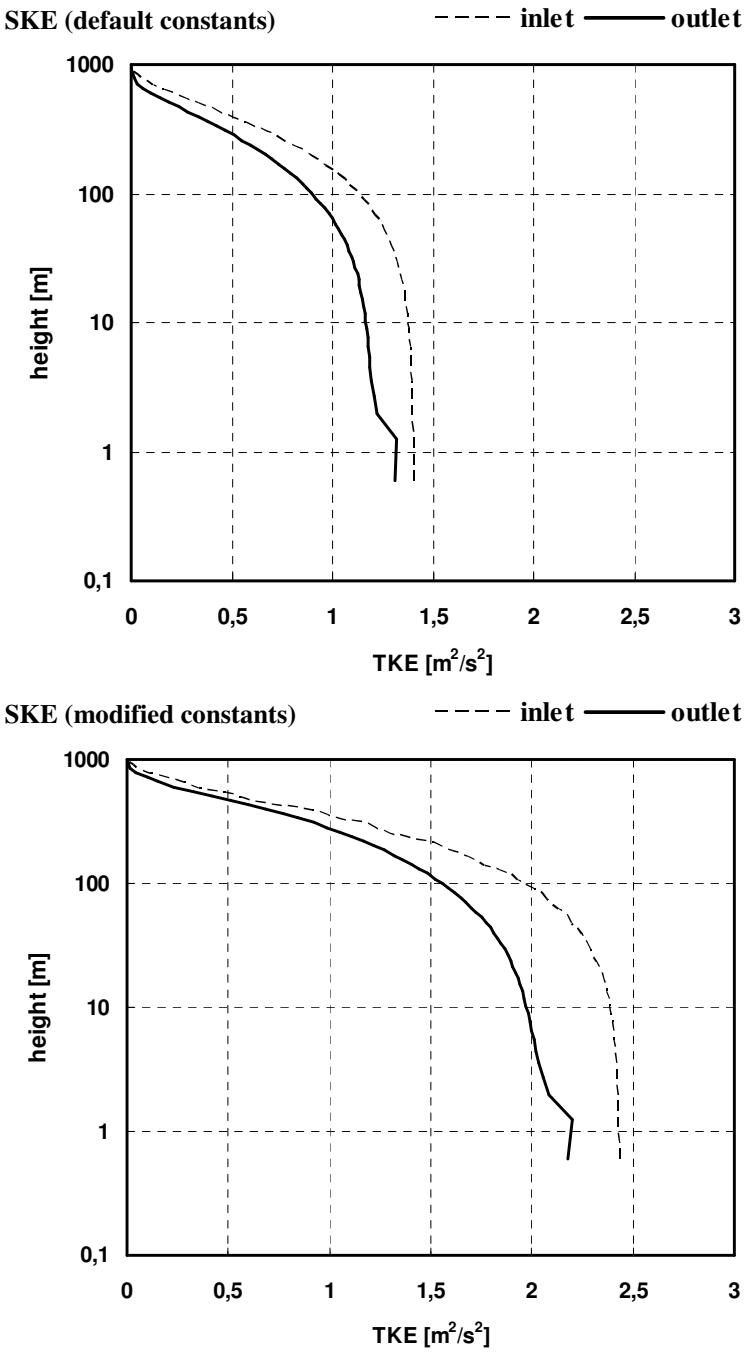

Figure 3.5 – vertical profiles of TKE for the SKE model with default and modified constants.

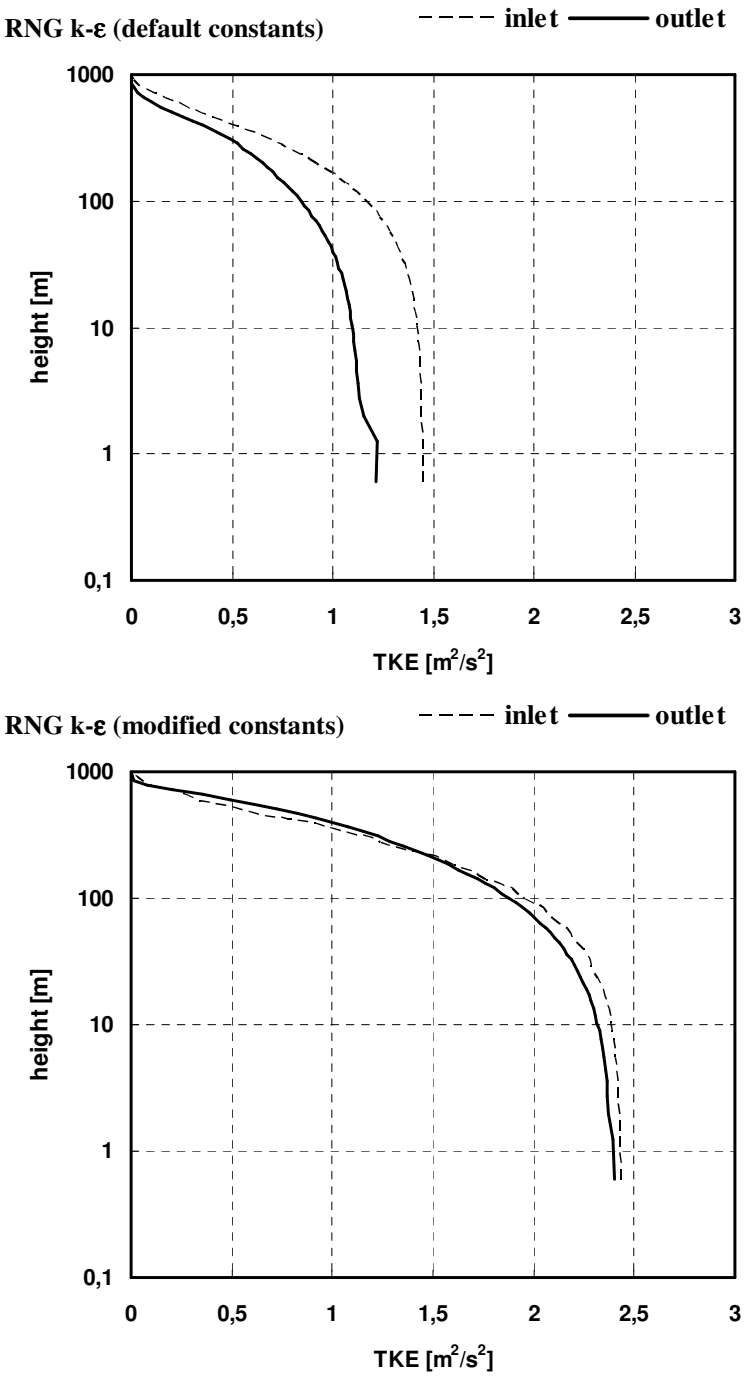

Figure 3.6 – vertical profiles of TKE, for the model RNG k-ε, for default and modified constants

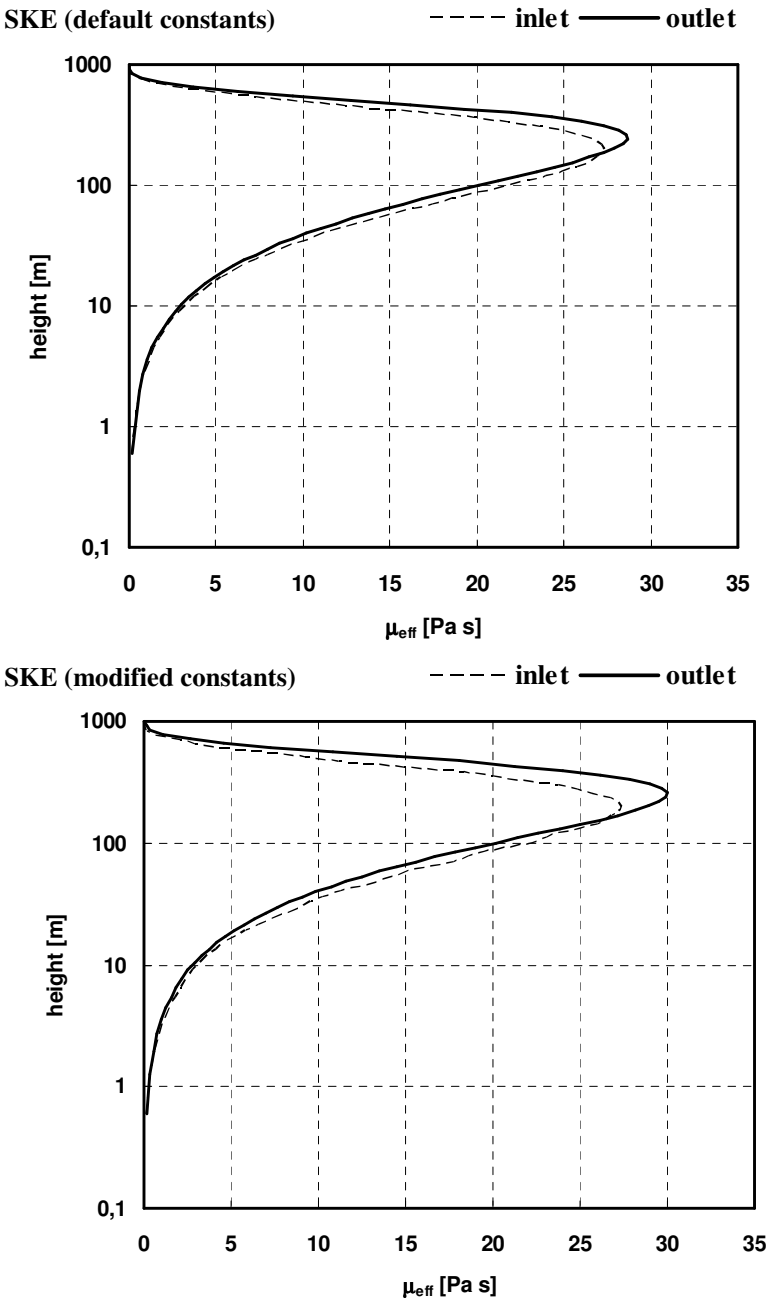

Figure 3.7 – Vertical profiles of effective viscosity for the SKE model with default and modified constants

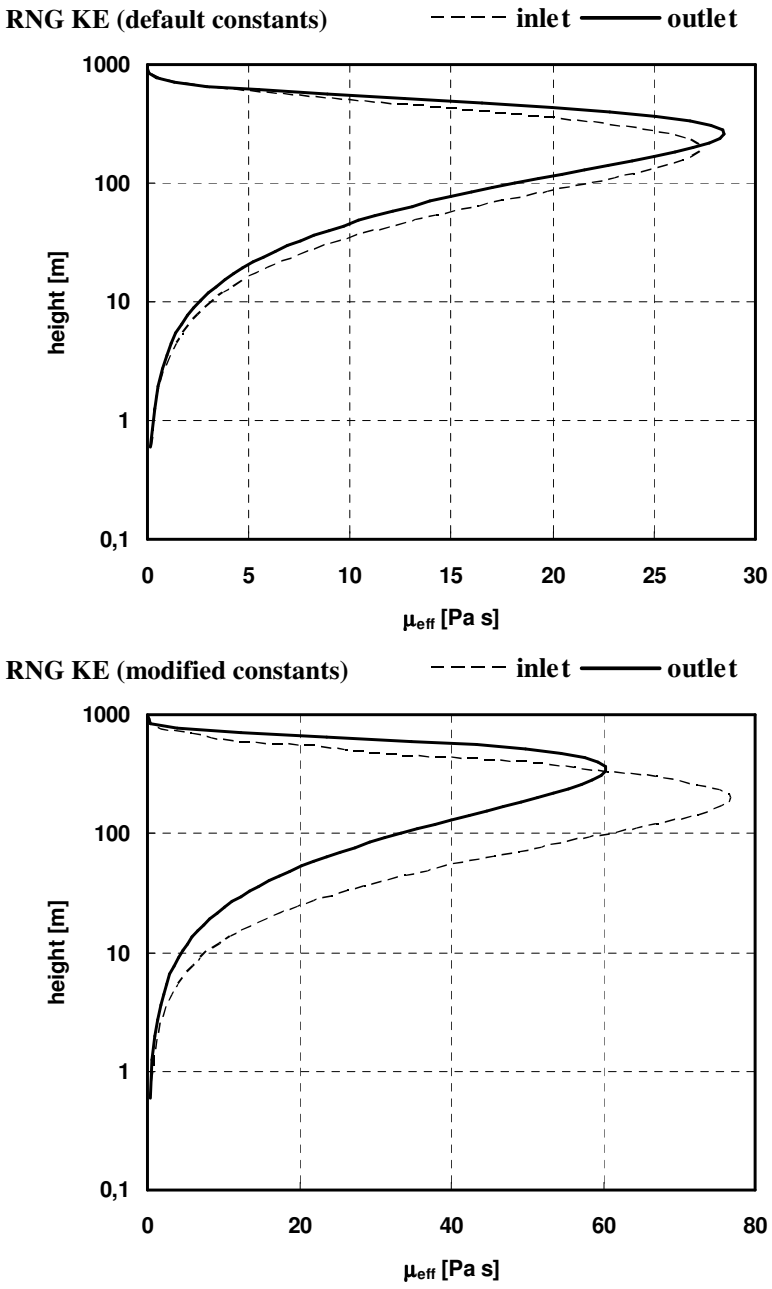

Figure 3.8 – vertical profiles of effective viscosity for the RNG k-ε model with default and modified constants

3.6.1 Choice of horizontal refinement

Five values of horizontal spacing have been chosen to study the error due to spatial discretization, see Table 3.5 for further grids details, and if a possible grid independence was reachable. For sake of simplicity the tests are carried out with the first order up-wind scheme while the next paragraph is devoted to spatial discretization schemes effects.

In Figure 3.9 the value of x-velocity is shown computed at an altitude of 10 m for the finest grid tested (5 m of resolution) and for the coarsest one (40 m of resolution) in the whole length of the domain. In the next Figure 3.10 the error due to horizontal refinement for all the cases is instead shown , in the vicinity of the hill top (above) and its rear (down). Figure 3.11 shows the same trend of Figure 3.10 but for the y-velocity.

The height of 10 m a.g.l. has been chosen to plot the velocity components since typical for anemometric measurements. For example this was the positioning height for most of he anemometers employed in the experimental campaign of Askervein which is treated in the next chapter. Other typical heights of displacement for the anemometers are 30 m and the hub height of wind turbines (for wind energy applications) that can be even 100 m a.g.l..

While in the 2D simulations performed on domains with a horizontal spacing of 5 m the time of computation resulted not acceptable, with a spacing of 10 m a good compromise is reached between accuracy of results and time of computation.

Nevertheless when the ABL is modelled over 3D domains of few kilometres square a horizontal uniform grid of 10 m resolution still leads to a total number of cells of few millions; horizontal resolution of 20 m or 30 m are therefore used if the simulations have to be carried out on a single machine.

It’s good practice to refine horizontally the grid in the area of interest, that should be rather in the core of the domain, and expand the interval size outside the area of interest towards the lateral borders. Nevertheless for the 2D tests uniform grids have been preferred in order to keep the grid as simple as possible.

Table 3.4 – Geometry, mesh, boundary conditions and some further settings for the 2D simulations on the isolated hill

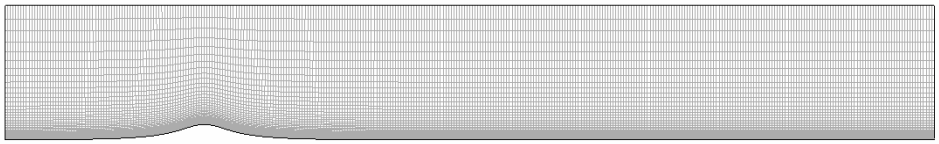

Geometry	
Lx	7000 m
Ly	1000 m
H	116 m
L	250 m
Hill x-position	1500 m from the inlet
Mesh	
Ny	50
h	0.6 m
Nx	dependent on refinement Δx
Boundary Conditions	
Inlet	Velocity Inlet
Outlet	Outflow
Top	Symmetry
Ground	Wall functions for rough surfaces
Further Settings	
Solver	Segregated
Turbulence Model	SKE (modified constants)
Pressure-Velocity Coupling	SIMPLEC
Pressure Discretization	PRESTO!

Table 3.5 – Horizontal resolution and total number of cells for 2D tests on the hill

Δx [m]	5	10	20	30	40
N	70,000	35,000	17,500	11,650	8,750

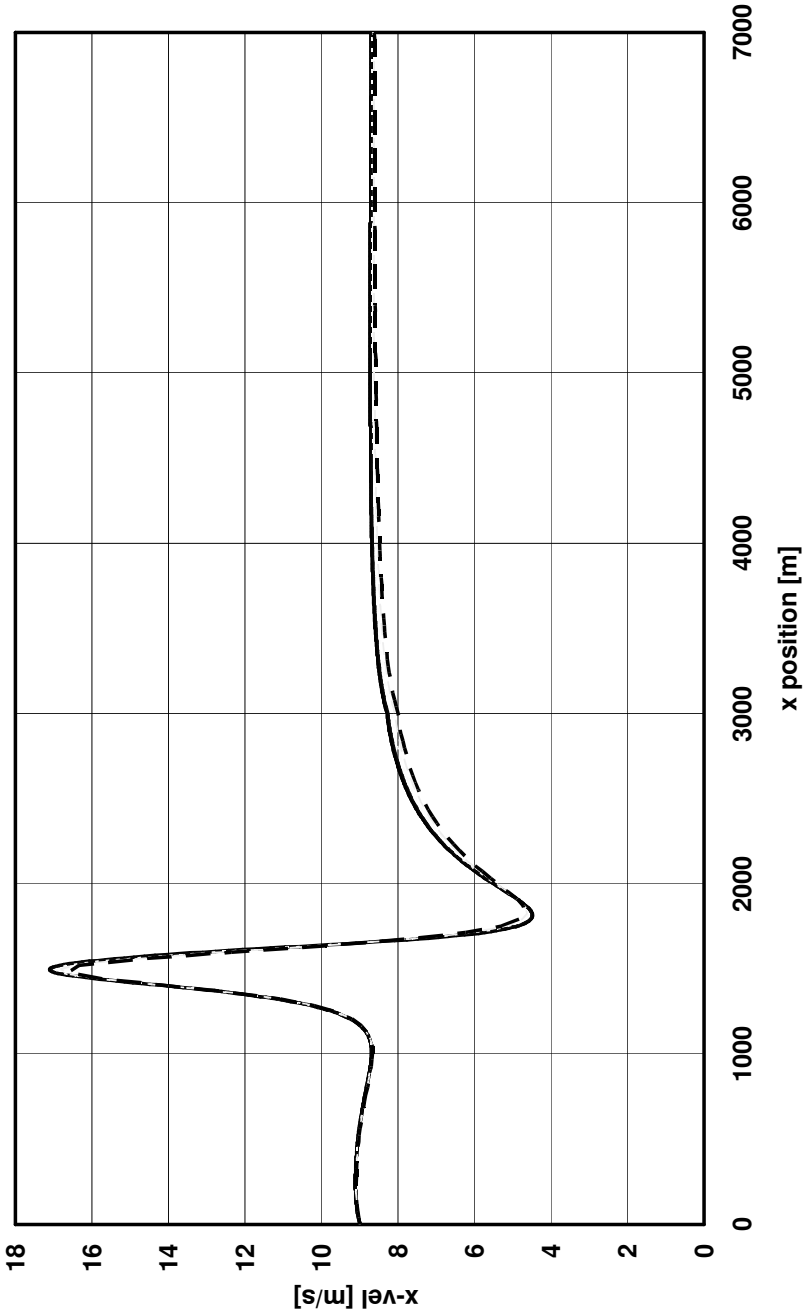

Figure 3.9 – x-velocity computed at 10 m a.g.l. for 5 m spacing (solid line) and 40 m spacing (dashed line)

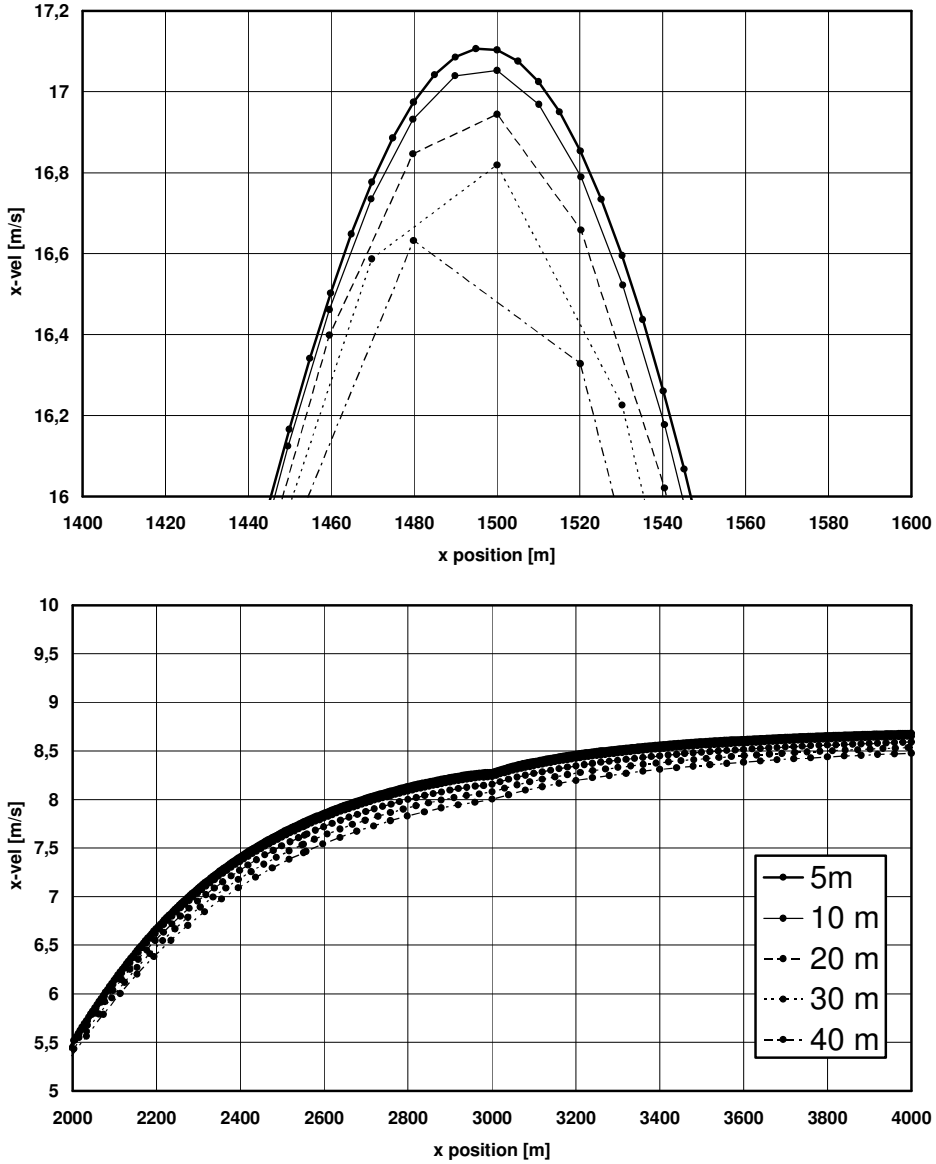

Figure 3.10 – Spatial refinement effects, x- velocity at 10 m altitude

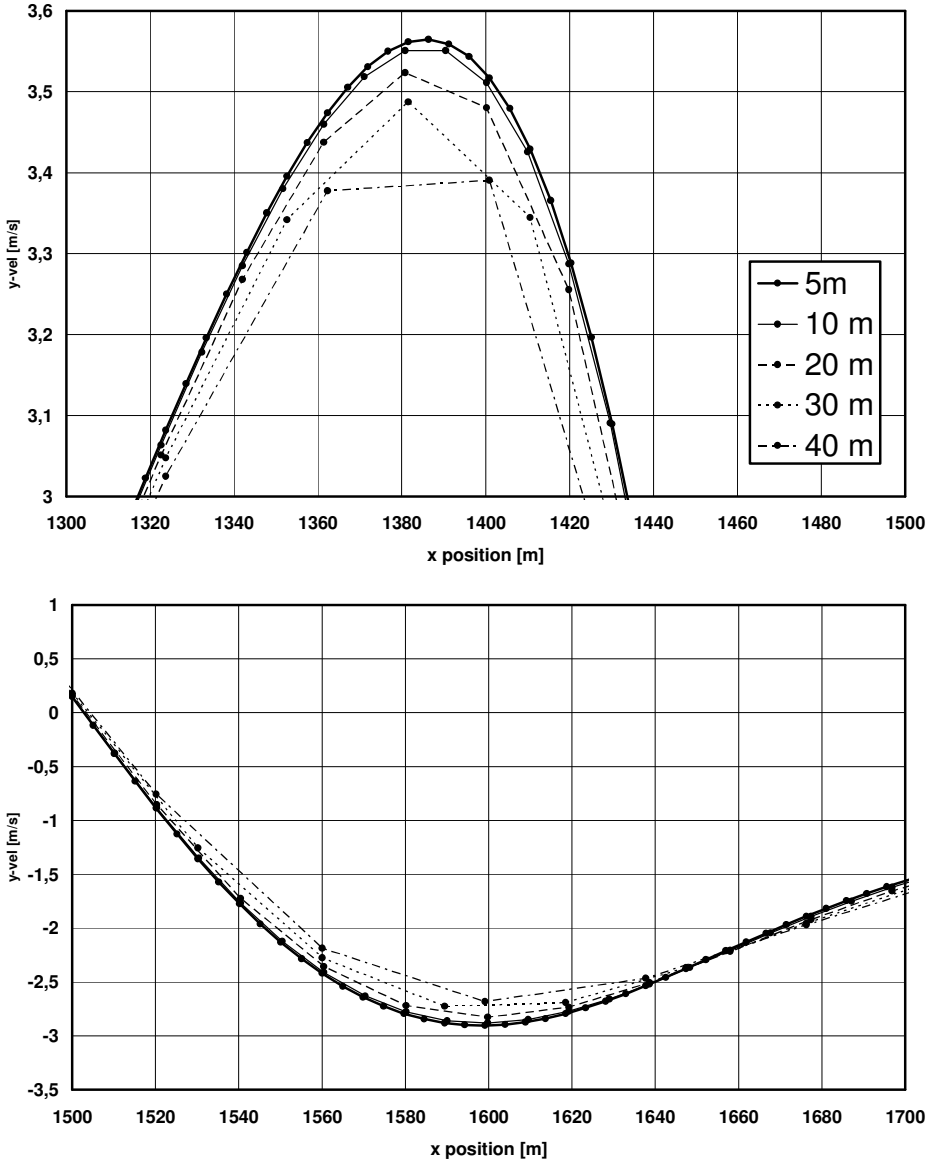

Figure 3.11 – Spatial refinement effects, y-velocity at 10 m altitude

3.6.2 Choice of discretization scheme

Fluent 6.2 allows to model the convection terms of each governing equation with different types of discretization schemes (viscous term is always modelled with a central scheme with second order accuracy). In the settings employed, summarised in Table 3.4, the possible discretization schemes for the convection terms are the up-wind first and second order, the power-law scheme, the third order MUSCL and the QUICK, which is a weighted average of a second order up-wind and a second-order central scheme; they are all described in the Fluent User's Guide [10] and related references.

Figure 3.12 (above) shows how the peak of velocity observed at 10 m a.g.l. in proximity of the hill top is better predicted with second order and third order schemes while first order up-wind and power-law introduce probably too much numerical viscosity and therefore poor prediction; also in the rear of the hill, see Figure 3.12 (down), approximately at three kilometres from the inlet the effects of the discretization scheme can be appreciated; the choice of the discretization scheme is therefore pushed to a second order up-wind scheme for all the governing equations since the use of an higher order scheme doesn't look motivated. The plot of the vertical component shows a behaviour similar to the horizontal component, therefore it will not be shown.

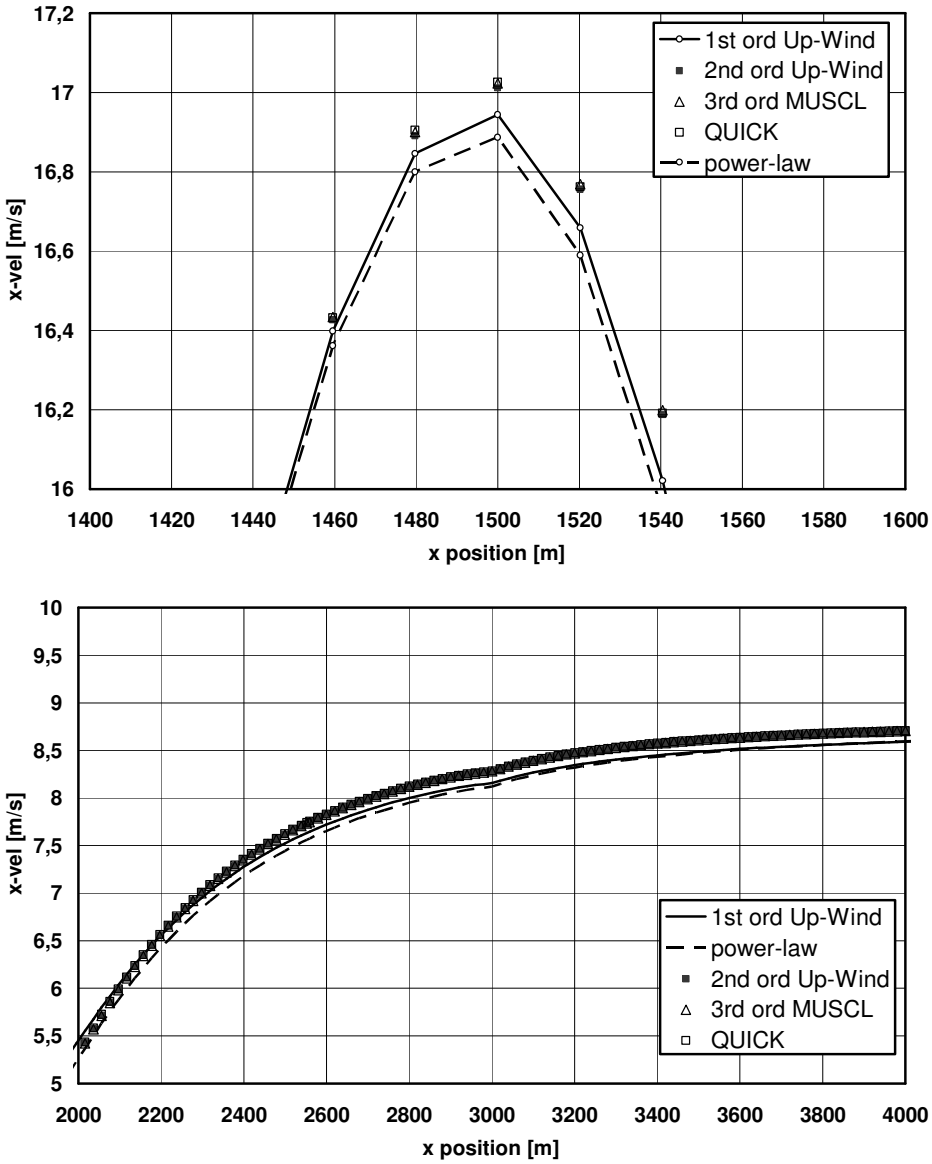

Figure 3.12 – Discretization schemes' effects, x-velocity at 10 m a.g.l., on the hill top (up) and rear (down)

Chapter 4 3D RANS SIMULATIONS OVER AN ISOLATED HILL

4.1 INTRODUCTION

The validity of a new CFD technique should be validated whenever possible by means of comparisons with experimental data. One of the most employed test-cases for the numerical analysis of the propagation of the ABL around isolated hills is the wind field observed on the hill of Askervein during the two experimental campaigns in September/October ’82 and ’83 carried out by a team of researchers coming from different institutions in the world.

The research groups which took part to the Askervein project were the Atmospheric Environment Service (AES), in Canada, the Risø national laboratory, in Denmark, the University of Hannover, in Germany, the University of Canterbury, in New Zealand, the Building Research Establishment and the ERA Technology Ltd, both located in the United Kingdom. Although the measurements gathered on the Askervein hill are nowadays more than twenty years old, the big amount of data available is still an important reference point for those researchers who want to investigate the flow over hilly terrains.

The experimental results of the Askervein hill project are reported in *Taylor and Teunissen (1983)* [34] for the ’82 data and in *Taylor and Teunissen (1985)* [36] for the ’83 data. A comprehensive description of the experimental set ups and instruments can be found in *Taylor and Teunissen (1986)* [37] together with a selection of the experimental results.

After the publication of the gathered data by the involved institutions several researchers tried to reproduce with numerical codes the flow field observed on the Askervein hill.

Castro et al. (2003) [5] performed a series of numerical RANS simulations reproducing some of the experimental runs, the TU03-B, MF03-D and TK03 as named in *Taylor and Teunissen (1985)* [36], the considered incoming wind

direction was 210° measured clockwise from north while the stratification was nearly neutral.

The turbulence model employed by *Castro et al.* (2003) [5] was the SKE with the constants of the model ($C_{1\varepsilon}$ = 1.44, $C_{2\varepsilon}$ = 1.92 and σ_k = 1.0) set as in Launder and Spalding (1972), whereas the constants C_μ and σ_ε followed the recommendations by *Beljaars et al. (1987)* [3] (C_μ = 0.033 and σ_ε = 1.85).

Castro et al. (2003) [5] proposed to pass from a steady to an unsteady state analysis since in their RANS simulations in the lee side of the hill, close to the hill top, the flow variables were oscillating around a mean value; in a unsteady simulation an intermittent separation bubble is likely to occur as observed in few of the experimental runs. If this is the case of the run TU03-B only an unsteady simulation can reproduce correctly the flow field in the lee side of the hill.

The simulations run by *Stangroom (2004)* [32] on the hill of Askervein dealt with the incoming flow at 180° and 210°. For the 180° direction the reproduced run was the MF01-D e TU01-B while for the 210° the runs of reference are the already mentioned TU03-B, MF03-D e TK03. The simulations presented in *Stangroom (2004)* [32] were run with the commercial code CFX, the grids employed were unstructured with few layers of prismatic cells adjacent to the terrain. *Stangroom (2004)* [32] adopted the RNG k-ε and the RSM turbulence models in the RANS simulations over Askervein hill. The RNG k-ε model predicted the flow field in a manner comparable to the RSM. Depending on the wind direction and area of the domain, the experimental results were sometime closer to the RNG prediction and sometime closer to the RSM prediction. Vertical profiles of turbulence (TKE or σ_u) over the hill top obtained with RNG k-ε and RSM models are also shown in *Stangroom (2004)* [32], that have been compared to the experimental data collected with propeller and sonic anemometers. Both the turbulence models underpredicted the measured level of turbulence, with a higher error for the RNG k-ε.

4.2 SIMULATIONS ON ASKERVEIN HILL

4.2.1 General description

The hill of Askervein resembles a semi-ellipsoid with axes of few kilometers with the hill top (HT) located few hundreds of meters far from its centre point (CP). The topography of the hill is plotted in Figure 4.1, where the measurements points CP, HT and RS are shown together with the points of deployment of the propeller anemometers GILL UVW located at 10 m a.g.l. along the line A passing through the hill top HT. Other two reference lines were the line AA, parallel to the line A but passing through CP, and the line B, passing through HT and CP, along the major axis.

Two digital maps of the area are available: the map-A that covers an area of 16 x 16 km^2 and the map-B that covers an area of 6 x 6 km^2, both made by 256 x 256 points, the horizontal resolution of map-A being therefore 62.5 m while the map-B has a resolution of 23.4 m. Moreover the map-A describes the hills surrounding Askervein hill while the map-B shows only the hill isolated. Both maps are shown in Figure 4.2. The whole topography described by map-A is provided in Figure 4.3 together with the extension of map-B.

Since the presence of the mentioned group of neighbouring hills most of the experimental runs performed by the research groups were relative to wind blowing from the third and the fourth sector, directions for which the hills close to Askervein are supposed to not affect the flow field around the hill.

The higher resolution of map-B provides a slightly higher altitude at the summit of the hill; a less smoothed topography could lead to numerical results much closer to the experimental.

It's not possible to state, without performing simulations, which one of the two maps could lead to the best prediction: map-A, enclosing a wider area and neighbouring topographies, or map-B, with an higher resolution.

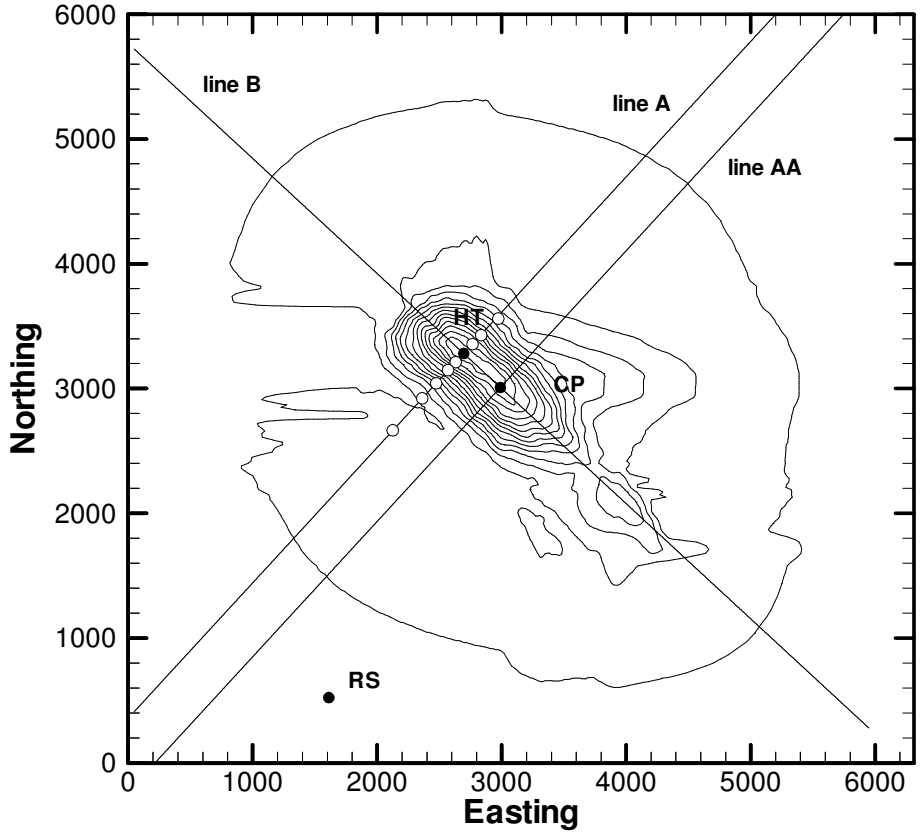

Figure 4.1 – topography of Askervein hill, Reference Site (RS), Hill Top (HT) and Centre Point (CP), obtained from map-B.

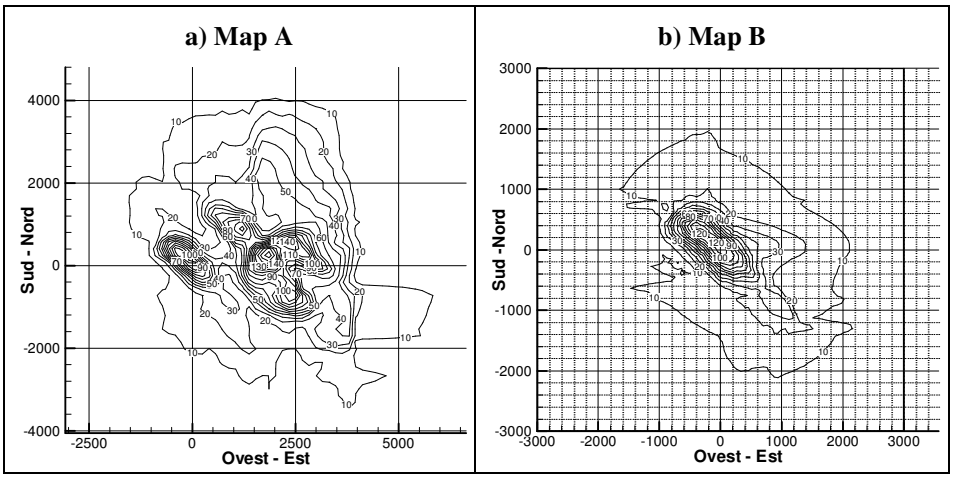

Figure 4.2 – Maps A (a detail) and B (the whole map) of Askervein Hill

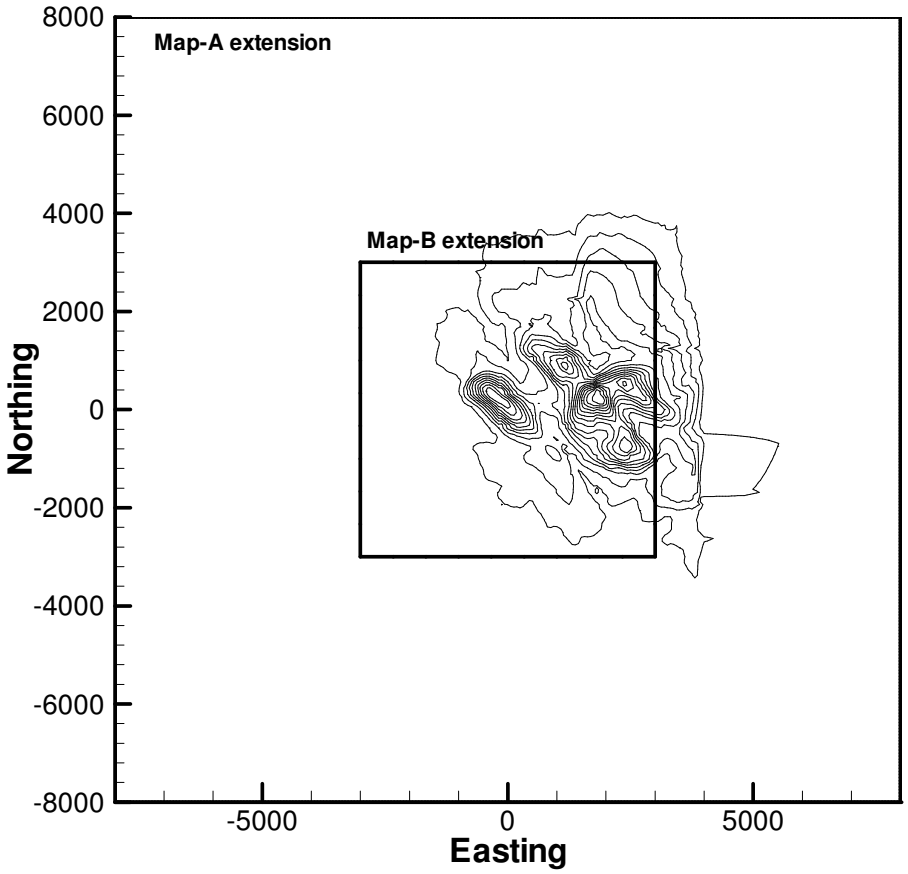

Figure 4.3 – Extensions of map-A and map-B over the topography described by map-A.

4.2.2 Measurement reference data

Among all the data gathered during the two campaigns, it has been chosen to simulate the run TU03-B. During this run the wind was blowing almost constantly for three hours from a direction of 210°, a direction almost perpendicular to the main axis of the hill, for which the hills at the east of Askervein would produce no or minimal effects on the flow-field, moreover during the run TU03-B the stratification was neutral, therefore stability effects can be neglected simulating this run.

From the report of the experiments by *Taylor and Teunissen (1985)* [36] it is extracted the Table 4.1 which shows part of the results obtained with the GILL UVW anemometers displaced along line A and at the RS point.

The same horizontal velocities listed in the second column of Table 4.1 are then plotted in Figure 4.4 along line A. Considering the definition of TKE as given by equation (1.9) and the standard deviations of the velocity components in Table 4.1 the TKE is calculated and plotted against the horizontal position along the line A in Figure 4.5. The standard deviations of the velocity components, also reported in Table 4.1, are plotted in Figure 4.6 against the horizontal position along line A of the measurement points at 10 m ag.l..

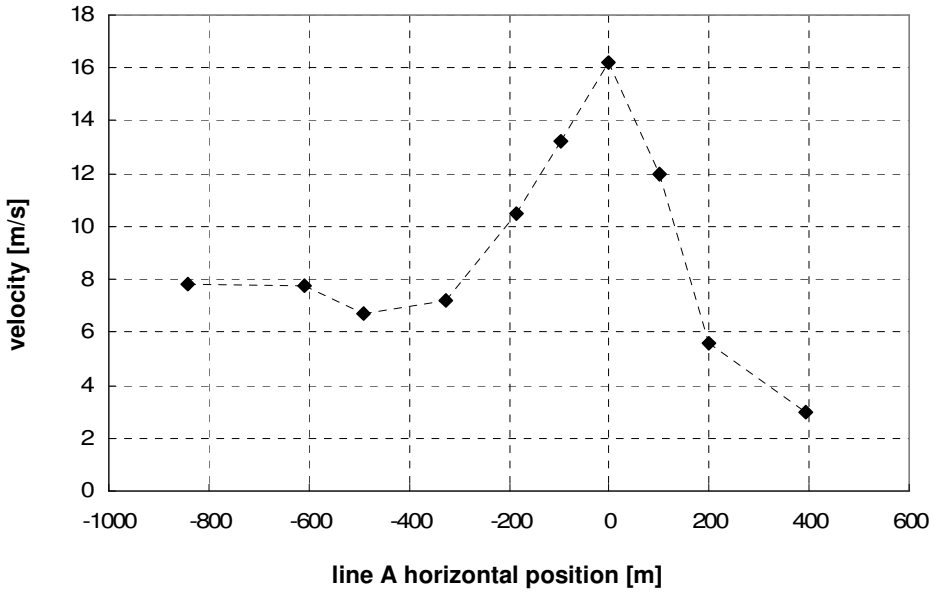

Figure 4.4 – Horizontal velocity measured at 10 m a.g.l. along line A by GILL UVW anemometers (as in Table 4.1).

Table 4.1– Averaged data from GILL UVW anemometers for turbulence run TU03-B (extracted from table A1.3 of Taylor and Teunissen (1985) [36]).

Twr lcn	Direct.	Speed	σ_u	Int U	σ_v	Int V	σ_w	Int W	uv	uw	vw
RS	207.3	8.6	1.223	0.143	0.704	0.082	0.413	0.048	0.135	-0.247	-0.013
ASW85	201.6	7.8	1.200	0.153	0.762	0.097	0.463	0.059	0.007	-0.239	0.002
ASW50	192.9	6.7	1.350	0.202	0.683	0.102	0.475	0.071	0.099	-0.272	0.015
ASW35	196.0	7.2	1.243	0.174	1.038	0.145	0.580	0.081	0.042	-0.351	-0.033
ASW20	200.6	10.5	1.115	0.107	1.126	0.107	0.565	0.054	0.032	-0.287	-0.004
ASW10	207.9	13.2	1.059	0.080	1.232	0.093	0.577	0.044	0.098	-0.243	-0.049
HT	203.4	16.2	1.100	0.068	1.034	0.064	0.577	0.036	0.189	-0.153	0.031
ANE10	206.5	12.0	1.758	0.146	1.012	0.084	0.531	0.044	-0.004	-0.241	0.056
ANE20	195.9	5.6	2.560	0.458	1.502	0.269	0.881	0.158	-1.431	-0.560	0.206
ANE40	188.1	3.0	1.983	0.668	1.798	0.606	1.192	0.402	-0.275	0.694	0.459

Legend:

Twr lcn	tower location (name)
Direct.	direction, measured in degrees clockwise from north
Speed	horizontal wind speed
σ_u	estimator of standard deviation of streamwise component of velocity
Int U	streamwise turbulent intensity ($=\sigma_u$/Speed)
σ_v	estimator of standard deviation of spanwise component of velocity
Int V	spanwise turbulent intensity ($=\sigma_v$/Speed)
σ_w	estimator of standard deviation of vertical component of velocity
Int W	vertical turbulent intensity ($=\sigma_w$/Speed)
uv	covariance streamwise-spanwise
uw	covariance streamwise-vertical
vw	covariance spanwise-vertical

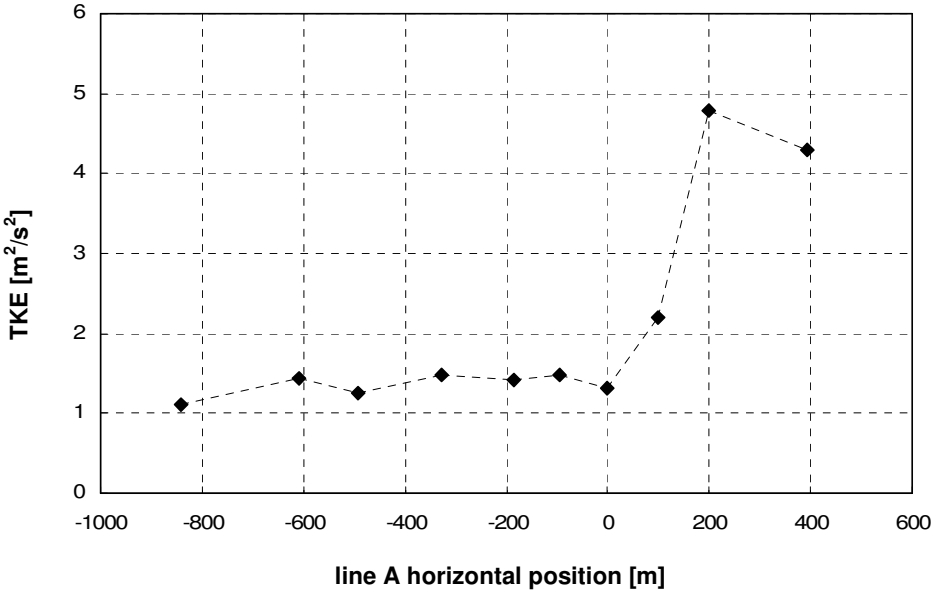

Figure 4.5 – TKE computed with (1.9) and standard deviations of velocity components measured at 10 m a.g.l. along line A by GILL UVW anemometers (as in Table 4.1).

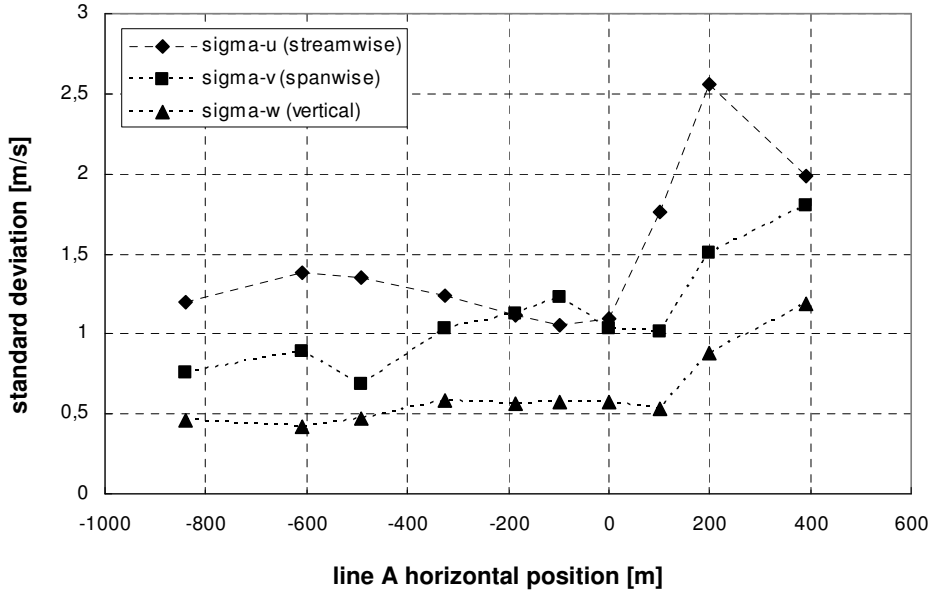

Figure 4.6 – Standard deviations of velocity components measured at 10 m a.g.l. along line A by GILL UVW anemometers (as in Table 4.1).

Considering valid a log-law (1.3) at the reference site RS and assuming a roughness length z_0 of 0.03 m, a friction velocity of 0.634 m/s is computed by exponential interpolation (with κ 0.41); if the roughness length is not fixed the regression provides a roughness length of 0.0486 m and a friction velocity of 0.685 m/s; experimental data and regression curves are reported in Figure 4.7.

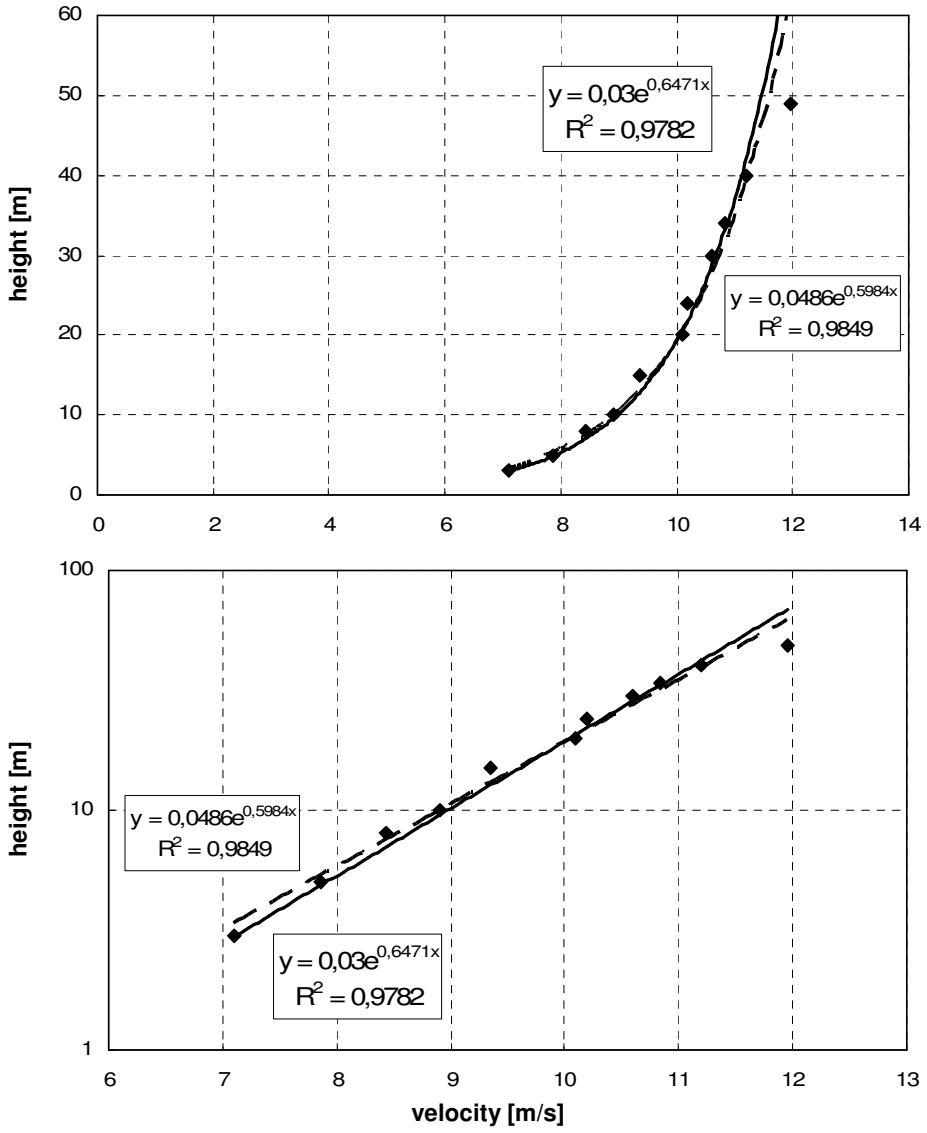

Figure 4.7 – Vertical profile of mean horizontal velocity at RS during TU03-B run (from Taylor e Teunissen (1985) [36]) and exponential interpolations.

The values of TKE measured at RS are instead plotted in Figure 4.8, they can be used to evaluate the SKE C_μ constant: if the value of C_μ 0.09 is kept (default in Fluent) then the TKE values measured by the GILL UVW at the RS are approximately matched by equation (3.2), see Figure 4.9. This observation allows the usage of the default values for the SKE model's constants and also for the other models' constants in the simulations of the TU03-B run, performed in neutral conditions. Considering the velocity's standard deviation measured at RS (table A1.6 and A1.7 of *Taylor and Teunissen (1985)* [36]), also a vertical profile of TKE has been constructed, shown in Figure 4.8. The constructed vertical profiles of both velocity and turbulence should resemble the profiles assigned at the inlet of the computational domains.

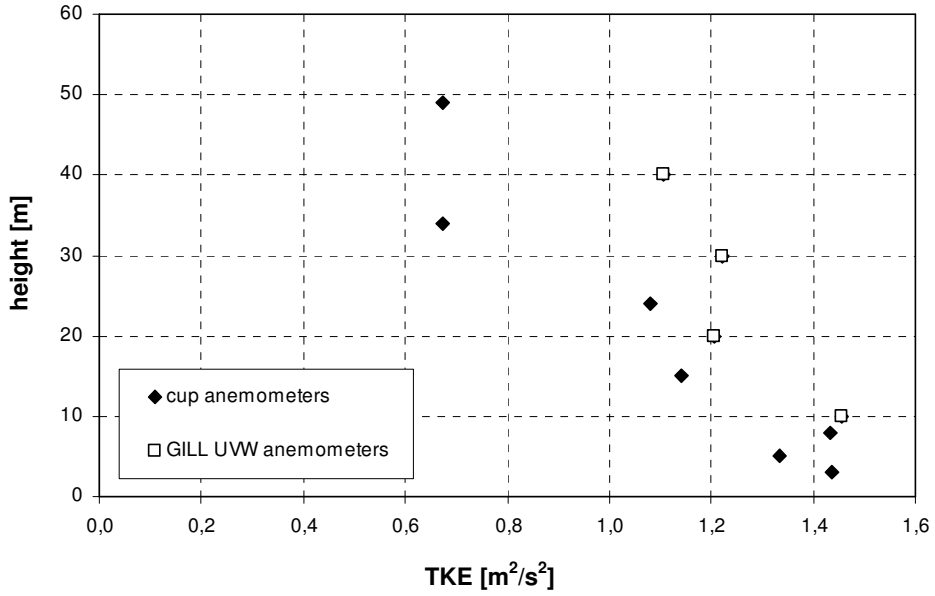

Figure 4.8 – Vertical profile of TKE obtained from turbulence measurements (tables A1.6 and A1.7 of Taylor and Teunissen (1985) [36]).

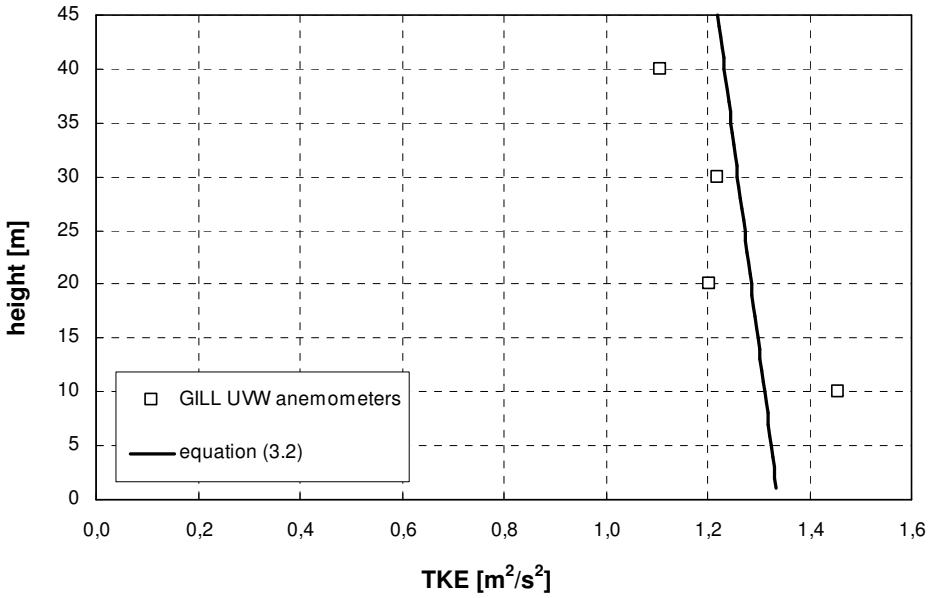

Figure 4.9– TKE values measured by the GILL UVW anemometers at RS during the run TU03-B and profile given by equation (3.2) with C_μ 0.09 and friction velocity 0.634 m/s (solid line).

4.2.3 Simulations with Fluent

A series of 3D simulations have been carried out with the commercial code Fluent on the isolated hill of Askervein. Both maps A and B are used in order to study the effects of the original resolution and influences to the flow of the group of hills at east of Askervein.

For both the maps a geometry of 3 km x 6 km enclosing the hill has been drawn in order to have the sides of the computational domain parallel to the incoming wind (210°). The height of the computational domain has been set to 1 km while the hill of Askervein is placed approximately 1.6 km far from the inlet border.

A view of part of the meshed borders for the computational domain obtained from map-A is shown in Figure 4.10, above the whole domain containing the hill of Askervein.

Further details of the geometry and grid are provided in the Table 4.2 while the boundary conditions employed are summarised in Table 4.3.

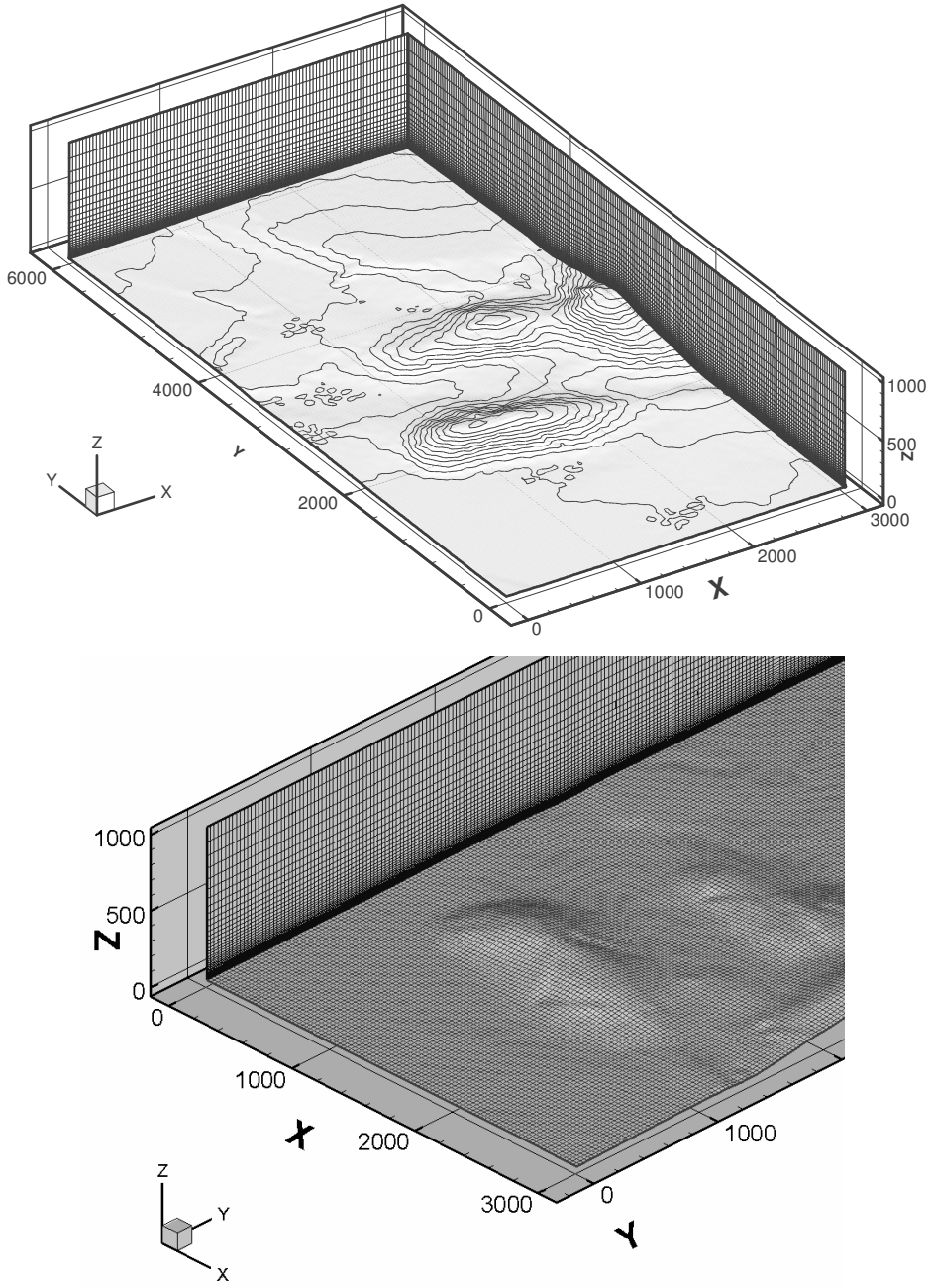

Figure 4.10 – Grid obtained from map-A.

Table 4.2 – Geometric characteristics of the meshes used for TU03-B runs comparisons

Height of the domain	1000 m
Width domain (dir. x, spanwise)	3000 m
Length domain (dir. y, streamwise)	6000 m
Height of wall adjacent cell (h)	0.6 m (z_0 0.03 m – RC 1 – RH 0,2943 m)
Width cells (Δx, Δy)	30 m
Number of vertical divisions	50
Number of horizontal divisions	100 x-axis, 200 y-axis
Total number of cells	1 000 000

Table 4.3 – Boundary Conditions

Inlet	Velocity Inlet
Left side	Symmetry
Right side	Symmetry
Outlet	Pressure Outlet (map-A), hydrostatic model
	Outflow (map-B)
Terrain	Wall with wall-functions
Top (geostrophic wind)	Symmetry

Several turbulence models have been tested in RANS simulations with the described geometry, grid and boundary conditions; the turbulence models employed are reported in Table 4.4.

Table 4.4 – Turbulence models employed in the presented RANS simulations run with the code Fluent.

	Map-A	**Discretization scheme for advection term**
SKE	default constants	2nd order upwind (momentum, k and ε)
RNG k-ε*	default constants	2nd order upwind (momentum, k and ε)
RKE	default constants	2nd order upwind (momentum, k and ε)
RSM	default constants	2nd order upwind (momentum, k, ε and Reynolds' stresses)
	Map-B	
SKE	default constants	2nd order upwind (momentum, k and ε)
RNG k-ε*	default constants	2nd order upwind (momentum, k and ε)
RKE	default constants	2nd order upwind (momentum, k and ε)
RSM	default constants	2nd order upwind (momentum, k, ε and Reynolds' stresses)

* with the Differential Viscosity model activated, see the Fluent User's Guide [10] for the option's description

4.2.3.1 Results: mean flow and turbulence

The horizontal velocity measured in the run TU03-B is plotted in Figure 4.11, where the vertical bars are proportional to the standard deviation of the stream wise velocity and where the horizontal velocities obtained with the SKE model in both maps are also shown. The two SKE simulations forecasted well the flow up stream of the hill while the peak of velocity at the top resulted slightly under predicted, a feature which is common in the reproduction of the Askervein flow, see e.g. the plots presented by *Castro et al. (2003)* [5], an under prediction of velocity that can be explained certainly by the too coarse meshes originated from both maps. In fact, also in the 2D simulations of Chapter 1 about an isolated hill it was already shown that an horizontal resolution of 30 m leads to a poor prediction of the wind peak at the top of the hill. Therefore improvements could be expected refining the grids especially around the summit of the hill.

The under prediction of the wind peak at the top of the hill has been also explained in literature (*Castro et al. (2003)* [5]) by a roughness of the terrain around the top of the hill smoother than the one considered.

The wind down stream of the hill is instead over predicted by both the simulations based on the two maps, in the lee side of the hill, in an adverse pressure-gradient flow, the turbulence model plays an important rule. The flow downstream is not well captured because of the turbulence modelling. Differences can be noticed between the wind predictions of the two simulations, the map obtained from map-B looks behaving better than the one obtained from map-A. It seems therefore that the neighbouring hills do not affect significantly the flow at the lee side of the hill, while the higher resolution of map-B would lead to a better prediction of the flow.

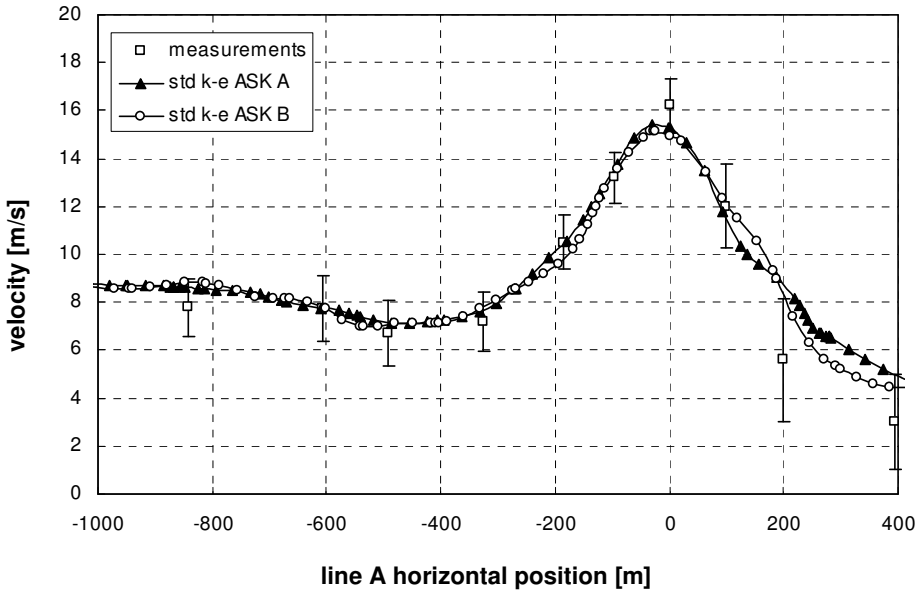

Figure 4.11 – Horizontal velocity along line A (10 m a.g.l.), SKE model map-A and map-B.

The same experimental data of horizontal velocity and bars proportional to streamwise velocity standard deviation are used in Figure 4.12 and Figure 4.13, respectively for map-A and map-B, to make comparisons of four turbulence models (SKE, RNG KE, RKE and RSM).

In Figure 4.12 and Figure 4.13 is shown how the mean flow along the line A in the ups stream region and on the top of the hill is basically described in the same manner by all the turbulence models employed. The flow in lee side, in the adverse pressure gradient region, is the most sensitive to turbulence modelling. The two equations turbulence model which was able to simulate in the best way the mean flow in the lee side was the RNG, while the SKE was the worst. The RSM produced the flow field closest to the experimental one in the simulation on the grid built over map-A while in the simulation on the grid built over the map-B the best forecasting was given by the RNG while the RSM slightly underestimated the velocity in the lee side.

Depending on the topography the RNG or the RSM seem to behave better, one big issue in the analysed run is that the flow was about to separate or an intermittent bubble of separation was likely present. If unsteady phenomena were present in the chosen run the only way to reproduce accurately the experimental data would be by performing unsteady simulations.

Nevertheless, by observation of the mean flow the best behaving two equation model would look the RNG KE. It would be interesting to analyse an other run, always in neutral conditions, for instance from 180°, possibly when the flow was not prone to separate.

The turbulence results are instead presented in Figure 4.14 by the TKE values collected along line A where the values of the measured TKE are the same of Figure 4.5. The SKE model predicts well the level of turbulence upstream and at the top of the hill while the level of turbulence is under predicted in the lee side of the hill. Again, in the adverse pressure gradient flow, poor matching is observed with experimental data with the grid obtained from map-B producing an higher peak of turbulence, but still much smaller than the measured.

When the same TKE data are compared with the numerical results obtained with different turbulence models in Figure 4.15 and Figure 4.16 the two equations models predicting better the TKE level are the SKE and the realizable k-ε in a more or less equal way, while the RNG k-ε leads to a slightly level of

turbulence. The RSM model produces a slightly underestimated TKE at the top of the hill, like the RNG k-e does, but it's the turbulence model which predicts the highest peak of turbulence at the lee side, still too low compared to the experimental data. In the forecast of the TKE the grid dependency is even much stronger than in the velocity prediction, therefore also for the turbulence plots a much better result is expected if an higher horizontal discretization is considered.

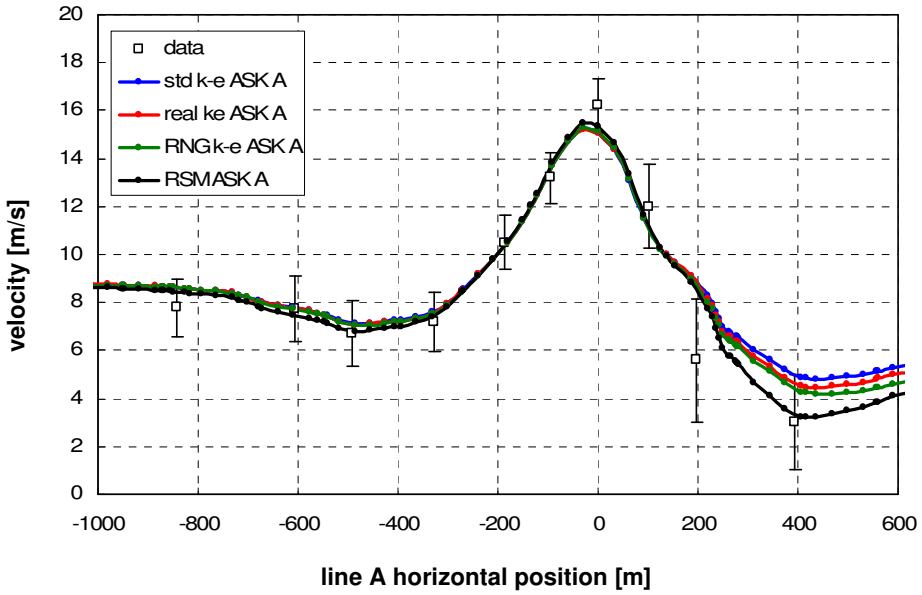

Figure 4.12 – Horizontal velocity along line A (10 m a.g.l.), k-ε derived turbulence models and RSM over map-A.

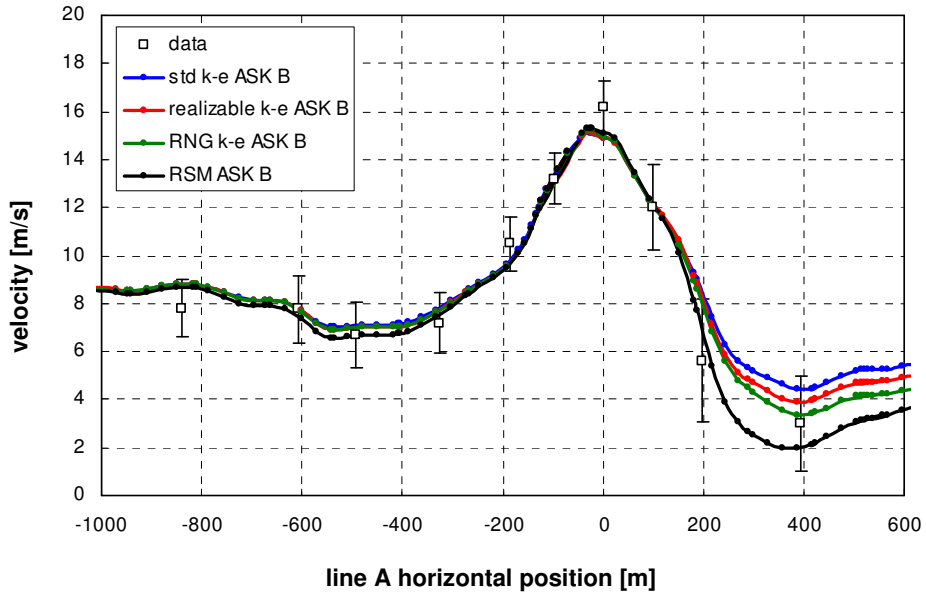

Figure 4.13 – Horizontal velocity along line A (10 m a.g.l.), k-ε derived turbulence models and RSM over map-B.

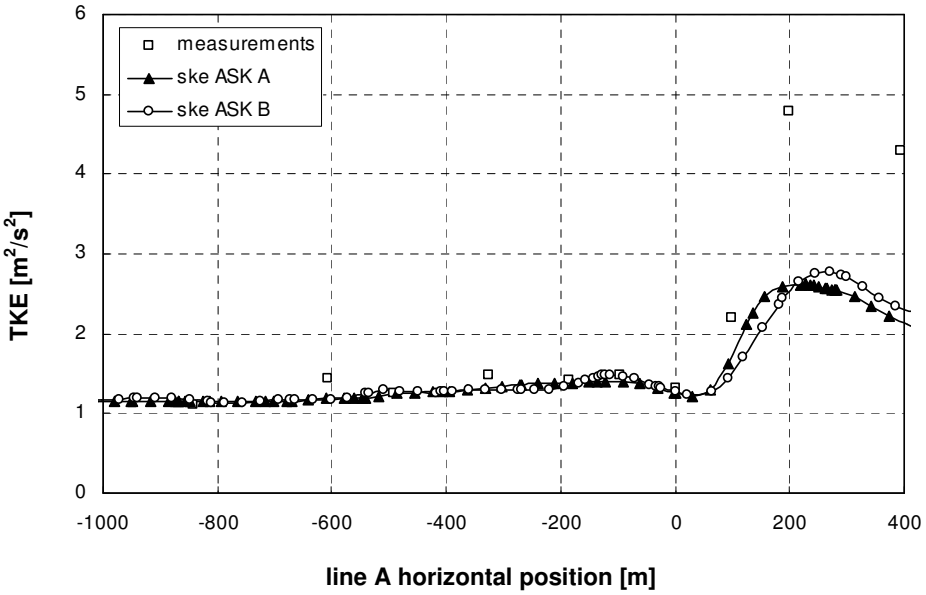

Figure 4.14 – TKE values along line A (10 m a.g.l.), SKE model for both maps

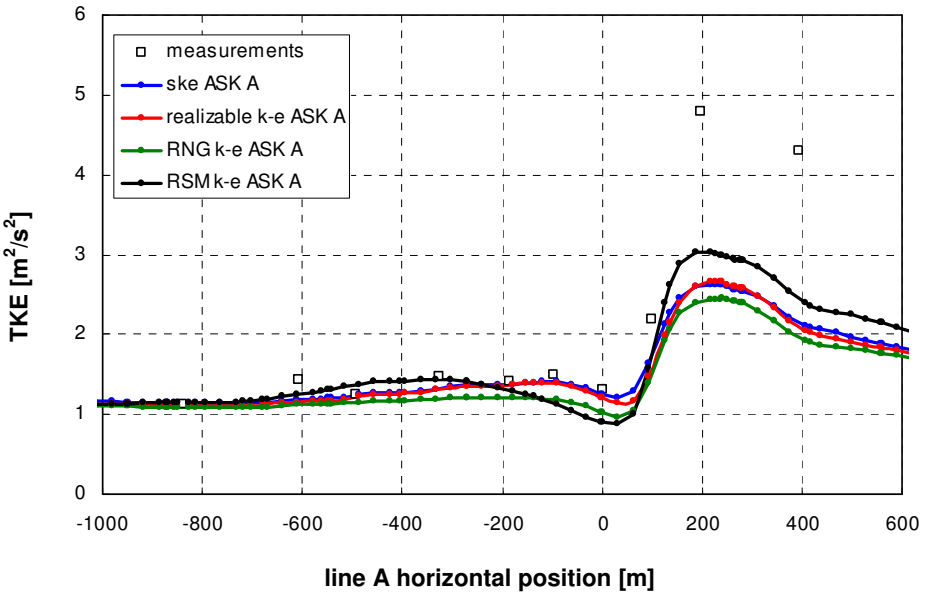

Figure 4.15 – TKE values along line A (10 m a.g.l.), k-ε derived turbulence models and RSM over map-A.

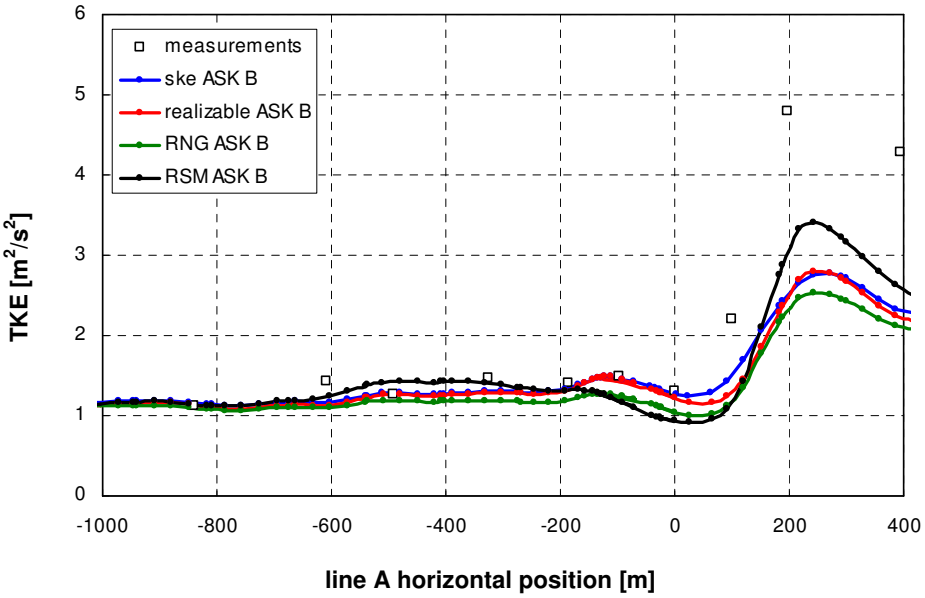

Figure 4.16 – TKE values along line A (10 m a.g.l.), k-ε derived turbulence models and RSM over map-B.

In Figure 4.17 the standard deviations of the velocity vector are plotted along line A, both measured and calculated by the RSM model, while the standard deviations for the horizontal components are generally underestimated, for the vertical component the standard deviation is overestimated, these behaviours are then enhanced in the lee side of the hill at approximately at 200 m downstream of the hill top.

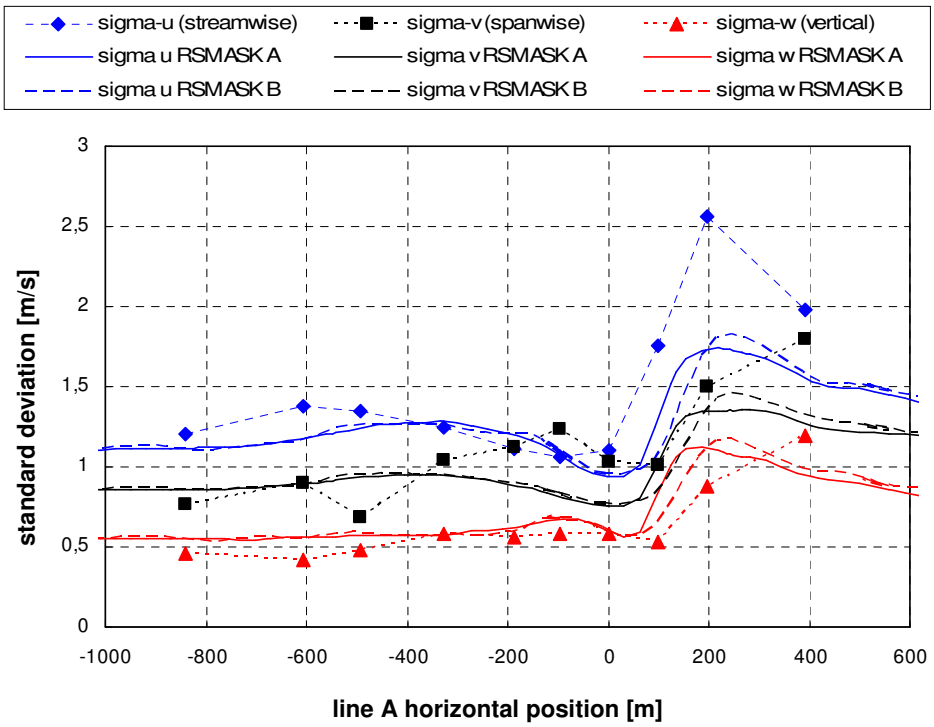

Figure 4.17 – standard deviations of velocity components along line A (10 m a.g.l.), measured and simulated with RSM over map-A and map-B.

4.2.4 Simulations with WindSim

The software WindSim is aimed at calculating the annual energy production of a given wind farm; it firstly generates a structured grid made of hexahedral cells, fitted to a given topography, and then solves the RANS equations by means of the commercial CFD code PHOENICS, with a finite volume approach, in steady state conditions for an uncompressible and isothermal flow.

The continuity and momentum equations are solved with a segregated solver named SIMPLEST which is a modification of the widely used algorithm SIMPLE.

The meshes generated with WindSim are built over a rectangular area with the borders directed eastwards and northwards; horizontally they can be uniformly spaced or with an inner refined region which is usually the area enclosing the wind farm or the anemometric station. The grids can be stretched also along the vertical direction; in this fashion the smallest cells result the adjacent to the terrain while the others expand vertically with increasing altitude.

The inlet conditions are the same used in the Fluent simulations presented in the first part of this chapter: vertical profiles of velocity, TKE and TDR are imposed at the inlet; the outlet is treated by providing a pressure profile while, when the flow is directed in 0°, 90°, 180° and 270° the lateral borders are treated as symmetry planes; a second approach available in the setting of the boundary conditions is given by a nesting procedure, a meso-scale model is performed, the flow field obtained is then used to provide boundary conditions for an inner micro-scale model.

The turbulence model used by default by WindSim to close the RANS equations is the standard k-ε model which can be selected with two different sets of constants that are reported in Table 4.5.The sets of modified constants in Table 4.5 are the same also used in *Castro et al. (2003)* [5] and proposed in *Beljaars et al. (1987)* [3].

Table 4.5 – Constants of the standard k-ε model in WindSim 4.5

	C_μ	$C_{1\varepsilon}$	$C_{2\varepsilon}$	σ_k	σ_ε
Standard	0,09	1,44	1,92	1	1,3
Modified	0,034	1,44	1,92	1	1,85

The case study of Askervein have been also analysed with WindSim in order to test the two sets of constants available and compare the numerical results obtained with the corresponding data obtained with Fluent.

Grids with different resolution were analysed in order to study the grid sensitivity of the results.

The simulations carried out with the code WindSim 4.5 were performed on the digital map-B, covering an area of 6000 m x 6000 m centred on the hill of Askervein.

Three grids has been constructed over the map-B and then employed in the simulations performed with the code WindSim and some geometric features of the computational domain and grids are reported in Table 4.6 and Table 4.7. The horizontal resolution in the inner refined area of the coarsest grid is comparable with the resolution of the meshes employed in the simulations performed with the code Fluent which is 30 m, while grid 1 and 2 are horizontally more refined in the inner region with a horizontal spacing around 20 m.

In the Figure 4.18 it's shown the topography of the hill of Askervein while in Figure 4.19 is visible a top view of the map-B discretized as in Grid 3, measurements points RS, HT, CP and along line A are also shown.

Table 4.6 – horizontal extension of domains an inner refined regions employed in the simulations of the Askervein hill flow with WindSim

Height domain	1000m above highest terrain node		
Easting (x) extension	X_{min} 072688m	X_{max} 078688m	ΔX 6000m
Northing (y) extension	Y_{min} 820456m	Y_{max} 820456m	ΔY 6000m
Refined area			
Easting (x) extension	X_{min} 074488m	X_{max} 076688m	ΔX 2200m
Northing (y) extension	Y_{min} 822256m	Y_{max} 824456m	ΔY 2200m

Table 4.7 – geometric features of the domains and meshes for the performed simulations on Askervein hill with the code WindSim

Number of cells	N_X	N_Y	N_Z	**Total cells**
Grid 1	168	168	34	959 616
Grid 2	168	168	40	1 128 960
Grid 3	119	119	40	566 440

Max resolutions	Δx_{min}	Δy_{min}	Δz_{min}
Grid 1	21,4m	21,4m	2,428m
Grid 2	21,1m	21,2m	0,375m
Grid 2	21,1m	21,2m	0,375m

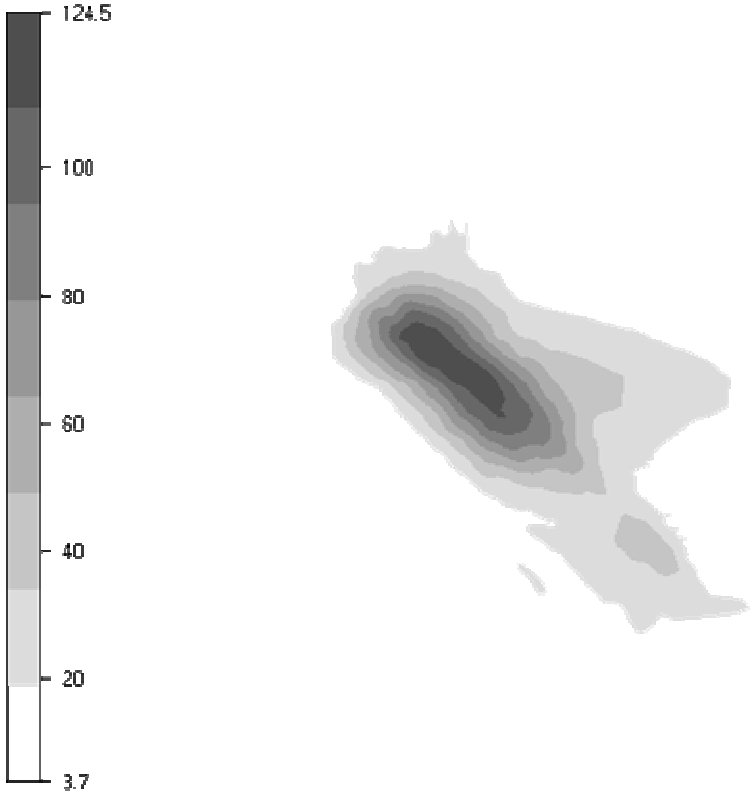

Figure 4.18 – Elevation map of Askervein hill obtained from map-B

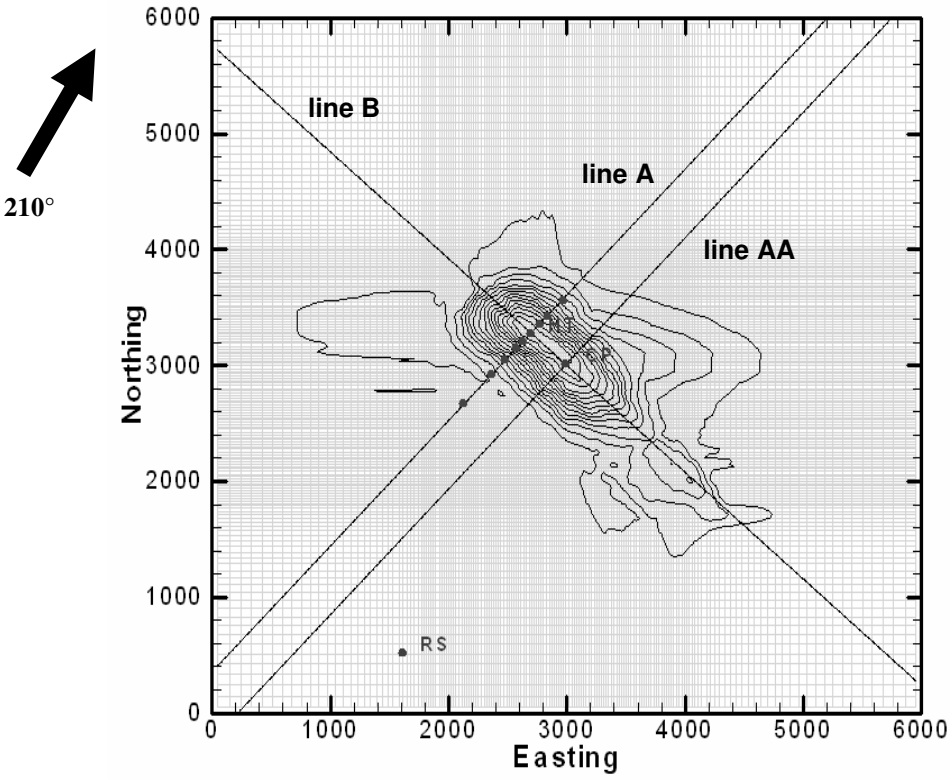

Figure 4.19 – Discretized map-B for the grid 3, points HT, CP, RS and 10 m masts locations along line A. 210° wind direction as in run TU03-B of Taylor and Teunissen (1985) [36]

The standard k-ε turbulence model has been employed to investigate the flow on the hill of Askervein with both the sets of constants reported also in Table 4.5. The friction velocity employed is about 0.634 m/s as calculated by interpolating the experimental data at RS relative to the run TU03-B. In Table 4.8 the simulations whose results will be reported in following paragraphs are summarised, classified by grid, turbulence model, number of iterations.

The chosen direction for the incoming wind is the 210° measured clockwise from north as done for simulations with Fluent, in this way WindSim considers two faces as inlets and two as outlets, this is also an important difference existing between the simulations performed with Fluent and WindSim. The computations performed with WindSim are meant, like the ones carried out

with Fluent, to reproduce the wind field observed during the experimental run TU03-B, MF03-D and TK03 of the report *Taylor and Teunissen (1985)* [36].

Table 4.8 – Set of simulations of Askervein (from map-B) run with WindSim 4.5

Turbulence models	SKE default	SKE mod.
Grid 1	✓ **($u_{\tau 1-2}$)**	✓ **($u_{\tau 1}$)**
Grid 2	✓ **($u_{\tau 2}$)**	✓ **($u_{\tau 2}$)**
Grid 3	✓ **($u_{\tau 1-2}$)**	✓ **($u_{\tau 1-2}$)**

Number of iterations	SKE default	SKE mod.
Grid 1	$5500_{(1)}/3000_{(2)}$	4000
Grid 2	3000	1100
Grid 3	$3000_{(1)}/3000_{(2)}$	$4000_{(1)}/3000_{(2)}$

Friction velocities		
$u_{\tau 1}$	0,422 m/s	u(500m)=10 m/s
$u_{\tau 2}$	0,6336 m/s	u(500m)=15,02266 m/s (TU03-B)

4.2.4.1 Results: mean flow and turbulence

The calculated mean flow-field is compared to the experimental measurements reported in table A1.3 and A1.4 of *Taylor and Teunissen (1985)* [36]. The computed horizontal velocity along the line A is plotted in Figure 4.20 showing that also WindSim underestimates the velocity magnitude at the top of the hill and overestimates at the lee-side, as already observed in the Fluent simulations. The grids 2 and 3 provide basically the same results in terms of velocity and the grid 1 differs from the other two meshes in the lee side of the hill at about 0,5 km from the hill top which is very likely connected to the high level of turbulence predicted. The grid dependency is shown also in Figure 4.21 by means of the TKE predicted along line A, the simulation carried out with the grid 1 was probably close to diverge since the too high value of TKE obtained

at the lee side, the high value of TKE remained restricted in the lee area but the peak of TKE about 10 m^2/s^2 is not verisimilar. The grid 2 predicted a TKE peak higher than the one computed with grid 3, showing the grid dependency of the results; finally the flow field obtained with grid 3 is very similar to the one calculated with Fluent in a similar horizontal resolution showing not many differences between results obtained by the two numerical tools.

Also the effects of the usage of both sets of SKE model's constants, see Table 4.5, have been carried out, the numerical results are presented in the same manner adopted for the grid dependency study, in Figure 4.22 is plotted the horizontal velocity and in Figure 4.23 the TKE both calculated along line-A passing through the hill top. In terms of velocity the usage of the two sets of constants is not so significant, the two curves in Figure 4.22 do not differ that much; the usage of the two sets of constants produce instead different values of TKE which is generally higher for the modified set due to the smaller C_μ, while the predicted peak of TKE is the same in the two cases resulting in a generally smoother turbulence field when applying the modified set of constants.

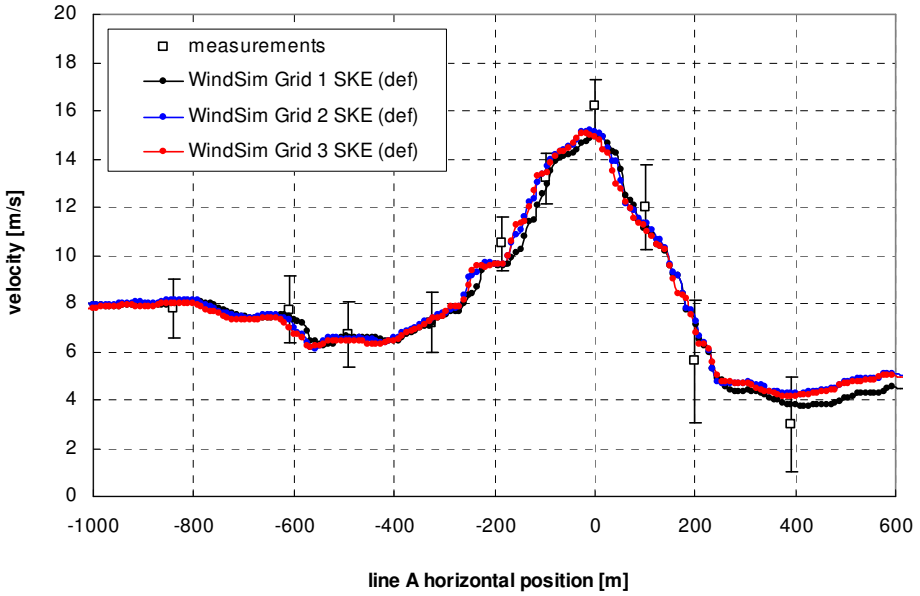

Figure 4.20 – Grid dependency: horizontal velocity along the line A, reproduction of experimental data TU03-B.

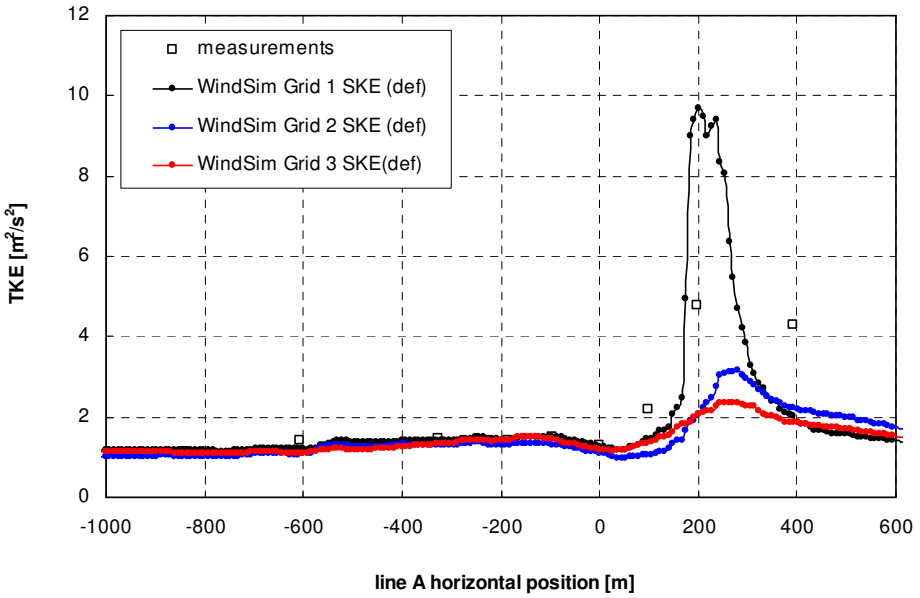

Figure 4.21 – Grid dependency: Turbulence Kinetic Energy (TKE) predicted with WindSim 4.5 and measured (TU03-B) along line A at 10 m a.g.l.

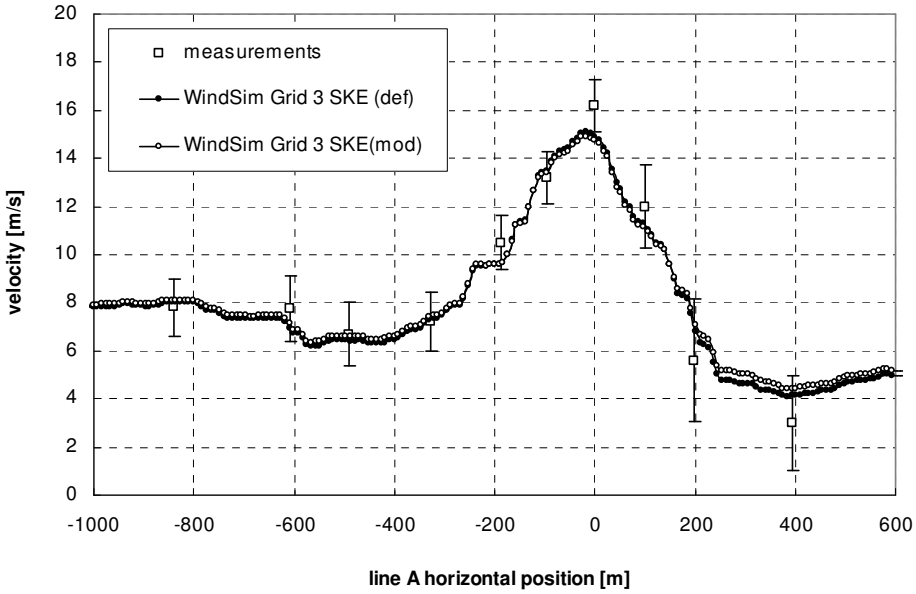

Figure 4.22 – Model's constants dependency: horizontal velocity along the line A, reproduction of experimental data TU03-B.

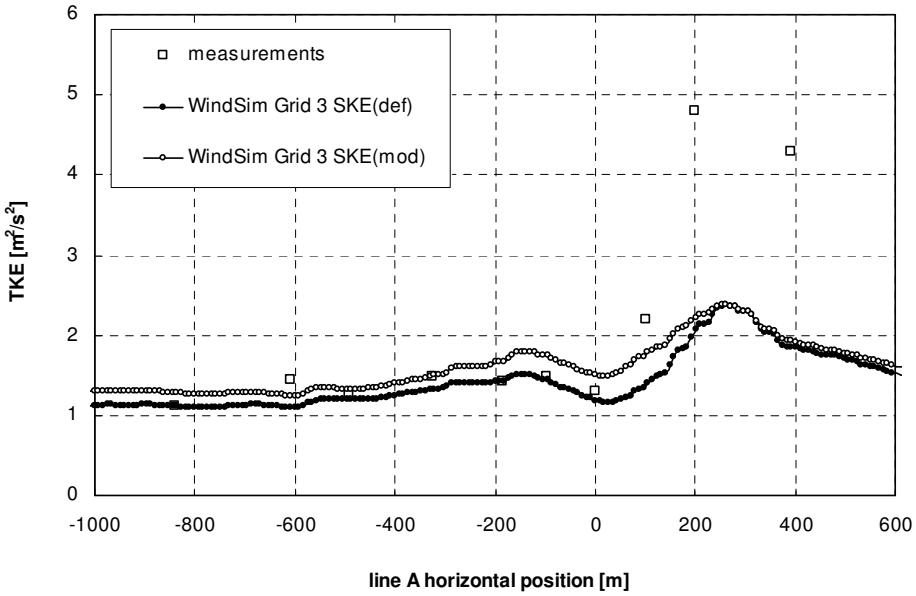

Figure 4.23 – Model's constants dependency: Turbulence Kinetic Energy (TKE) predicted with WindSim 4.5 and measured (TU03-B) along line A at 10 m a.g.l.

Chapter 5 SIMULATIONS 3D DES/LES OVER FLAT TERRAINS*

5.1 INTRODUCTION

Present literature and in-house experience pointed out that RANS approach is insufficient to provide a satisfactory simulation of flows bounding complex terrains' features or architectural structures, leading to explore the application of more precise turbulence solving methodologies such as Large Eddy Simulation (LES) and hybrid methods URANS/LES such as the Detached Eddy Simulation (DES). Further CFD techniques are obtained once LES or hybrid URANS/LES are coupled with the use of wall functions to model the flow in the wall adjacent cells, in this case the Wall Modelled LES (WMLES) is used rather than pure LES. In this way turbulent flows with Reynolds numbers up to 10^9 are affordable. Moreover, the turbulence plays the main rule to determine fluxes of momentum, energy and moisture within the atmosphere. An accurate prediction of the turbulence within the ABL is therefore necessary and an application of eddies solving methodologies like LES and DES is nowadays simulating the research since the improved capabilities of the modern computers and the lack, up to now, to predict in a correct way the logarithmic wind profile in the surface layer by LES methods.

In the present chapter will be described a series of DES and WMLES aimed at evaluating the capabilities of the commercial code Fluent 6.2 in reproducing a neutral ABL with eddy solving methodologies.

Since the scope of the presented simulations was to model a neutral stratified flow, only the continuity and momentum equations have been solved; a grid's resolution study have been performed to determine the proper discretization for all the different classes of terrain roughness.

* The present chapter is a rearranged version of the DC project's thesis "Investigation of the Atmospheric Boundary Layer applying Large Eddy Simulation" carried out at the von Karman Institute during the academic year 2005-06.

Boundary conditions for eddies solving methods should have some characteristics, for instance, the vertical planes parallel to the flow cannot be symmetry planes as done in RANS simulations, since symmetry planes kill the turbulent fluctuations and the formation of the eddies themselves; periodic conditions are therefore used in the span-wise direction. When the ABL to be studied is a fully developed flow over a flat terrain periodic conditions stream-wise are again successfully applied.

Inlet conditions with imposed velocity and turbulence are not taken into account in the present PhD thesis but they deserve to be considered in alternative to stream-wise periodic conditions especially when the ABL considered flows not anymore over a flat terrain but over topographic features. In this way the size of the domain itself can be kept not too wider than the region of interest. For a neutral ABL such those studied and presented in this chapter, the upper boundary can be imposed as a symmetry plane while wall-functions are still used for the terrain, as done in the RANS simulations.

5.2 STUDY OF THE ABL WITH LES TECHNIQUES

In the last two decades several studies have dealt with the reproduction of the ABL with eddies solving techniques, both LES and hybrid RANS/LES methods (DES). LES of neutral stratified boundary layers have been presented by Mason and Thomson (1987) [24] using a standard Smagorinsky SGS model in the simulation of an Ekman layer. The same authors proposed in 1992 [25] the use of the Smagorinsky model coupled with a back-scattering technique to cure the failure of the simulations to well reproduce the logarithmic law, equation (1.3). In fact, as also mentioned by Mason and Thompson [25], when the neutral ABL is simulated with the original Smagorinsky-Lilly model, an overshoot in the velocity is typically obtained with values of normalised wind shear ϕ_m reaching a maximum about 2.

In recent years two approaches have been followed in order to improve the simulations: one is the refinement of the grids in order to set a proper filter

width, while the second one is the usage of improved and generally more advanced SGS models compared to the standard Smagorinsky-Lilly.

Sullivan P.P. *et al.* (1994) [34] proposed a two-part eddy viscosity model where the contribution of mean and fluctuating eddy-viscosities are introduced and their effects are balanced by means of an "isotropy factor".

Among most recent works dealing with LES simulations of ABL it's worthy to mention the Ph.D. thesis of F.T. Chow (2004) [7] where a dynamic reconstruction model is applied to reconstruct the resolvable sub-filter-scale (RSFS) stresses together with the dynamic eddy-viscosity model by Wong and Lilly (1994) [42] for the sub-grid-scale stresses (SGS). Furthermore, an example of DES applied to the planetary boundary layer is given by the multi-planet EPIC General Circulation model proposed by Dowling T.E. and LeBeau R.P..

5.3 METHODOLOGY FOR THE DES/LES SIMULATIONS OF THE ABL

The flow field computed by both DES and LES methods need to be started from a RANS steady solution properly perturbed in order to make develop the turbulence more easily. Few pass-through times has to be waited for before gather statistics, that should be done when statistically steady conditions are reached.

5.3.1 Initial steady simulations

All the unsteady simulations, both DES and LES, 2D and 3D cases are started from a converged solution of a RANS simulation of the ABL using the SKE model for the turbulence closure.

The grids employed were all of structured type with uniform horizontal spacing and ranging from 20 m to 60 m of size. For the vertical discretization of the domain the prescription to assign the height of the wall adjacent cell h higher than twice RH (Roughness Height) it has been followed, but the more accurate results in term of predicted wall-shear stress are obtained with the

value of h only slightly higher than 2 RH, the rest of the vertical spacings are assigned in order to obtain a successive ratio about 1,1; the meaning of the parameter RH appearing in the wall function for rough surfaces is explained in the Fluent User's Guide [10].

The initial RANS simulations are run with the SKE model, the air is treated as uncompressible and dry; about the operating conditions the operating pressure is set at 1 atm at the ground level, the gravitational acceleration is enabled, while the operating density has been set to zero.

As regards the boundary conditions employed, the upper face of the domain has been set as symmetry, while periodic boundaries have been used, only streamwise in 2D and both spanwise and streamwise in 3D. The mass flow has been assigned, usually calculated by assuming that a log-law is valid in the whole domain. The terrain has been treated with a wall boundary condition, using wall functions for rough surfaces, usually with RC (Roughness Constant) one and RH calculated by the equation:

$$\mathrm{RH} \approx \frac{z_0 \, E}{\mathrm{RC}}, \qquad \textbf{(5.1)}$$

Which is obtained by the (2.33) with C_S and K_S respectively equal to RC and RH. The equation (5.1) comes from the comparison of (1.3) and the wall-function modified for rough surfaces as it is described in the Fluent user's manual [10].

Even if the maximum value accepted by Fluent for the RC parameter is one (value accepted 0÷1) thorough the graphical user interface, it's also possible to assign a value of RC higher than one, by reading a profile file for the lower boundary where values of RC are specified for each cell of the terrain. For instance RC can be set to E and RH to z_0 which also allows to draw a finer grid close to the wall and to obtain a more precise wall shear stress forecast.

The described roughness settings for a finer grid with the parameter RC higher than unity have been set successfully for RANS SKE simulations and

there is hope that their use will provide some improvements also in LES and DES simulations.

As regards the discretization methods adopted, the default schemes have been left active but the pressure discretization scheme is turned to PRESTO! (PREssure STaggered Option) which simulates a staggered grid helping the convergence process. The upper limit of the ratio eddy viscosity to laminar viscosity is increased in such a way that the code won't prevent this ratio to grow, in fact the eddy-viscosity for an ABL is naturally very high so there is no reason to limit its value.

Finally the RANS simulation is run until reaching a complete convergence, with the residual at minimum possible value, for a grid counting 125000 cells this condition is generally reached in 6000 iterations.

Once the solution of the RANS simulation reaches the convergence, the command **`solve>initialize>init-instantaneous-vel`** perturbs the flow field calculated, the velocity field is in this way prepared to start up the LES or the DES simulation. The initialization of the flow field superimposes over the RANS final solution a synthetic turbulence. In this way it's easier to make develop a "natural" turbulence, i.e. ruled by the solved equations. In some cases a turbulence will be never obtained without a initialization command since turbulence needs instabilities and some perturbations in the flow field to born and grow. The kind of instability present in a fully developed boundary layer needs a perturbation of a certain amplitude in order to obtain turbulence; this is not the case of other instabilities for instance of turbulent wakes, jets and mixing layers where all scales perturbations, also very small and hence always present, are amplified and finally lead to turbulence.

Unfortunately, in Fluent user's guide [10] there is no further description about the initialization of the instantaneous flow field even thought it's very likely that the same command is used in producing a synthetic turbulence for the perturbed inlet conditions. In this case the perturbation of the flow field is obtained by the free-divergence random-flow-generation function proposed by Kraichnan (1970) [20] and modified by Smirnov et al. (2001) [30], this

command is based on the summation of a finite number of Fourier harmonics (100 in the code Fluent) in order to construct a synthetic turbulence spectrum.

In the code user's guide [10] it's not mentioned if the initialization command is available only for some turbulence models. Nevertheless it has been noted during the performed tests that the initialization of the instantaneous velocities is not valid when the SA turbulence model is activated, this is the reason why the RANS simulations performed before the initialization of the flow field are done with the standard k-ε model rather than the SA model, which is the most natural choice when the scope is to switch to the SA based DES.

In order to have a feeling of the effect of the initialization command described on the flow field it can be seen from Figure 5.1 and Figure 5.2 how the command produces a perturbation on the original velocity field (velocity profiles of Figure 5.1) obtaining the velocity profiles like the ones shown on the lower part of Figure 5.1; in Figure 5.2 can instead be seen how the turbulence kinetic energy is not directly influenced by the perturbation command.

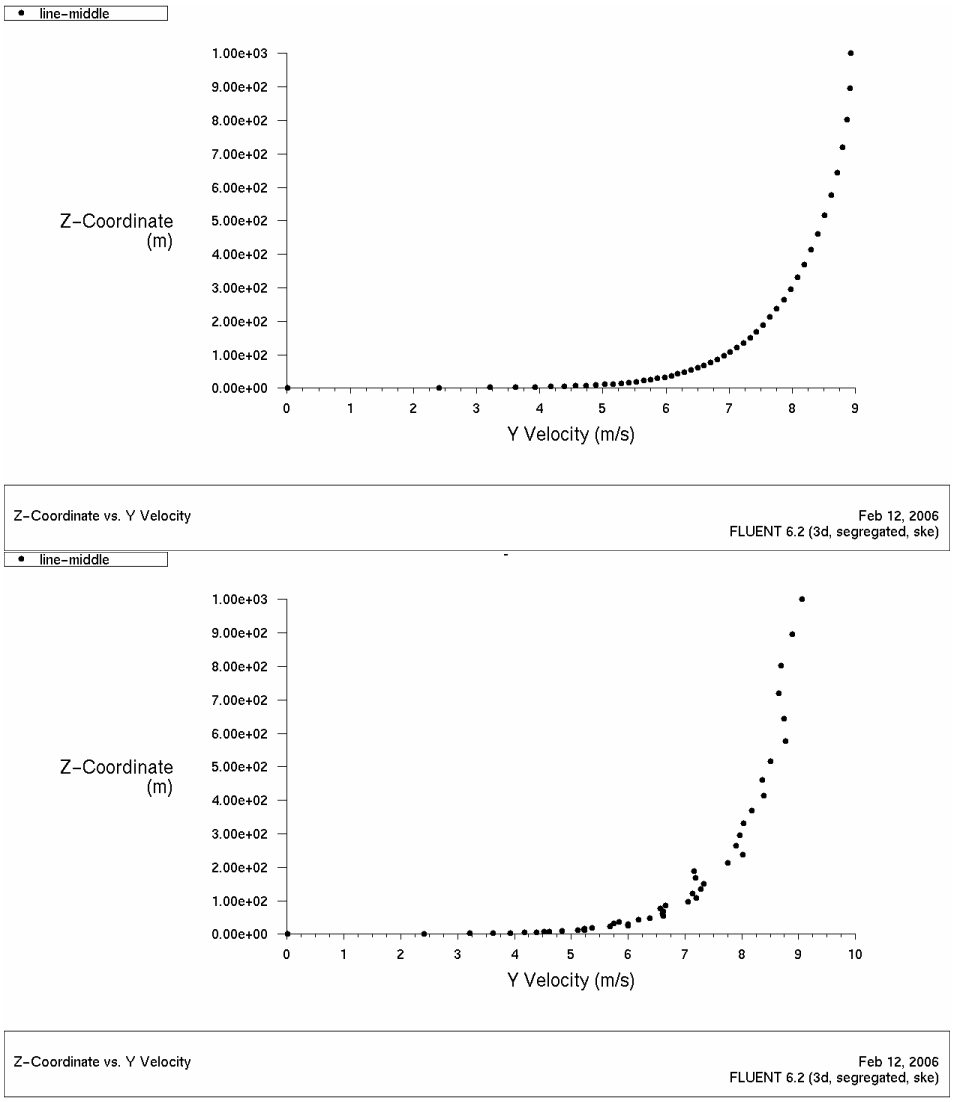

Figure 5.1 – Example of vertical profiles stream-wise component of velocity for a converged RANS SKE simulation (above) and the same value after initialization command (below).

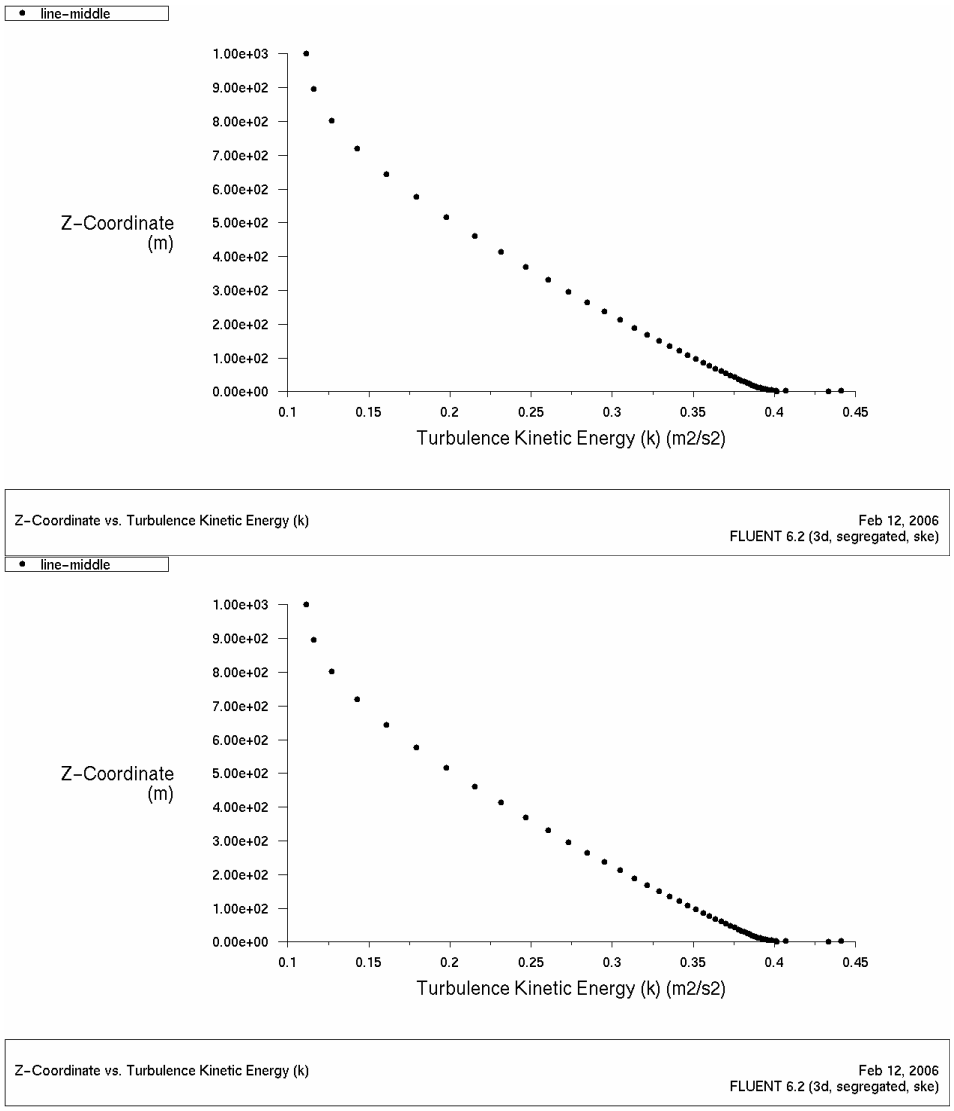

Figure 5.2 – Examples of TKE vertical profiles for a converged RANS SKE (above) and the same values after initialization (below).

5.3.2 Turbulence modeling

The study presented in this chapter dealt with the LES/DES simulations of a neutral ABL over a flat terrain using the commercial code Fluent 6.2; hence only the continuity and momentum equations have been employed, paying attention to determine the sensitivity of the model to different parameters such

as grid resolution, roughness parameters and turbulence model's parameters (SGS).

Since the LES option in Fluent 6.2 can not operate with wall-functions adapted for rough walls the choice of the turbulence treatment has been left in the first part of the study to an hybrid URANS/LES methodology named DES (Detached Eddy Simulation) based on a modification of the Spalart-Allmaras model, while in a second moment of the study an home-made Smagorinsky-Lilly model has been plugged in the code in order to use it coupled with the wall-functions modified for the roughness.

In the eddies solving methods LES only the big-eddies are solved directly (resolved scale) while the small-scale eddies effects are modelled with turbulence models named sub-grid-scale (SGS) models, or more correctly the sub-filter-scale (SFS).

A peculiarity of eddies solving methodologies is that the flows have to be modelled always in unsteady simulations; also a 2D approach is theoretically wrong since eddies are correctly developed only in tri-dimensional space. Nevertheless 2D LES can be carried out and it has been successfully applied especially in some cases of external aerodynamics of bluff bodies.

5.3.3 The new LES-UDF implemented in Fluent

The code Fluent 6.2 offers four methodologies to model the SGS eddy viscosity $\mu_{t\text{-}SGS}$, four SGS models:

- the Smagorinsky-Lilly (SL) model
- the dynamic SL model
- the Wall-Adapting Local Eddy-Viscosity (WALE) model
- the dynamic kinetic energy model

All the listed models are not available coupled with the wall-functions for rough walls while the DES option does. Therefore the need in the present

project for DES turbulence modeling or the implementation of a new SGS turbulence model to be used coupled with the wall-functions.

In the standard Smagorinsky-Lilly SFS model, which has been implemented in a new UDF and used for rough surfaces in the present project, the $\mu_{t\text{-}sgs}$ is modelled by:

$$\nu_{t-sgs} = (C_S \Delta)^2 |\overline{S}| \quad \textbf{(5.2)}$$

Being C_S the Smagorinsky constant, Δ the filter width $(= \text{cell} - \text{volume}^{1/3})$ and $|\overline{S}|$ the magnitude of the resolved scale rate of strain tensor

$$|\overline{S}| = (2 S_{ij} S_{ij})^{1/2} \quad \textbf{(5.3)}$$

5.3.4 DES settings tested

The SA based DES model is implemented in Fluent 6.2 as proposed by Shur *et al.* (1999) [28], two further modifications of the model are available:

1. the possibility to substitute the length scale *d* only in the destruction term
2. and to compute the filter size Δ from the volume of the cell in equation (5.5) rather than on the maximum dimension (5.4).

$$\Delta = \max(\Delta x, \Delta y, \Delta z) \quad \textbf{(5.4)}$$

$$\Delta = \sqrt[3]{\text{cell} - \text{volume}} \quad \textbf{(5.5)}$$

The possibility to choose two values of filter width and the replacement of the new length scale (2.29) in both the production and destruction term or only in the destruction term lead to four possible settings of the DES model which are named and summarized in the Table 5.1.

It's worthy to remember that the choices shown in Table 5.1 are available in Fluent only through the text user interface.

The four possible DES models have been tested in 2D domains both for smooth and rough walls, the model more similar to a LES with a Smagorinsky-Lilly model has been finally chosen for the 3D simulations.

Table 5.1 – classification of the four DES options in Fluent 6.2.

	$\Delta = \max(\Delta x, \Delta y, \Delta z)$	$\Delta = \sqrt[3]{\text{cell} - \text{volume}}$
$\tilde{d} = \min(d, C_{DES}\,\Delta)$ replaced in all the terms (production + destruction)	**DES1**	**DES2**
$\tilde{d} = \min(d, C_{DES}\,\Delta)$ replaced only in the destruction term	**DES3**	**DES4**

Furthermore, if the variable S is computed with equation (2.8) and changing the value of some constants (C_{prod} and C_{w3})of the model further possible settings are available; some of the possible settings have been tested on 2D and 3D boundary layers, the settings tested are:

- Case a: S based on vorticity;
- Case b: S based on vorticity/strain (equation (2.10)), $C_{prod} = 2$, $C_{w3} = 2$;
- Case c: S based on vorticity/strain (equation (2.10)), $C_{prod} = 1$, $C_{w3} = 2$;
- Case d: S based on vorticity/strain (equation (2.10)), $C_{prod} = 1$, $C_{w3} = 0$

Where all the other constants are left with the default values. The reason why the C_{prod} is set to 1 is to make $S \equiv |\bar{S}|$ when $|\bar{\Omega}| > |\bar{S}|$ while the constant C_{w3} is set to 0 to make f_w in the destruction term equal to 1.

Considering the transport equation for the modified eddy viscosity adopted in the SA model, equation (2.8), in equilibrium conditions (production term = destruction term) the following relation holds for the settings DES4d (which means DES4 of Table 5.1 and case d of the previous list):

$$\tilde{\nu}_t = \frac{C_{b1}}{C_w}\left(C_{des}\,\Delta\right)^2 \tilde{S} \qquad \textbf{(5.6)}$$

Comparing the equation (5.6) to the (5.2) and considering that far from the wall $\tilde{\nu}_t \approx \nu_t$ and $\tilde{S} \approx S$ it turns out that

$$C_S{}^2 \approx \frac{C_{b1}}{C_w} C_{des}{}^2 \qquad \textbf{(5.7)}$$

In order to make the Smagorinsky LES and the SA based DES models predict the same order of magnitude of SGS turbulent viscosity the equation (5.7) has to be respected.

5.4 2D TESTS

Before dealing with the description of the 3D simulations performed of a neutral ABL, that will be presented in the paragraphs 5.5 and 5.6, the preliminary tests 2D are going to be described in the present one. The DES and LES tests 2D do not pretend to solve correctly the ABL since eddies are 3D structures and only 3D simulations can solve them. The 2D simulations are meant to test quickly some features and parameters of the models employed even if a real response about the quality of a model can only come from the tri-dimensional simulations. In 2D LES/DES, as has been observed , turbulence 2D is hard to form especially when no important obstructions to the flow like bluff bodies are present. For instance in the 2D studied cases of flat terrains that are going to be presented in this chapter the perturbations superimposed with the initialization command did not develop into turbulence.

All the 2D tests have been performed on a simple geometry, a rectangle 6 km long and 1 km high representing a flat terrain. The boundary conditions

employed are translational periodic for the inlet/outlet, wall functions for the ground and symmetry for the upper boundary.

The grid employed is uniform horizontally while a stretching has been prescribed for the vertical discretization, the minimum height of the cell is named h and it's the height of the wall adjacent cell; in all the grids drawn the successive ratio has been kept around 1,1.

The methodology followed for the simulations is the one described in the previous paragraph 5.3. Several tests have been performed over smooth walls for DES, LES and LES with a user defined function implementing a Smagorinsky model (from this point named simply LES-UDF), and, over rough walls, for DES and LES-UDF.

While the 2D simulations over smooth terrains are meant more to compare the LES option of Fluent and LES-UDF to the several tried settings of the DES module, the tests over rough surfaces allowed comparisons of DES settings only to LES-UDF.

5.4.1 2D boundary layers on smooth walls

2D simulations have been run over a smooth flat terrain always using a wall function to model the ground. With this series of simulations it was possible to:

a) compare LES and DES
b) make a study of sensitivity to the parameter C_{DES}
c) make comparisons between different settings of the DES model

The 2D simulations are aimed at reproducing a fully developed boundary layer by applying a translational boundary condition. The numerical results are presented by vertical profiles of velocity, presented in wall units $u^+ = u/u_\tau$ and $y^+ = y\, u_\tau/\nu$ since the flow is over a smooth surface and it is therefore possible to compare the results with the universal logarithmic law of a turbulent boundary layer.

5.4.1.1 2D boundary layers on smooth walls: comparing LES against DES

Two vertical profiles of normalized velocity are shown in Figure 5.3 in wall units, one obtained with a DES and the other with LES with a Smagorinsky-Lilly SGS model and the position of the switching interface is shown with a dashed line; in the RANS region of the DES the universal logarithmic law is predicted correctly while above the RANS region the profile deviates from the log-law, this is due to the fact that in 2D simulations no turbulent structures at all has been developed, so the only eddy-viscosity observed is the one produced by the SGS model. From the same Figure 5.3 it can be seen that the LES model of Fluent acts effectively as an other DES model in the sense that there is a region unsteady RANS, where in fact a mixing length model is applied and at an interface the model switches to pure LES according to equation (2.29).

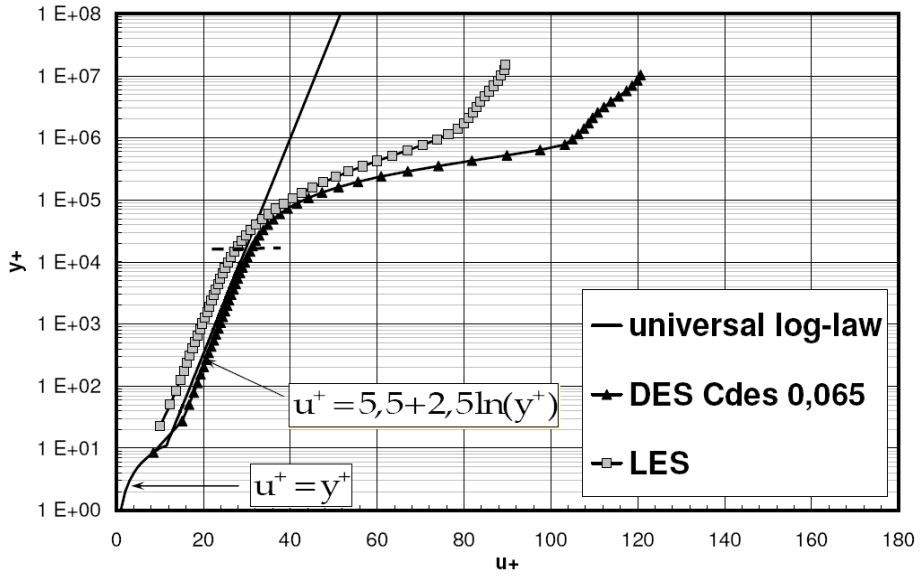

Figure 5.3 – Velocity profiles (u^+, y^+) for DES 2D (C_{DES} 0,065) and LES 2D (C_S 0,1) of flat terrain. Dashed line is the position of the interface RANS/LES for the DES model.

5.4.1.2 2D DES boundary layers on smooth walls: C_{DES} sensitivity

The constant C_{DES} influences directly the position of the interface URANS/LES, as it's shown in Figure 5.4; in the DES model the interface is located at the wall-distance $C_{DES}\,\Delta$, moreover the constant C_{DES} affects the magnitude of the SGS turbulent viscosity exactly like the Smagorinsky constant C_S (see the procedure followed to obtain equation (5.7) and Guénot and Aupoix (2003) [16]).

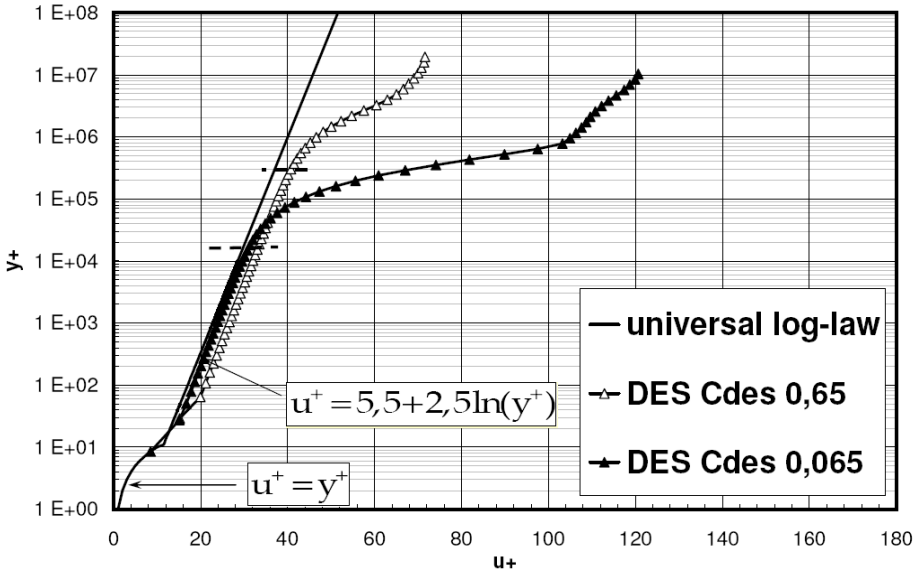

Figure 5.4 – Velocity profiles (u^+, y^+) for DES 2D (C_{DES} 0,065 and C_{DES} 0,65). Dashed lines are the positions of the interfaces RANS/LES.

Lilly derived a value of 0.17 for the Smagorinsky constant C_S for homogeneous isotropic turbulence in the inertial sub-range; according to the equation (5.7) a value of C_{DES} 0.827 is obtained; these values of constants are generally accepted to be too dissipative and smaller values of C_S are therefore used. Since the constant C_{DES} is directly connected to the SGS eddy viscosity and its value cannot change too much from the default value 0.65, the position of the interface, which is placed at $C_{DES}\,\Delta$ from the wall, is correctly controlled only by a proper refinement of the grid in the wall adjacent region since the

filter width Δ is computed from the cell's geometric characteristics by the (5.4) or the (5.5).

5.4.1.3 2D boundary layers on smooth walls: DES settings

Four different settings have been tested on smooth surfaces, numbered from DES1 to DES4 according to Table 5.1. All the cases produced normalised velocity profiles departing from the log law from the interface URANS/LES towards higher y^+ (LES region) as can be observed from Figure 5.5.

The filter width for cases 1 and 3 is computed by the max cell dimension while for cases 2 and 4 Δ is computed by the 1/3 power of the cell-volume; in fact for the cases shown in Figure 5.5 the constant C_{DES} has not been modified and the position of the interface clearly changes with the filter width.

When comparing the cases shown in Figure 5.5 the higher wall shear is obtained for cases 3 and 4 where the modification of the distance in the SA model is applied only in the destruction term which leads also to make $\tilde{S}$ closer to S, and therefore the model closer to a Smagorinsky model.

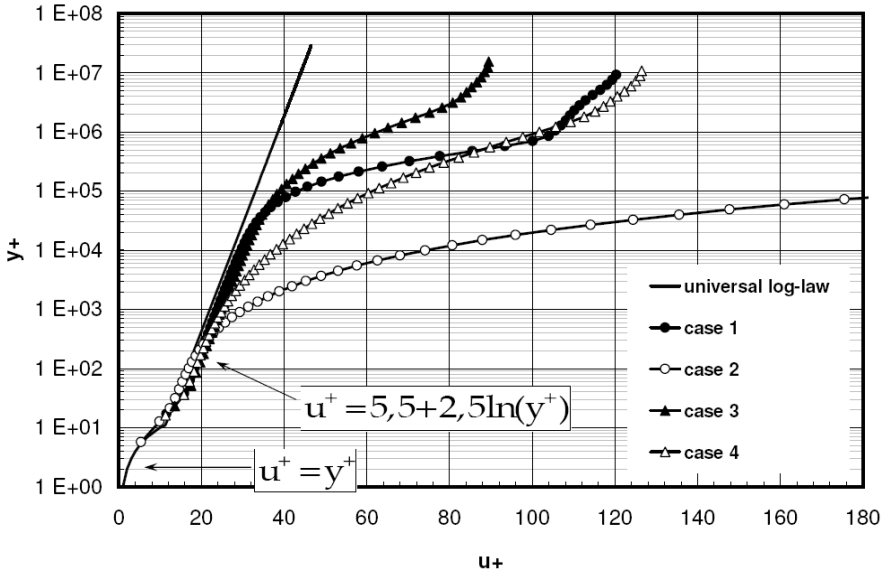

Figure 5.5 – Normalized velocity profiles in wall-coordinates DES 2D (smooth), cases 1, 2, 3 and 4 of Table 5.1.

Since the case 4 is the more similar to a Smagorinsky model it has been chosen to be used for the 3D simulations. There is a good experience in the usage of the Smagorinsky model, even if it's known that eddy-viscosity SGS models like Smagorinsky fails for instance in predicting the log-law expected from the similarity theory.

To make the case 4 even more similar to the Smagorinsky model other three settings have been tried, named 4b, 4c and 4d already listed in the paragraph 5.3.4. With the configuration 4d S is computed only from the strain rate tensor in the region where $|\bar{\Omega}| > |\bar{S}|$ while in the other configurations 4a, 4b and 4c S is computed from a linear combination of $|\bar{\Omega}|$ and $|\bar{S}|$.

Velocity profiles for the further settings of the case 4 are shown in Figure 5.6 in wall-coordinates. It can be seen that the velocity profile for the case 4d is quite different from the ones obtained with the other settings. The main task of this series of tests was to find a set of parameters for the SA based DES which make the hybrid model the closest possible to a Smagorinsky model, therefore further comparisons of DES 4d with LES and LES-UDF will be presented.

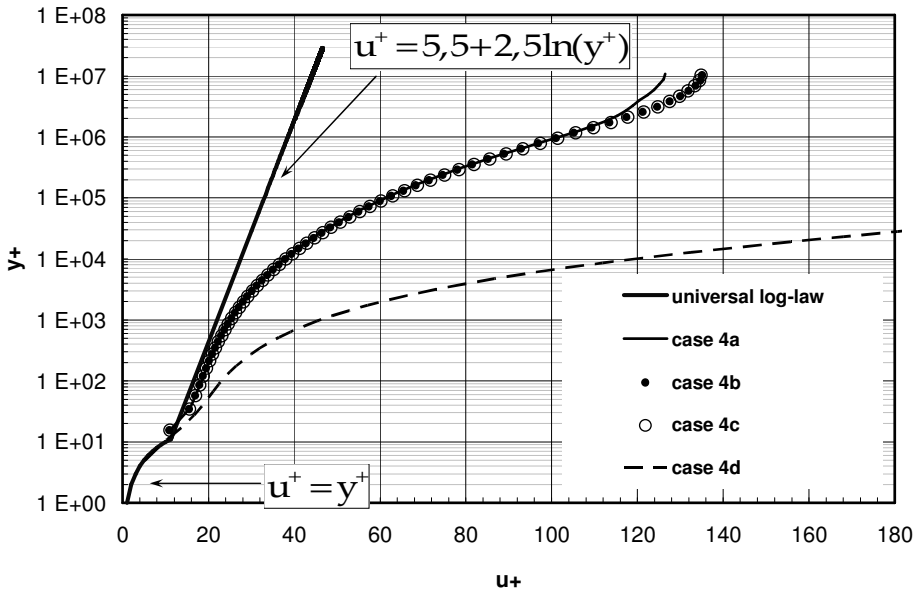

Figure 5.6 – Normalized velocity profiles for the four further settings tried for the case DES 4.

In the following Figure 5.7, Figure 5.8 and Figure 5.9 it's shown as with the DES 4d, LES and LES-UDF similar results are obtained in terms of velocity profiles and eddy-viscosity profiles.

Several tests have been performed on 2D domains and smooth walls, the main conclusions coming from this series of settings is that the DES 4d, LES and LES-UDF are almost equivalent.

Observing the eddy-viscosity profiles of Figure 5.9 it can be noticed how in the LES and DES cases the eddy viscosity decreases to zero closer to the wall, while in the LES-UDF case it approaches a value that is around 0,0002 Pa s, a value that is roughly ten times the molecular viscosity.

This defect is indeed cured in the LES in Fluent by defining a mixing length given by

$$L_S = \min\left(\kappa d, C_S V^{1/3}\right) \qquad \textbf{(5.8)}$$

and the SGS eddy-viscosity is computed by

$$\mu_{t-sgs} = \rho L_S^2 \left|\overline{S}\right|$$

In this way also the LES model acts in hybrid way, with a mixing length model between the wall and the interface and in LES model in the core of the flow therefore, now the interface results placed at $C_S\ \Delta$ from the wall. Depending on the aspect ratio of the wall-adjacent cells the model can act as LES in the all cells or not even without the correction in (5.8), this could be the case of rough walls where not an extreme vertical refinement is required at the wall and more "cubic" wall-adjacent cells are used.

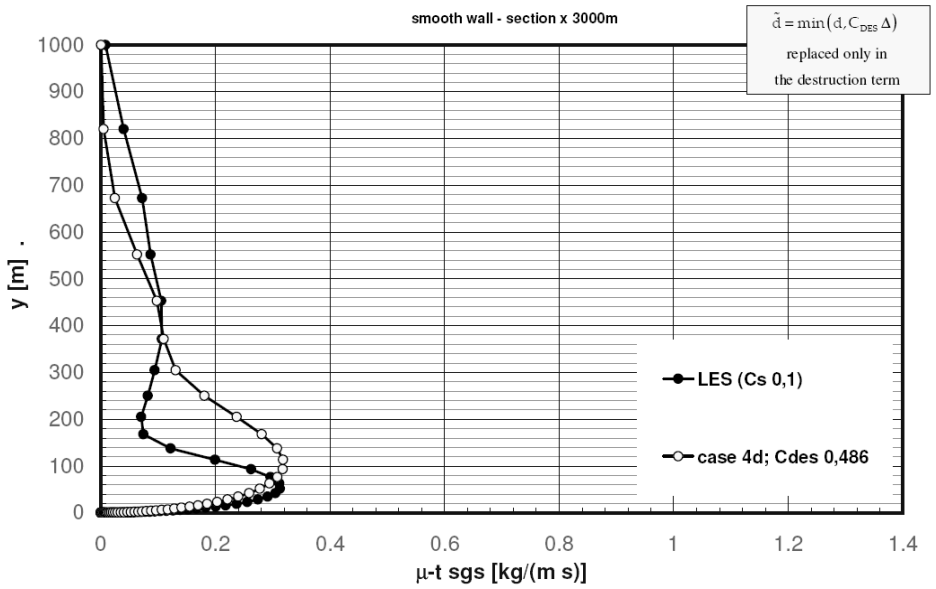

Figure 5.7 – Vertical profiles of turbulent SGS viscosity, comparison of LES (default Smagorinsky of Fluent) and DES with settings 4d.

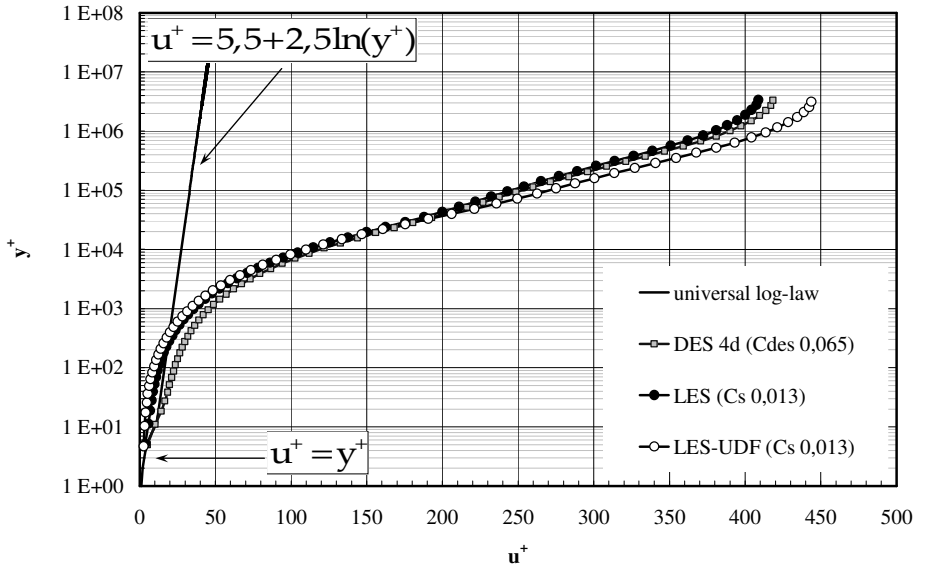

Figure 5.8 – Normalized velocity profiles (in wall-coordinates), DES 4d, LES and LES-UDF cases.

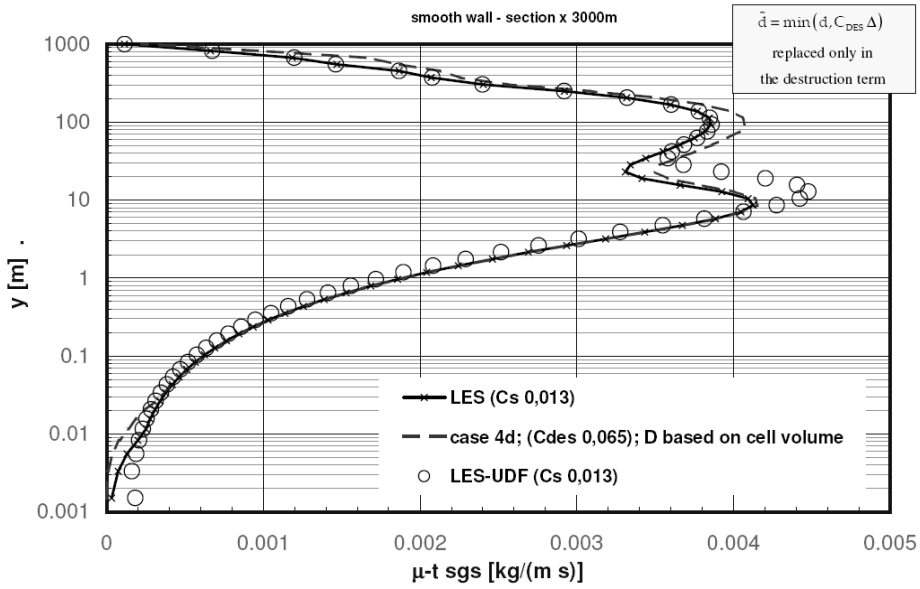

Figure 5.9 – Vertical profiles of SGS eddy viscosity, comparisons of LES (default Fluent), LES-UDF and DES (case 4d).

5.4.2 2D boundary layers on rough walls

The 2D simulations on smooth walls have been mainly done in order to compare DES settings with LES and LES with LES-UDF. For the rough walls the LES is not available and a confirm of the similarity of DES 4d and LES-UDF is here shown.

In the present work three values of roughness for terrains have been analyzed, they are summarized in Table 5.2 with indicated RH and RC, the input parameters of the code for the roughness and h standing for the height of the wall-adjacent cell.

Table 5.2 – Meshes used for the rough walls 2D tests.

class	z_0 [m]	used z_0 [m]	RH [m]		RC (0÷1)	h [m]
			First	Tuned		
IV	0,01÷0,04	0,03	0,2943	0,25	1	0,6
VI	0,1 ÷ 1	0,16	1,567	1,17	1	3,2
		0,5	4,896	3,39	1	10

The values of roughness chosen are not going to be presented for the 2D simulations, while further results are presented in the following paragraphs about 3D simulations. As regards the 2D simulations presented in the next paragraph it will be shown the equivalence achieved between DES 4d and LES-UDF when dealing with rough terrains.

5.4.2.1 LES-UDF and DES4d on rough walls

Comparison of velocity profiles and SGS viscosity profile are shown for the DES 4d case and the LES-UDF with the constant Cs and C_{DES} properly set, Figure 5.10 and Figure 5.11. The two models give very similar results and it's therefore demonstrated that in equilibrium conditions the DES 4d behaves very closely to the LES with Smagorinsky model. Due to the relative good confidence in the Smagorinsky model it has been decided to run the DES 4d and the LES-UDF for the 3D simulations.

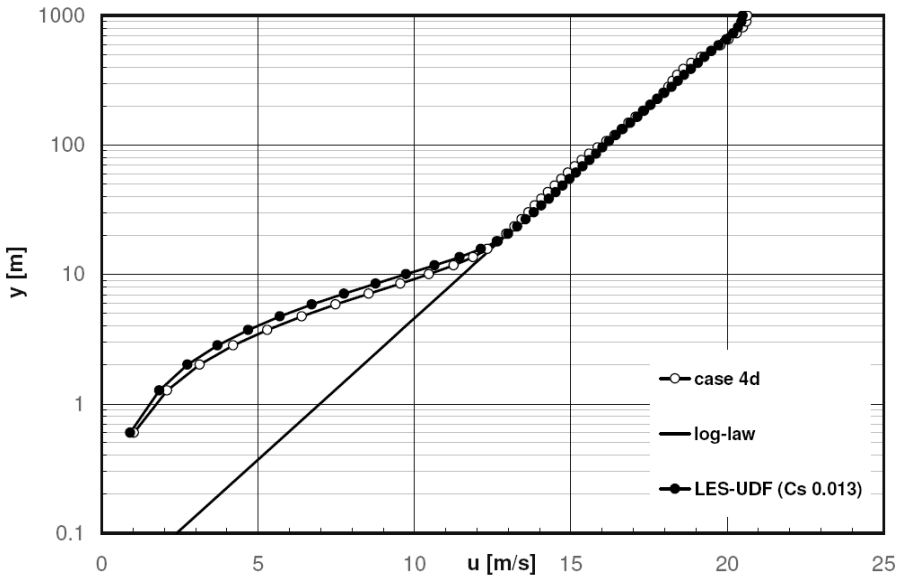

Figure 5.10 – Vertical profiles of velocity for DES 4d and LES-UDF.

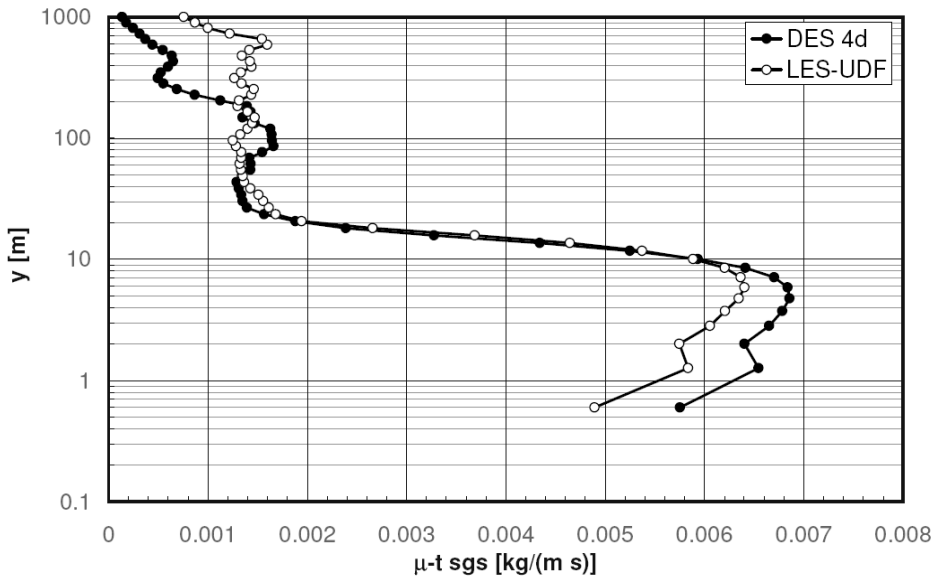

Figure 5.11 – Vertical profiles of SGS eddy viscosity for DES 4d and LES-UDF.

5.5 SIMULATIONS DES 3D

A series of DES 3D simulations over flat terrains have been carried out with some of the settings tested in 2D tests, presented in previous paragraphs. The simulations were performed over a domain 3 km wide in both horizontal directions and 1 km high. The relative numerical results are presented in the this and following paragraphs; a roughness sensitivity study has been carried out considering three values of roughness length: 0.03 m, 0.16 m and 0.5 m.

The roughness length of 0.16 m was chosen in order to make comparisons with the numerical results by Sullivan *et al.* (1994) [34] whose simulations were performed for the same value of roughness length, same domain size but higher resolution both horizontal and vertical, different boundary condition for the top surface. Moreover, Sullivan *et al.* (1994) [34] adopted for their LES simulations a different SGS model and different C_S equivalent parameters, comparisons with the presented results are therefore more qualitative than quantitative.

The DES model with settings 4d has been tested on a domain whose discretization main features are listed in table below while the same geometric

features of the discretised domain used by Sullivan *et al.* (1994) [34] are given in the Table 5.4.

Table 5.3 – Grids' features of the three simulations compared.

z_0 [m]	Lx, Ly [m]	Lz [m]	Nx, Ny	Nz	N	Δx, Δy [m]	h [m]
0,03	3000	1000	50	50	125 000	60	0,6
0,16	3000	1000	50	50	125 000	60	3,2
0,50	3000	1000	50	30	75 000	60	10

Table 5.4 – Grids' features of the discretised computational domain used by Sullivan et al. *(1994) [34].*

z_0 [m]	Lx, Ly [m]	Lz [m]	Nx, Ny	Nz	N	Δx, Δy [m]	h [m]
0,16	3000	1000	96	96	884 736	~ 30	-

The settings chosen for the DES model are the ones described in the paragraph 5.3.4 and identified as 4d which resembles the closer possible the Smagorinsky SGS model. The present simulations were aimed to assess the sensitivity of the DES model to different values of roughness of the terrain. The values of roughness length tested are 0,03 m, 0,16 m and 0,5 m, the first two corresponding to areas of low vegetation, while the third one is typical of a forested zone according to the classification of terrains, for instance the one proposed by the European Wind Atlas [39] and reported in Table 5.5. The used settings of the roughness parameters RH and RC for the three values tested have been already presented in Table 5.2.

The constant C_{DES} of the model has been set to 0,486 corresponding to a Smagorinsky constant C_S of 0,1 according to equation the equation (5.7) and Spalart-Allmaras model's constants as in Table 2.1.

Table 5.5 – Classification of the terrains based on the roughness length z_0 according to the Wind Atlas [39].

z_0 [m]	Terrain typology	Roughness Class
1-0,5	City – Forest	3
0,5 – 0,2	Suburbs – Shelter belts	3
0,2	Many trees and/or bushes	2-3
0,1	Farmland with closed appearance	2
0,03	Farmland with very few buildings, trees, *etc.*	1
0,01	Airport runway areas – mown grass	-
$3\ 10^{-4}$ - $1\ 10^{-4}$	Sand and water surfaces (smooth)	0

All the run DES 3D simulations were started from a perturbed RANS solution. The DES simulations were first left run for ten flow-through times in order to achieve a statistically steady turbulence, afterward the time statistics were gathered over an equal time window of ten flow-through times. The flow-trough time has been computed on the maximum velocity rather than on the bulk velocity.

The statistics gathered by default in Fluent 6.2 are the mean and the RMS values of the static pressure, velocity magnitude, x, y and z component of the velocity.

A more complete study of the turbulence would be achieved by calculating the co-variances of velocity components and higher order moments, while a spectral analysis of turbulence can also help to understand if the turbulence has been simulated correctly.

Nevertheless in the following paragraphs the most significant results are presented, usually as vertical profiles of variables averaged on horizontal planes.

The boundary conditions employed for both DES and LES simulations are slightly different than those usually employed in RANS simulations, for a flat terrain is convenient to set both the stream-wise and the span-wise borders as

translational periodic, in this fashion a fully developed situation is easily reproduced allowing at the same time to maintain a rather correct shape of the vortices in proximity of the lateral borders; the use of symmetry plane as lateral boundaries would kill all the turbulent fluctuations. The top of the domain is treated as a symmetry plane while the bottom as a wall with wall functions, these last two settings remained therefore the same used for RANS simulations.

A mass-flow has been assigned to the translational periodic condition, Table 5.6, aiming to produce a wind velocity of 15 m/s assuming that a log-law (equation (1.3)) would be valid over the whole domain.

Table 5.6 – Mass flows assigned at the periodic boundaries and physical time step.

z_0 [m]	Mass-flow [kg-s]	Time-step [s]	Max CFL cell number
0,03	$4{,}983\ 10^{+07}$	4	1
0,16	$4{,}883\ 10^{+07}$	4	1
0,50	$4{,}787\ 10^{+07}$	4	1

5.5.1 Wall-shear stress

The first type of numerical data that is going to be shown is the evaluation of the wall-shear stress by the code Fluent.

The contour plots of wall shear stress on the ground (Figure 5.12 for the smaller value of roughness tested, z_0 0.03 m) in the three cases studied show that the wall shear stress is higher in elongated areas parallel to the flow which are patterns of eddies organized in elongated structures whose length is not estimable since the periodic conditions make them like infinite long. The same behaviour has been described by Mason and Thompson (1992) [25] for computations performed with the standard Smagorinsky model. The authors claimed that the observed elongated structures are similar to the near-surface streaks found in low Reynolds number simulations of turbulent boundary layers. For this reason the observed elongated structures are named by some authors

super-streaks. Super streaks are structures not observed in actual turbulent boundary layers, they appeared also in hybrid RANS/LES simulations of a turbulent boundary layer, where the interface is placed in the logarithmic region around 30 y^+. In the mentioned hybrid RANS/LES simulations a shifting of the velocity profile in the logarithmic region is observed, this shift is accompanied by the presence of the super-streaks. In recent studies, for instance by Piomelli *et al.* [26], the introduction of a stochastic forcing at the interface allowed to reduce the shift in the velocity profile in the proximity of the interface while the super-streaks structures disappeared. A rather similar phenomena is observed in a WMLES and DES of the ABL over rough surfaces. A stochastic forcing of the velocity field could likely improve the simulations performed.

Unfortunately, the shortness of the domain together with the stream wise periodic conditions enhances the permanence of elongated structures; with the hazard of construct structure infinitely long if the size of the structures is comparable to the length of the domain.

By averaging the value of wall shear stress predicted by the DES simulations values are obtained that are smaller than the wall shear stress calculated by RANS SKE simulations and even smaller than the reference value which is computed considering valid the log-law (1.3) for the whole domain and for the given mass-flow (Table 5.6); the three values of wall-shear stress are summarized in the table below, the corresponding friction velocities are linked to the wall-shear stress by its definition, equation (1.1).

Table 5.7 – Wall-shear stresses and friction velocities for log-law (1.3), SKE-RANS and DES 4d simulations.

		Logarithmic law		**RANS SKE**		**DES 4d**	
z_0 **[m]**	Δx **[m]**	$\tau_{w-LOG-LAW}$ **[Pa]**	$u_{\tau-ref}$ **[m/s]**	τ_{w-SKE} **[Pa]**	$u_{\tau-ske}$ **[m/s]**	$\langle \tau_w \rangle_{DES}$ **[Pa]**	u_τ **[m/s]**
0,03	60	0,445	0,603	0,387	0,562	0,167	0,370
0,16	60	0,633	0,719	0,514	0,648	0,245	0,447
0,50	60	0,836	0,826	0,643	0,724	0,374	0,553

There is a constant tendency for the DES 4d performed to underestimate the friction velocity, the value calculated is generally 60% of the reference value.

The tendency to underestimate the wall-shear stress is directly connected to the typical local deviation from a logarithmic profile ("overshoot") in the velocity profiles observed which occurs in the surface layer. Instead the velocity gradient is higher than expected in the same zone where super-streaks are observed.

According to Mason and Thompson (1992) [25] the presence of the "overshoot" is connected to the lack of backscatter of turbulent kinetic energy from smaller to bigger vortices; in the simulations by Mason and Thompson (1992) [25] the lack of backscatter was due to the use of the Smagorinsky SGS model which is a pure dissipative model as all the eddy viscosity models.

One of the questions to be answered in the present chapter is to understand if the DES model predicts the "overshoot" typical of the Smagorinsky model, and if this appears how much it differs from a log-law and from other cases.

It has to be pointed out that, when some variables will be presented normalized by using the friction velocity, the underestimation of the friction velocity can lead to an amplification or to a reduction of the normalized group. Therefore both the non-dimensional groups based on computed friction velocity and reference (based on log-law) friction velocity are presented in the following sections of this report.

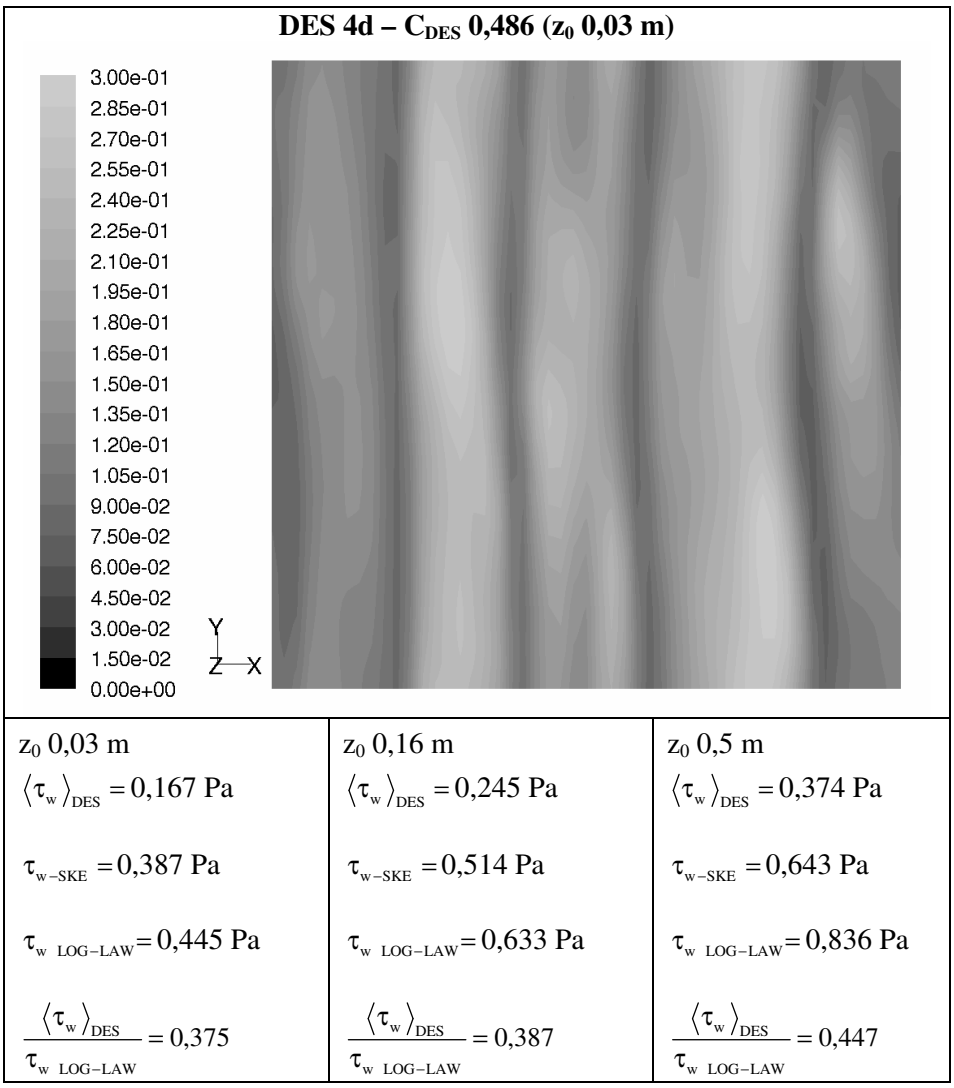

Figure 5.12 – Contours of wall shear stress [Pa] on the ground for the z_0 0,03 m (above); averaged values for DES and RANS SKE are reported with their reference value (log-law) for all the three cases.

5.5.2 Velocity profiles

In Figure 5.13 the vertical velocity profiles are shown, computed by averaging on horizontal planes the already time averaged stream-wise velocity component. Two trends are particularly clear, firstly, in the cells close to the

wall for which it results $d < C_{DES}\ \Delta$, in the RANS region, a logarithmic behaviour is fairly reproduced, in the interface RANS/LES the velocity profiles deviate from the log-law, a behaviour typical also of simulations performed with standard Smagorinsky-Lilly model, at a certain distance from the wall the logarithmic profile is once again recovered.

The velocity profiles are then normalized with the friction velocity computed and the one of reference (calculated assuming valid a log-law in the whole flow field and with the given mass flow) and plotted against z/z_0 respectively in Figure 5.14 and Figure 5.15, it's clear that the missing overlapping of the curves obtained with DES 4d simulations and the log-law curve of equation (1.3) come from the underestimation of the friction velocity; from the collapsing of the curves in Figure 5.15 can be another time highlighted how the expected friction velocity should be closer to the one of reference than the one computed.

In Figure 5.16 a comparison is presented with the baseline model by Sullivan *et al.* (1994) [34], in both cases the velocity profile deviates from the logarithmic law, in the profile relative to the simulation DES 4d the low value of predicted wall shear stress, i.e. of friction velocity, leads to amplify the value of normalized velocity, moreover a value of the model's constant C_{DES} higher than 0.486 should bring the profile computed to a shape closer to both the log-law and the Sullivan's baseline model.

In the Figure 5.17 the velocity profiles are shown in wall-coordinates u^+ y^+, this plot helps to understand if the boundary condition for the rough surfaces has been applied correctly, expecting a value of ΔB of equation (2.32) corresponding to the given roughness length z_0; in Figure 5.17 it can be seen as the ΔB seems to be better predicted for the lower values of roughness length.

In order to even better highlight and estimate the "overshoot" of velocity given by the model the normalized wind-shear ϕ_m defined by equation (1.4) is shown in Figure 5.18, in the three cases studied the "overshoot" in ϕ_m ranges between 2,6 and 3,4 where the value of a log-profile is 1.

It can be pointed out that tests made with a grid with double horizontal resolution ($\Delta x = \Delta y = 30$ m) and half horizontal dimensions (1500 m) of the domain to keep the same number of cells, not shown here, gave a less dramatic "overshoot".

5.5.3 Eddy-viscosity profiles

In Figure 5.19 and Figure 5.20 vertical profiles of SGS turbulent viscosity are shown, averaged on horizontal planes, the maximum of turbulent viscosity occurs around 30 m of altitude regardless the roughness length. The poor vertical resolution of the grid drawn for the most rough case doesn't allow to make a good estimation of the SGS viscosity maximum. Nevertheless the maximum value results higher for the higher roughness tested which is influenced by the higher velocity gradients.

A way to normalize the turbulent viscosity is to multiply it by the vertical gradient of the stream-wise velocity and divide by the wall-shear stress, the non-dimensional group obtained, plotted in Figure 5.21, should assume a value close to one at the surface if the SGS momentum flux is much higher than the resolved scale one. The described non-dimensional group collapses to the same value close to the wall for two out of three cases, for the most rough case the group falls on a value slightly smaller than unity but the trend looks generally acceptable.

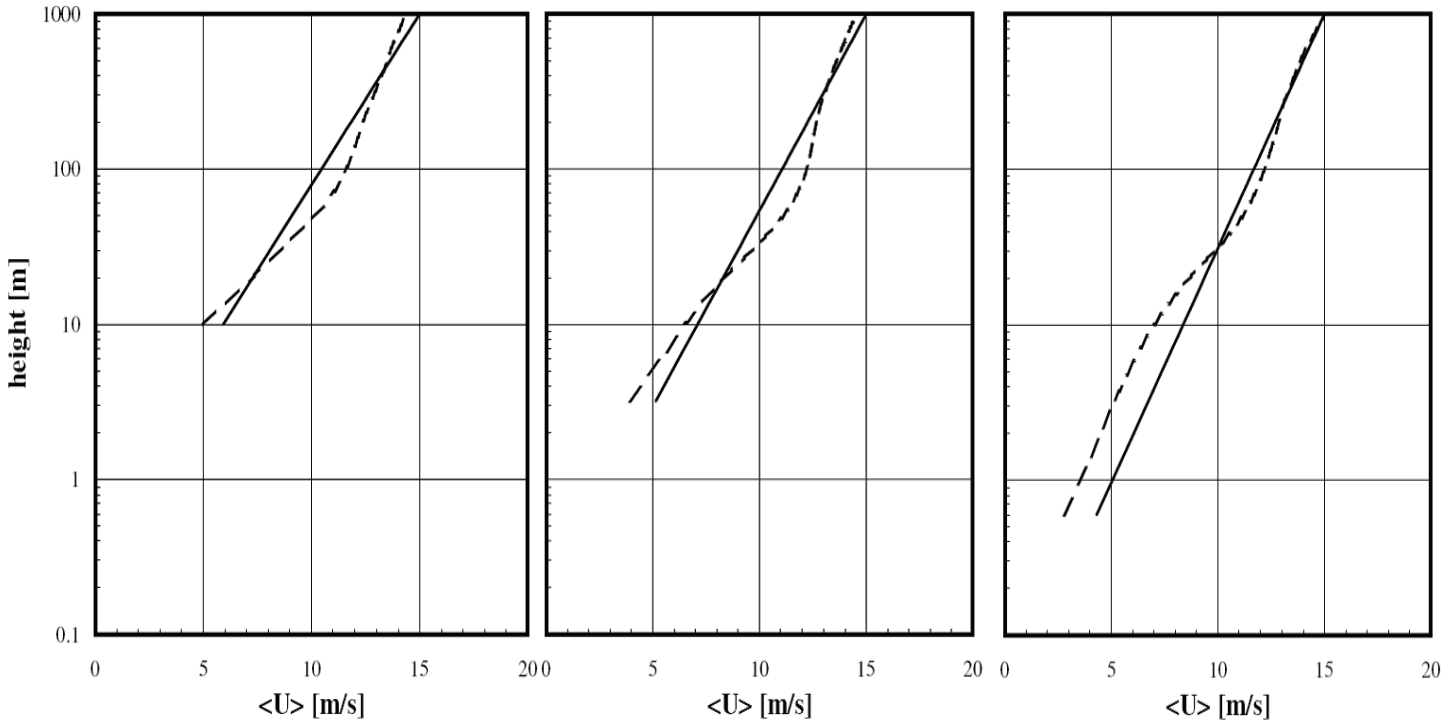

z_0 0,50 m z_0 0,16 m z_0 0,03 m

Figure 5.13 – Roughness sensitivity: velocity profiles, solid lines logarithmic laws, dashed lines horizontal plane averaged mean velocities.

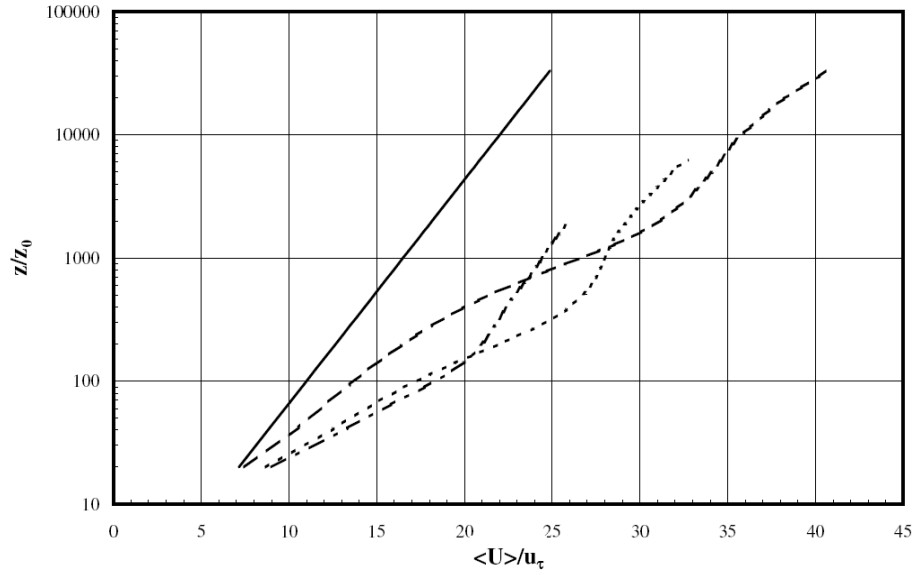

Figure 5.14 – Velocity profiles normalized with u_{τ} and z_0, solid line log-law (1.3), dashed line z_0 0,03 m, dotted line z_0 0,16 m, dashed-dotted line z_0 0,50 m.

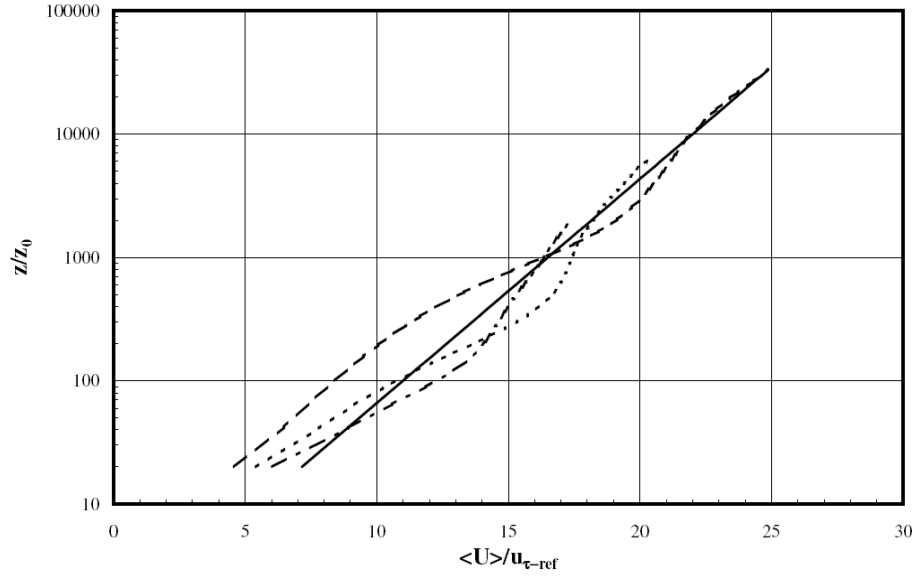

Figure 5.15 – Velocity profiles normalized with u_{τ} and z_0, solid line log-law (1.3), dashed line z_0 0,03 m, dotted line z_0 0,16 m, dashed-dotted z_0 0,5 m.

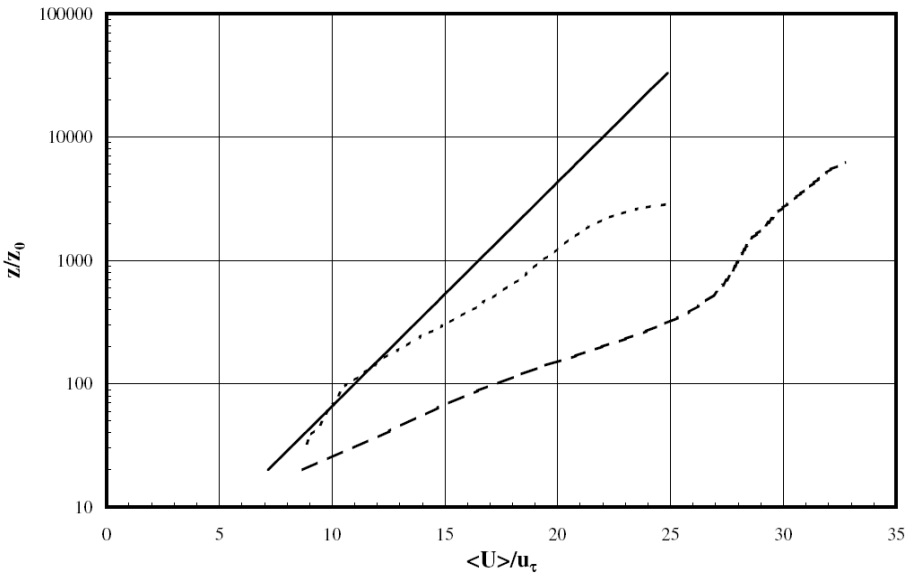

Figure 5.16 – Dashed line DES4d z_0 0,16 m, dotted line baseline model from Sullivan et al. *(1994) [34].*

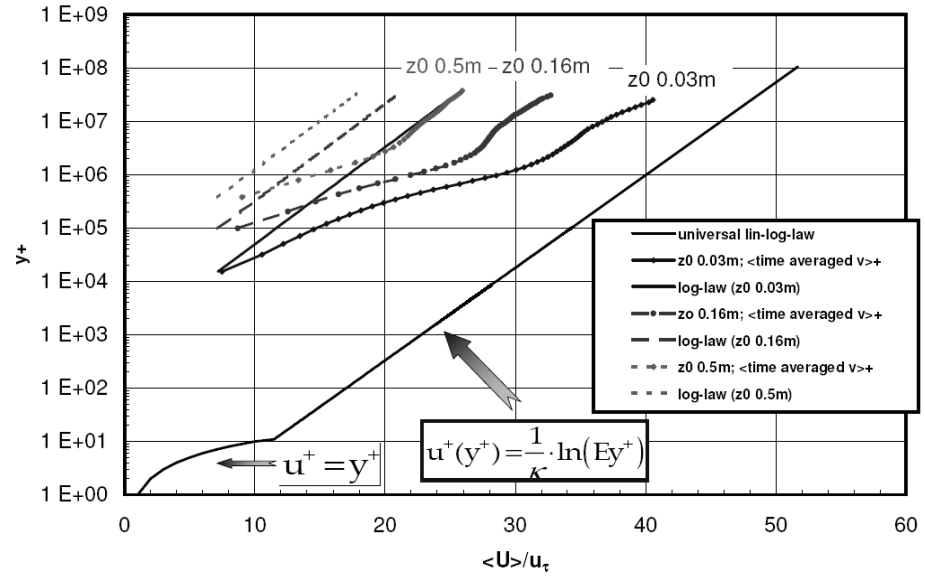

Figure 5.17 – Velocity vertical profiles in wall-coordinates.

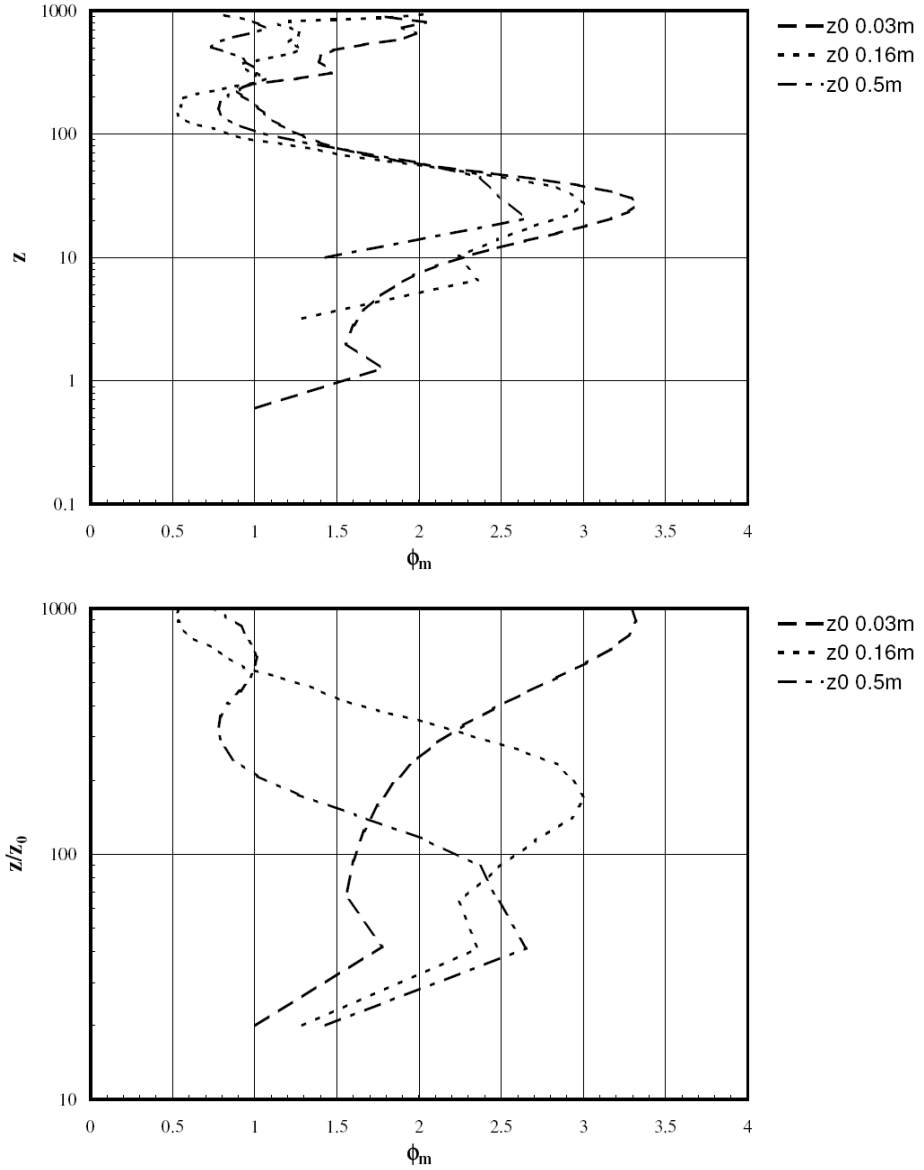

Figure 5.18 – Normalized-wind shear profiles.

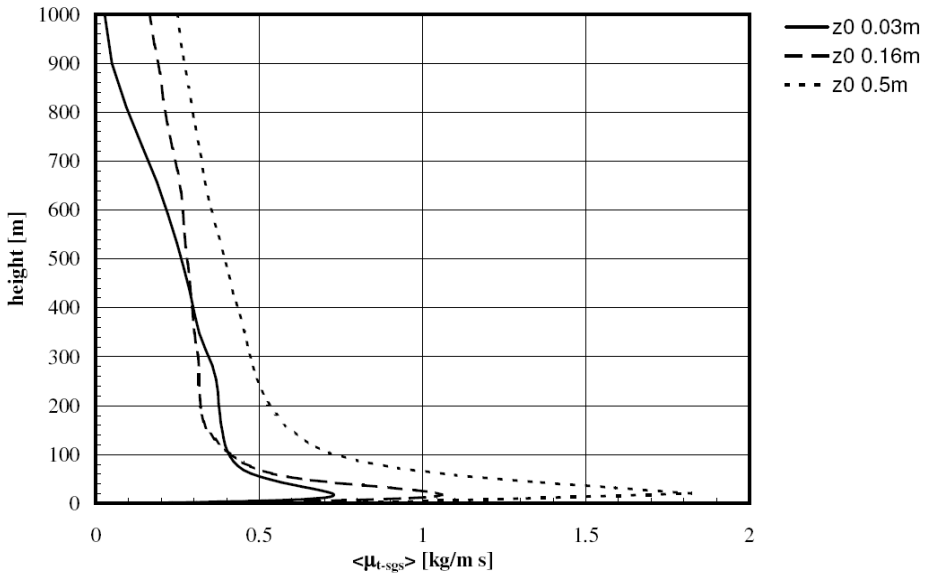

Figure 5.19 – SGS turbulent viscosity profiles, solid line z_0 0,03 m, dashed line z_0 0,16 m, dashed-dotted line z_0 0,5 m.

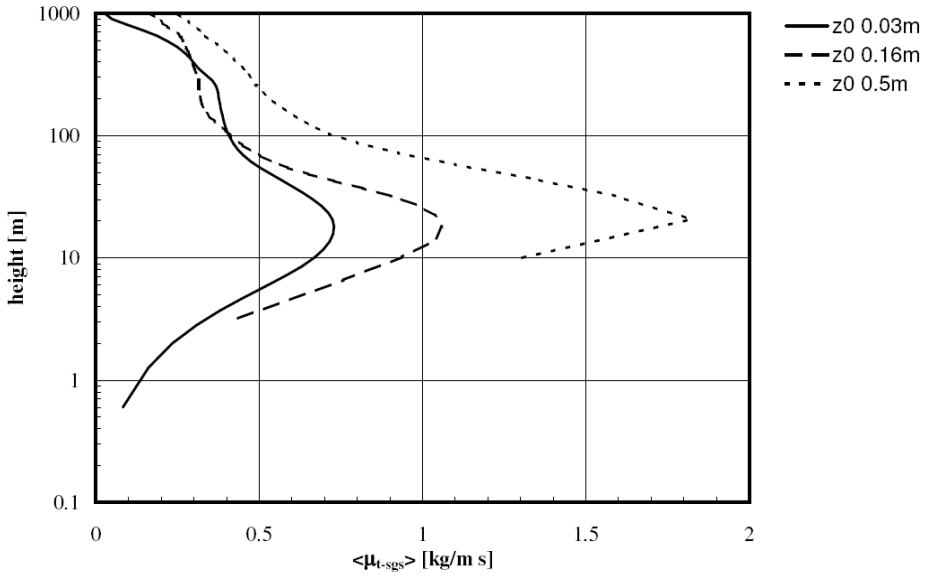

Figure 5.20 – Same values of Figure 5.19, semi-log coordinates.

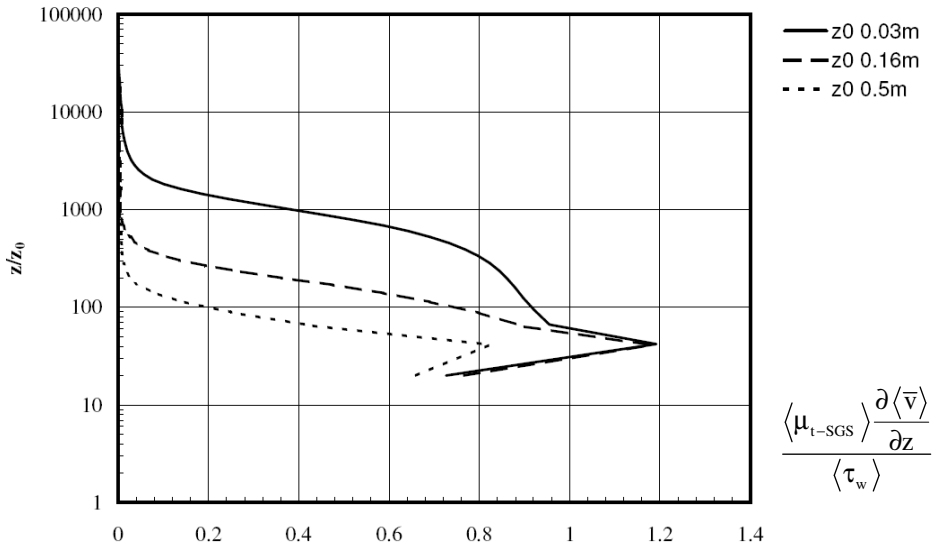

Figure 5.21 – Normalized SGS turbulent viscosity.

5.5.4 Velocity components variances profiles

The time RMS of the velocity components gathered by the code has been space averaged on horizontal planes in order to collect a set of vertical profiles, which are presented, both in dimensional form and in normalized form, in the following, Figure 5.22 and Figure 5.23. The RMS of the velocity components take into account only the resolved scale of the turbulence; the SGS part should be added to the resolved scale in order to reflect the whole turbulence, its influence is expected to be very important close to the terrain but negligible at a certain distance from the wall, in the surface layer.

Both the collapse of the data and the values close to the wall expected from similarity theory, equations (1.6), (1.7) and (1.8) lead again to evaluate as underestimated the wall-shear stress by the code while a friction velocity closer to the reference value looks more reasonable. It's certainly sure that for a more precise judgement of the variances the filtered part should be evaluated and summed.

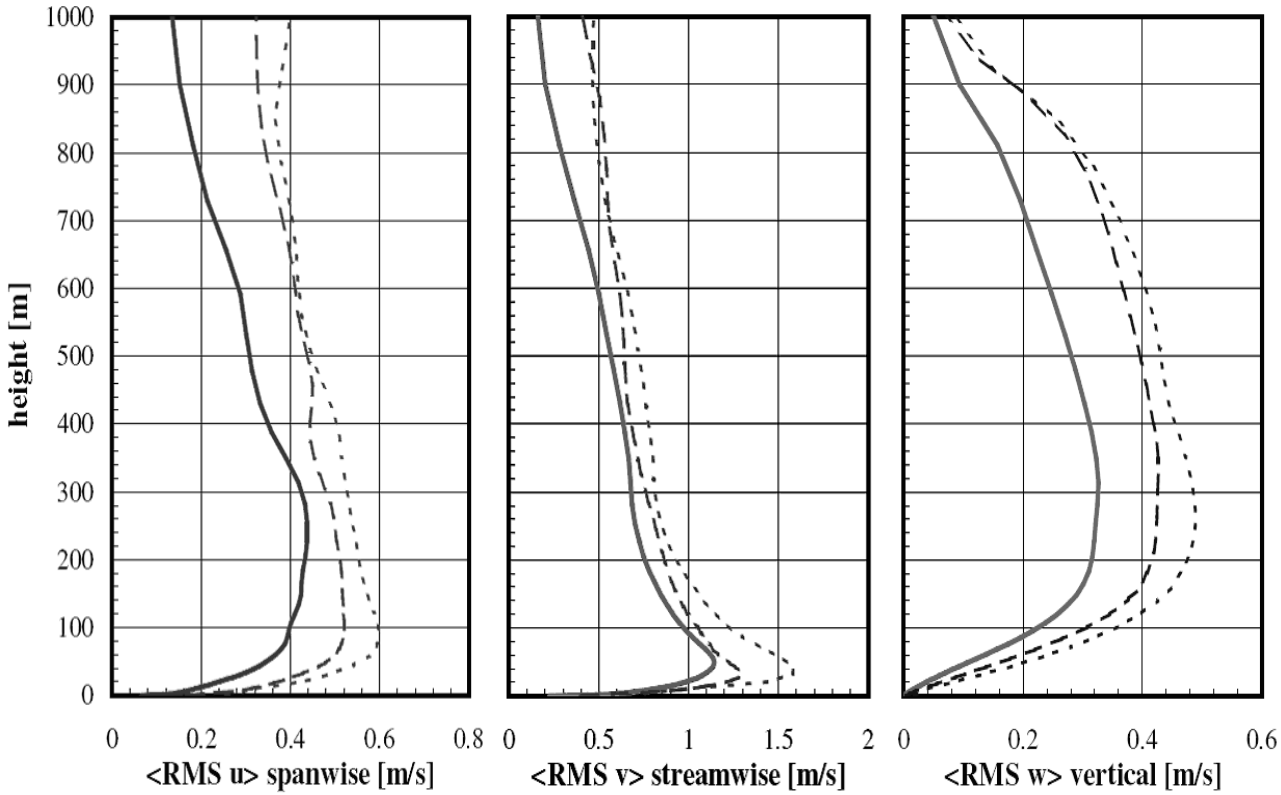

Figure 5.22 – Vertical profiles of RMS of velocity components. Solid lines: z_0 0,03 m; dashed lines z_0 0,16 m, dotted lines z_0 0,5 m.

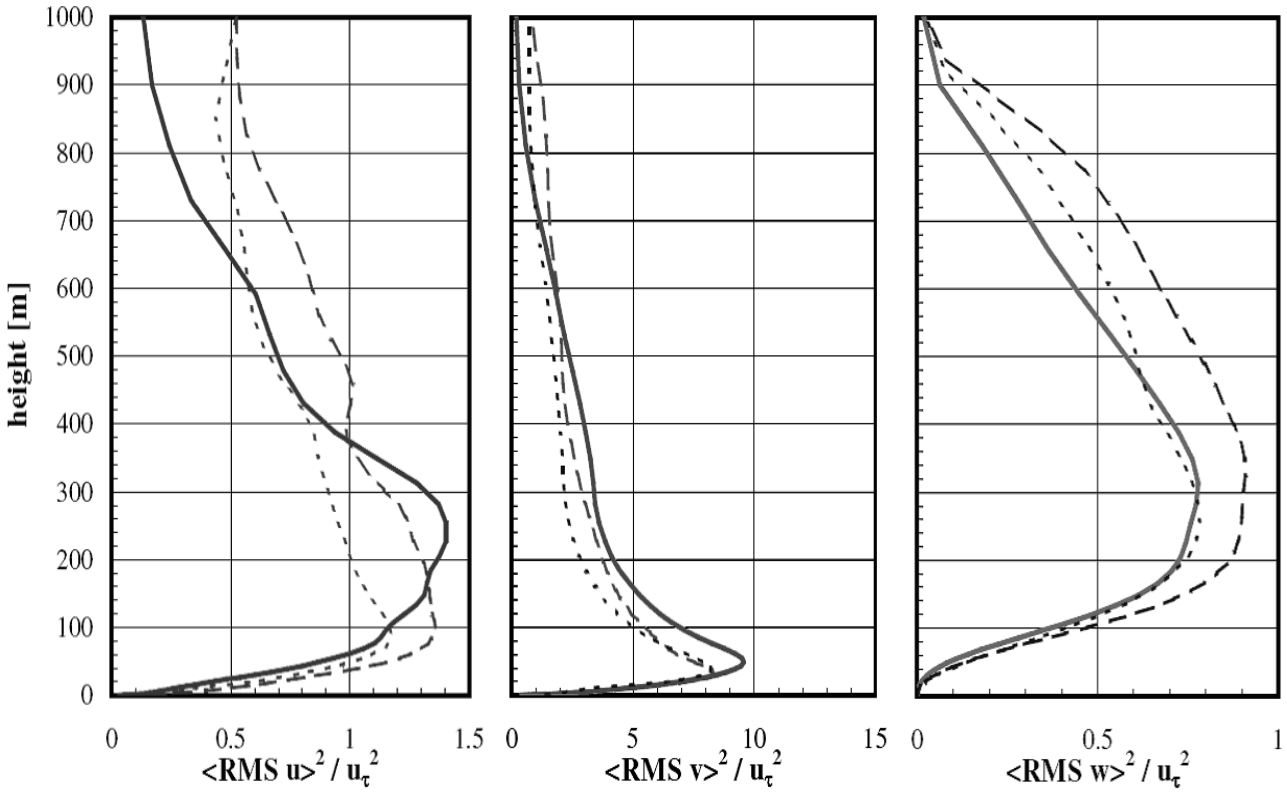

Figure 5.23 – Variances of velocity components normilized with predicted friction velocity. Solid lines: z_0 0,03 m; dashed lines z_0 0,16 m, dotted lines z_0 0,5 m.

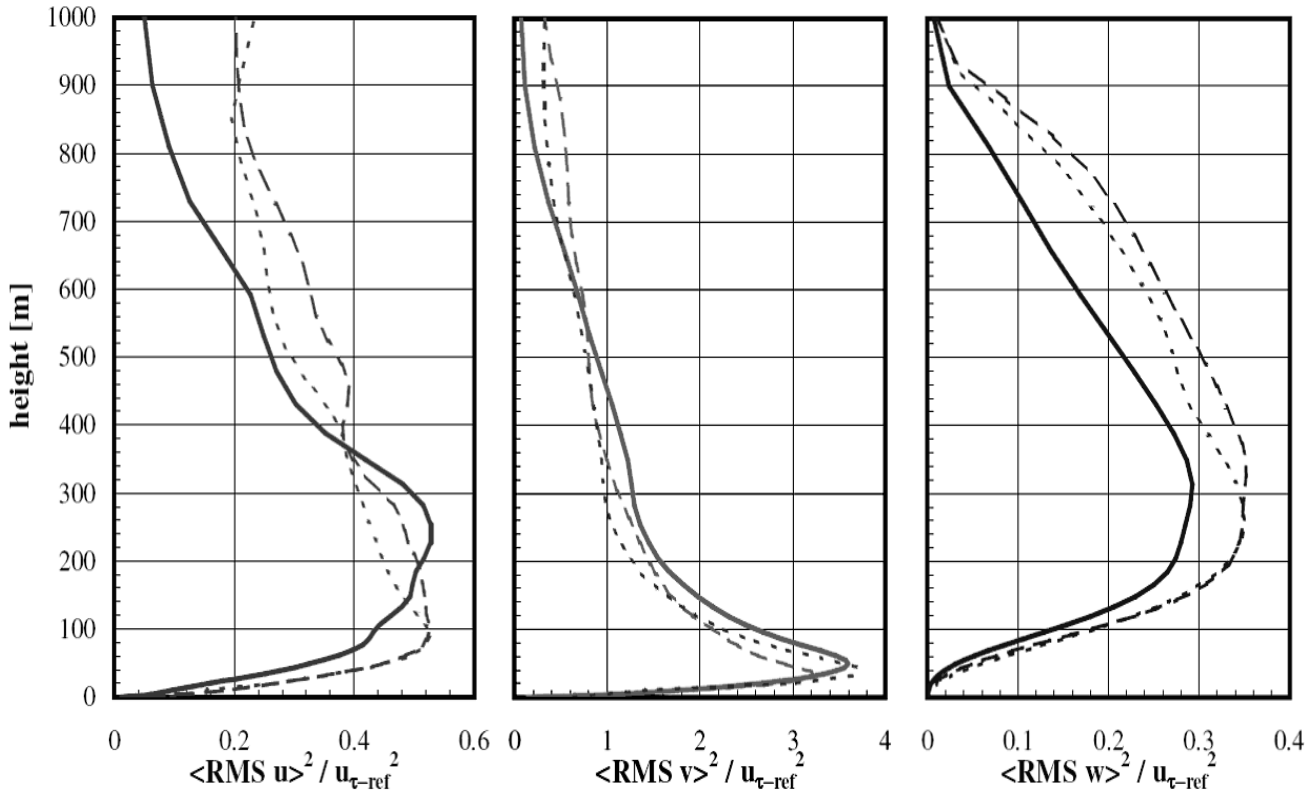

Figure 5.24 – Variances of velocity components normilized with reference (log-law) friction velocity. Ssolid lines: z_0 0,03 m; dashed lines z_0 0,16 m, dotted lines z_0 0,5 m.

5.5.5 Turbulent Kinetic Energy profiles

Turbulent Kinetic Energy profiles of resolved turbulence scale are shown in Figure 5.25, normalized values in Figure 5.26 and Figure 5.27. Since the TKE is computed from the RMS of velocity components the behaviour shown is the same observed for the RMS of the velocities plots, while an higher value of turbulence is fairly reproduced for the higher roughness since the higher velocity gradients, in the normalized profile a rather parabolic profile is shown, which resembles the expected profiles.

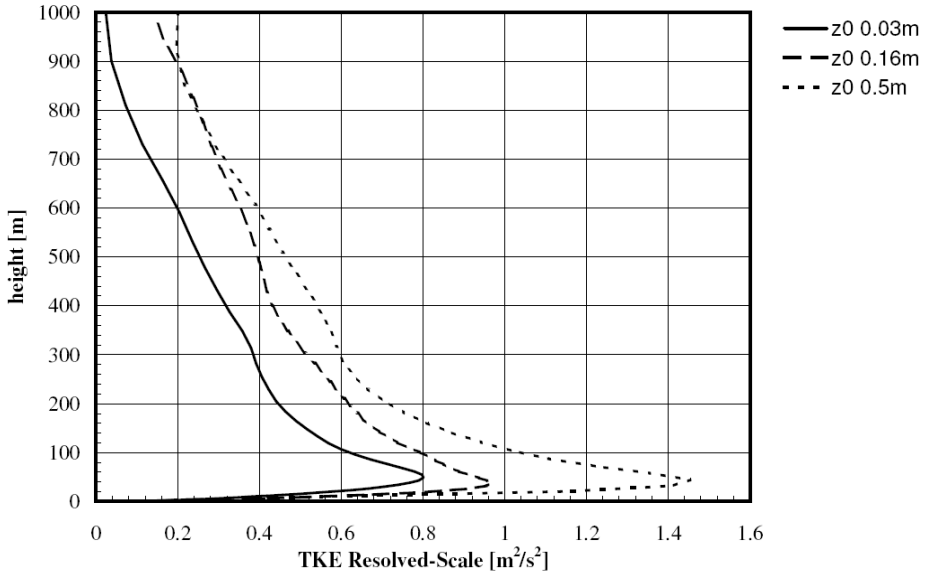

Figure 5.25 – TKE resolved scale vertical profiles for the DES4d simulations.

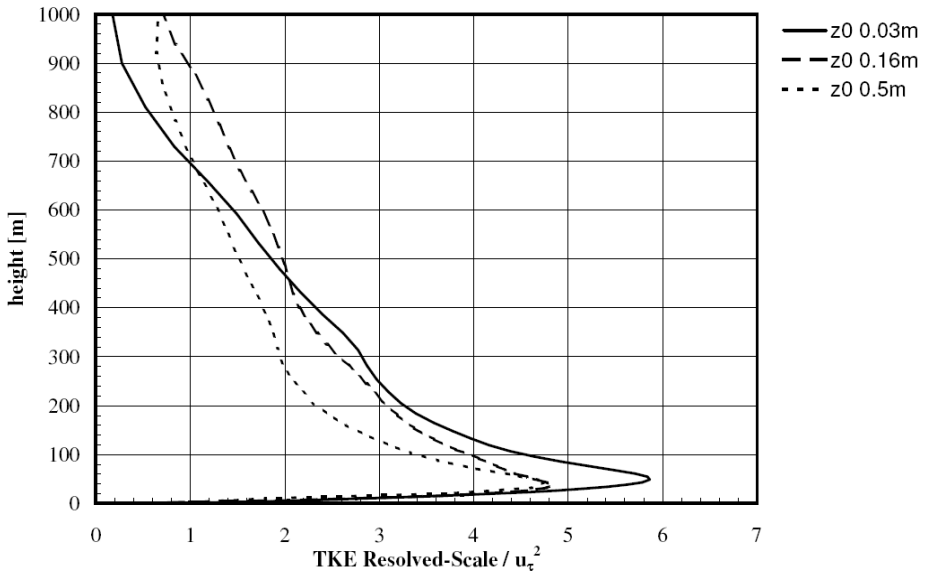

Figure 5.26 – TKE resolved scale vertical profiles normalized with computed friction velocity for the DES4d simulations.

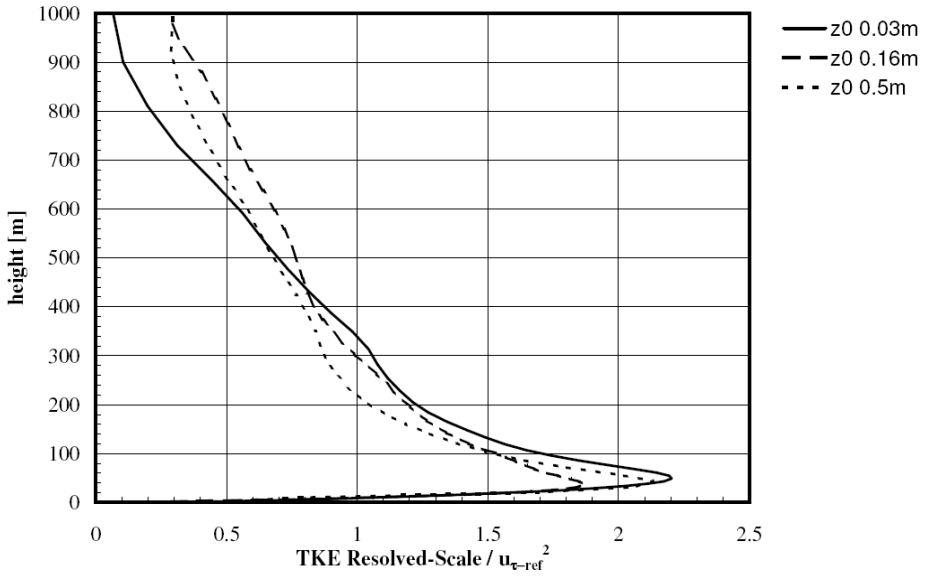

Figure 5.27 – TKE resolved scale vertical profiles normalized with reference friction velocity for the DES4d simulations.

5.5.6 Comparison with literature

Among the cases presented in literature the simulations by Sullivan *et al.* (1994) [34] have been chosen for comparison with the performed simulations, even if the model used in [34] is not the same analysed in this section. In fact Sullivan and collaborators compared two eddy-viscosity SGS models, both considering an extra transport equation for the SGS energy *e* which in equilibrium conditions (production of *e* equals dissipation ε) resembles the standard Smagorinsky model with C_S 0,18.

The main features for the meshes tested and the one in [34] are summarized in Table 5.8. The horizontal resolution in the meshes used in the simulations by Sullivan is approximately 30 m and, since it's preferable compare results for same resolutions, two DES4d simulations are here presented, one with Δx 60 m and Lx 3000 m and one with Δx 30 m and Lx 1500 m, where for the latter the resolution is fairly comparable with the resolution of the grids used in [34].

The filter width based on the cell-volume for the two grids employed is plotted in Figure 5.28. In Figure 5.29 the normalized velocity profile and in Figure 5.30 the normalized wind shear, both the figures show a better prediction of the velocity field by the more refined grid, showing a grid dependency of the results. Further improvements could be expected with a C_{DES} higher, corresponding to $C_S = 0,18$.

Figure 5.31 and Figure 5.32 show vertical profiles of resolved scale TKE. Figure 5.33, 5.34 and 5.35 show vertical profiles of RMS of velocity components compared to Sullivan's baseline model results and curves from similarity theory. Not perfect agreement is found between the compared cases. It has to be stressed that the vertical profiles presented are referred only to the resolved scale while Sullivan added to the resolved scale RMS of velocity components a SGS contribution calculated on the SGS eddy viscosity

What it can be seen from the vertical profiles Figure 5.33-5.35 of the RMS on the velocity components is that there is a main tendency in under predict the not-stream-wise, especially for the span-wise direction. Moreover the profiles

result comparable only in the case of similar resolution (Δx 30 m for DES4d case).

Table 5.8 – Grids' features of the three simulations compared.

	z_0 [m]	Lx, Ly [m]	Lz [m]	Nx, Ny	Nz	N	Δx, Δy [m]	h [m]
DES 4d	0,16 m	1500	1000	50	50	125 000	30	3,2
DES 4d	0,16 m	3000	1000	50	50	125 000	60	3,2
Sullivan *et al.* [34]	0,16 m	3000	1000	96	96	884 736	~ 30	

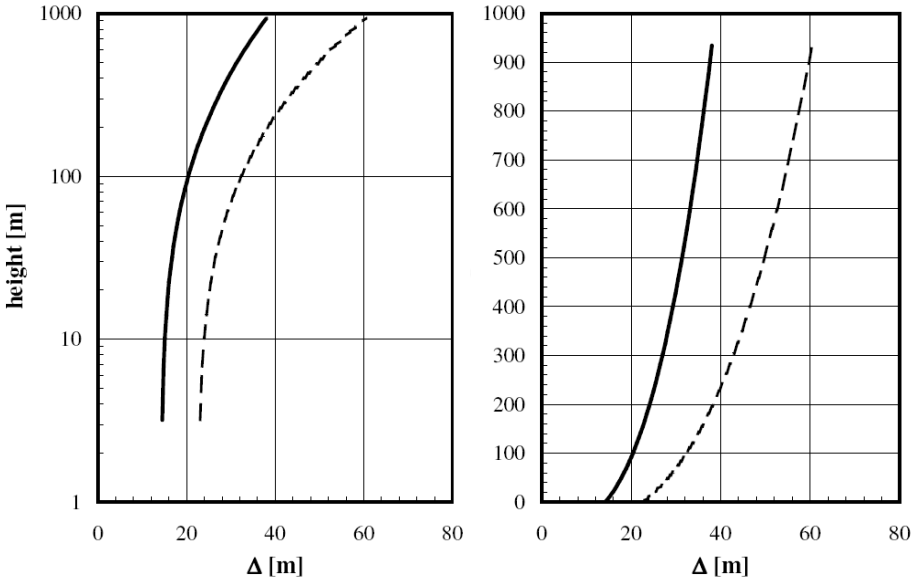

Figure 5.28 – Filter width based on cell-volume: solid line domain 1,5 km x 1,5 km (Δx, Δy 30 m), dashed line domain 3 km x 3 km (Δx, Δy 60 m).

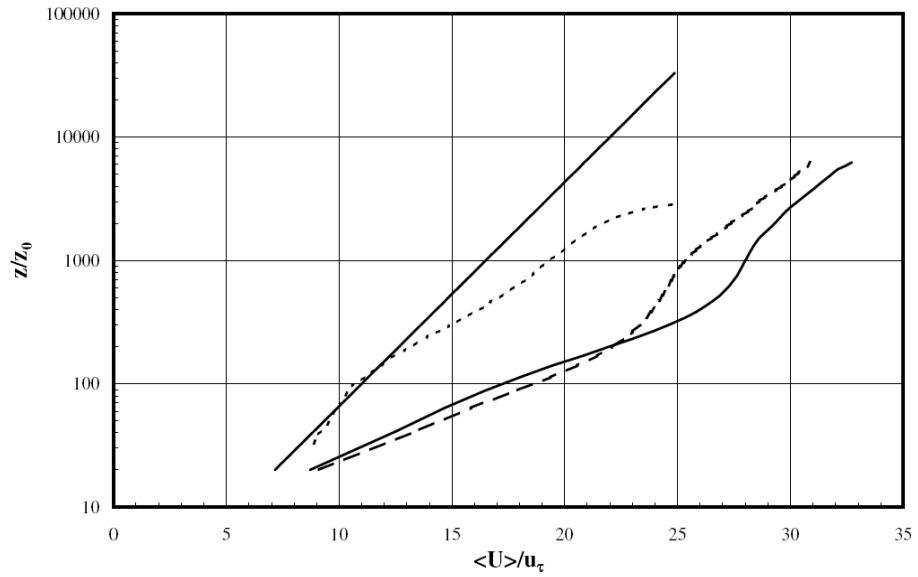

Figure 5.29 – Velocity profiles in non-dimensional units, solid line for domain 3 km x 3 km, dashed line domain 1,5 km x 1,5 km, dotted line Sullivan's baseline model.

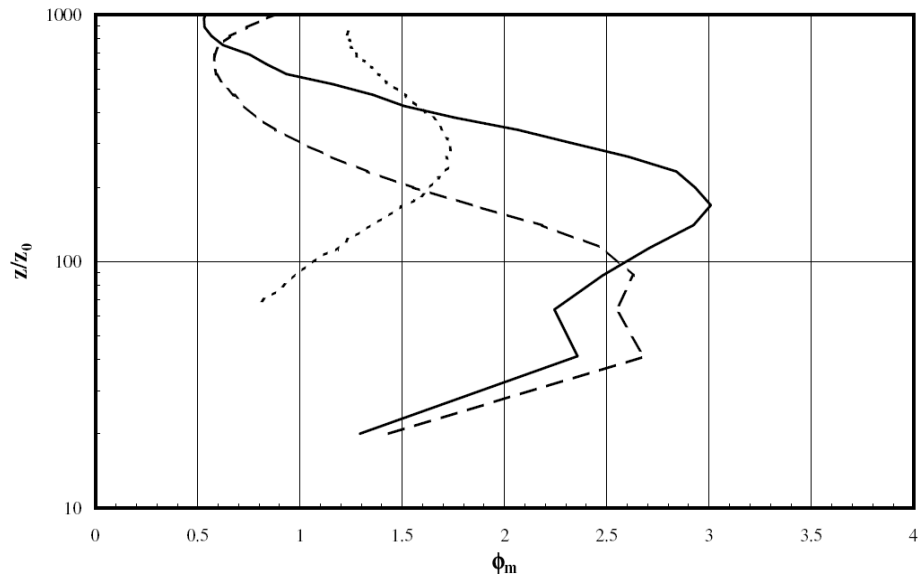

Figure 5.30 – Normalized wind shear, solid line domain 3 km x 3 km, dashed line domain 1,5 km x 1,5 km, dotted line Sullivan's baseline model.

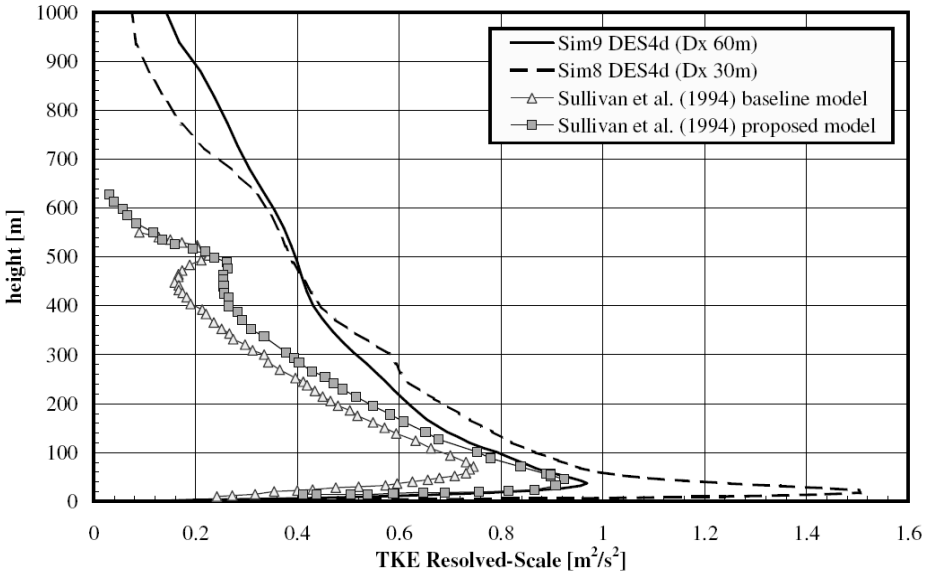

Figure 5.31 – Vertical profile of TKE resolved scale.

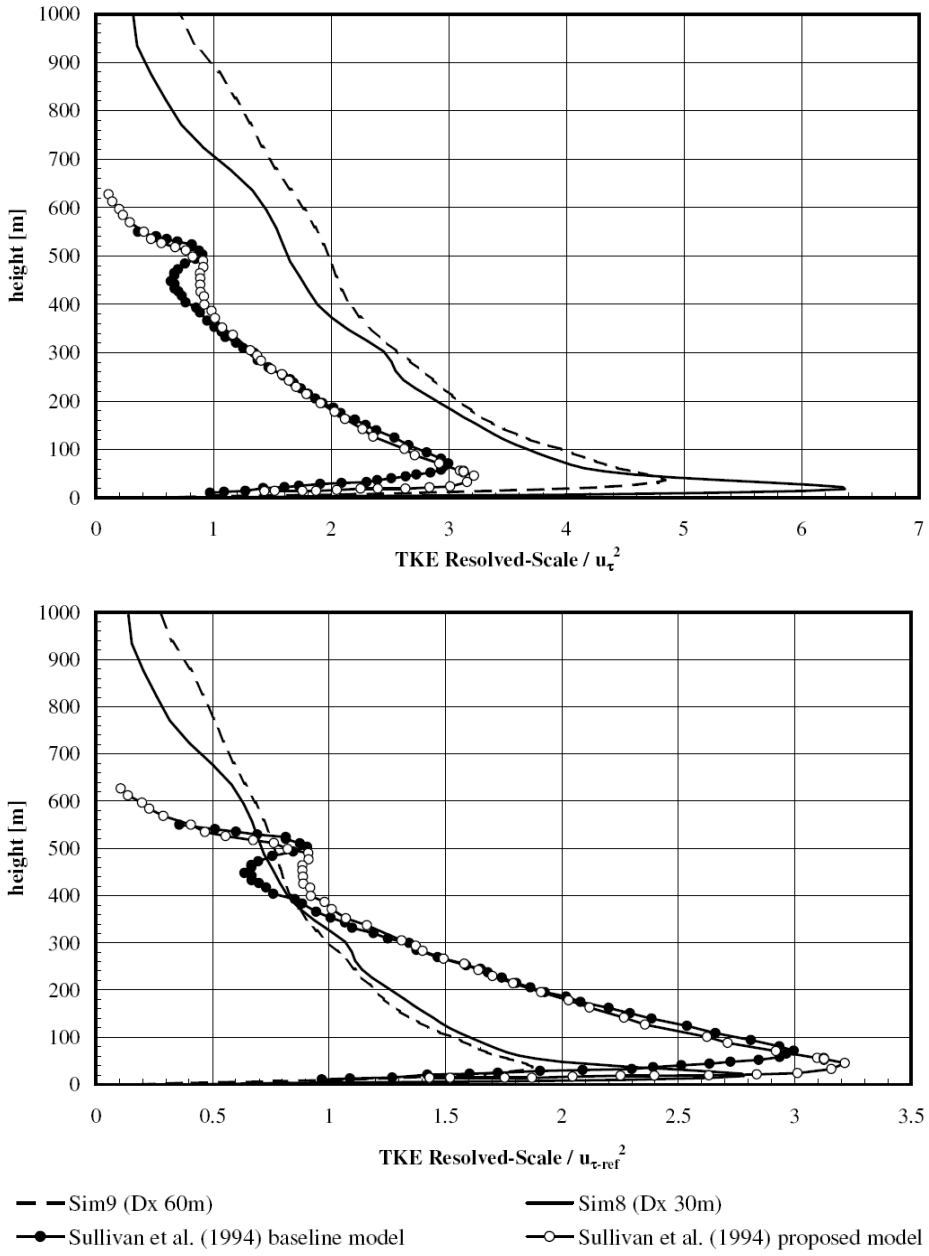

Figure 5.32 – Vertical profiles of normalized TKE.

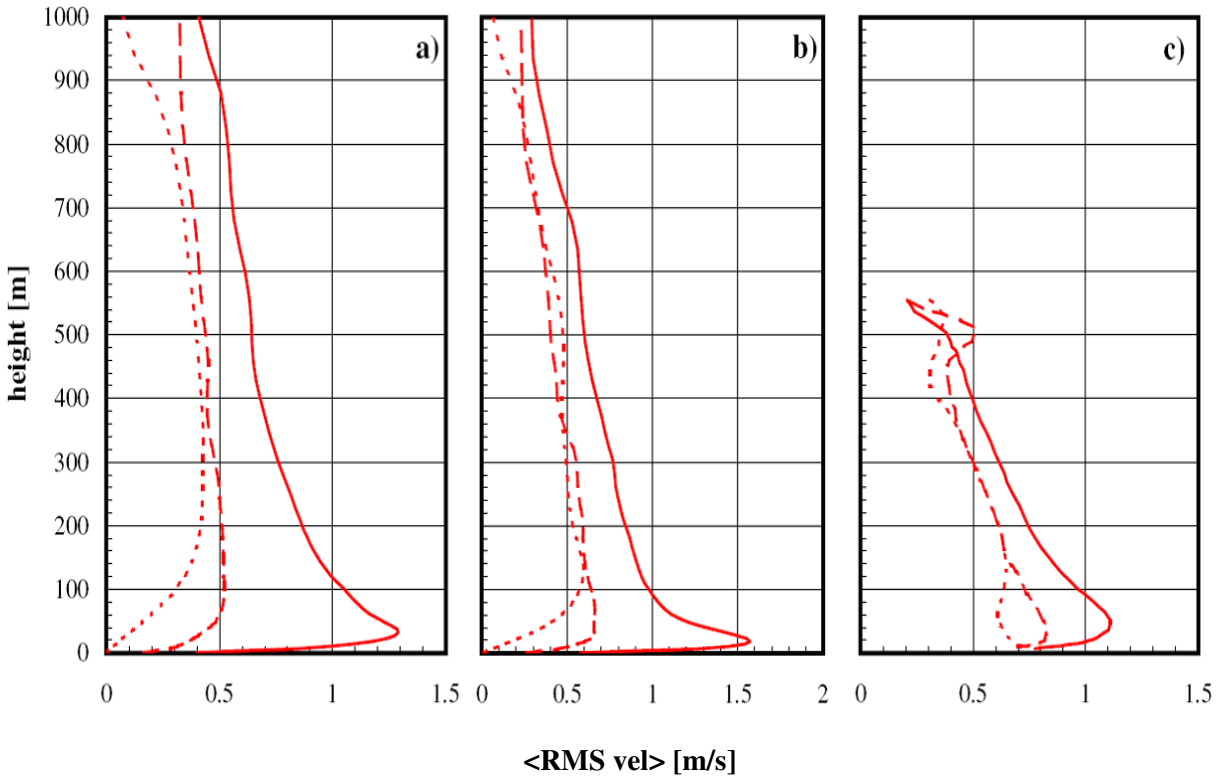

Figure 5.33 – RMS of the velocities: solid lines stream-wise component, dashed lines span-wise component, dotted lines vertical component; a) DES 4d with Δx 60 m (resolved scale), b) DES 4d with Δx 30 m (resolved scale), c) baseline model [34] (total = resolved scale + SGS).

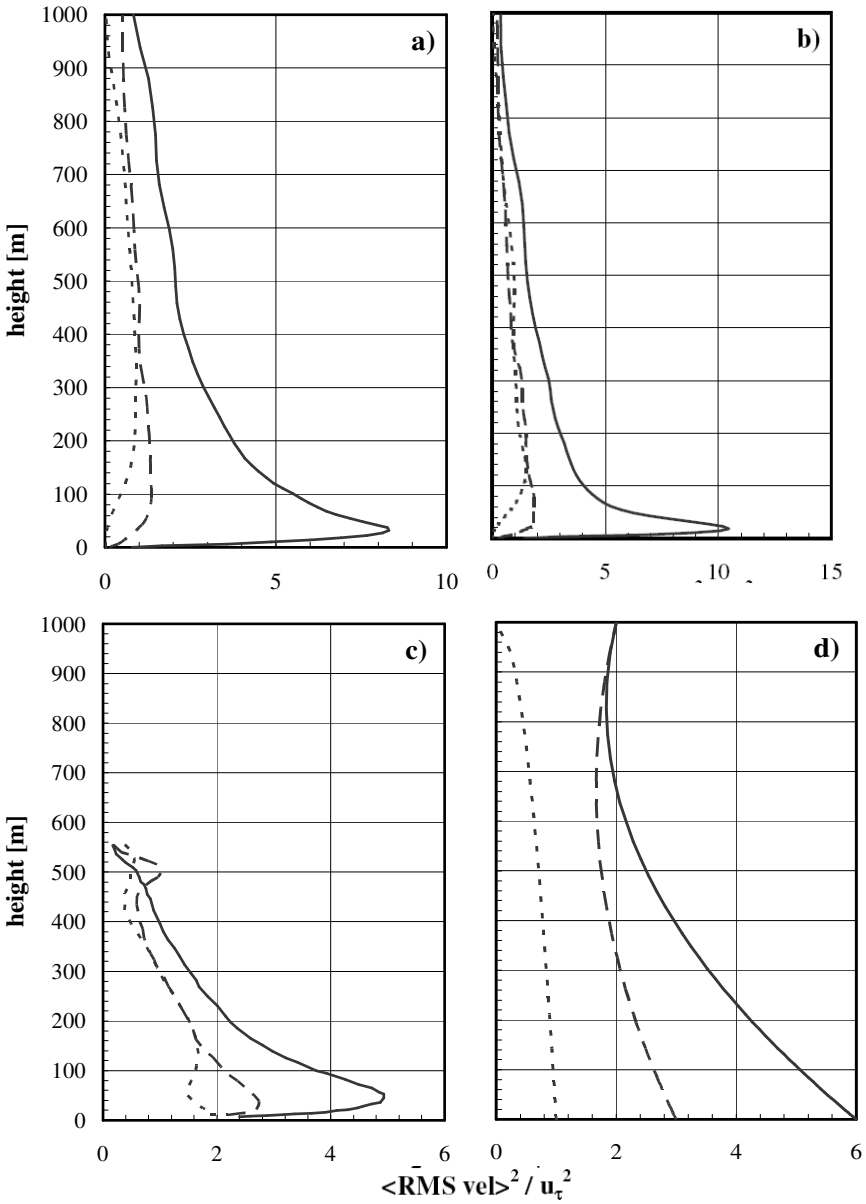

Figure 5.34 – Variances of the velocities normalized with computed friction velocity: solid lines stream-wise component, dashed lines span-wise component, dotted lines vertical component; a) DES 4d with Δx 60 m (resolved scale), b) DES 4d with Δx 30 m (resolved scale), c) baseline model [34] (total = resolved scale + SGS), d) similarity theory.

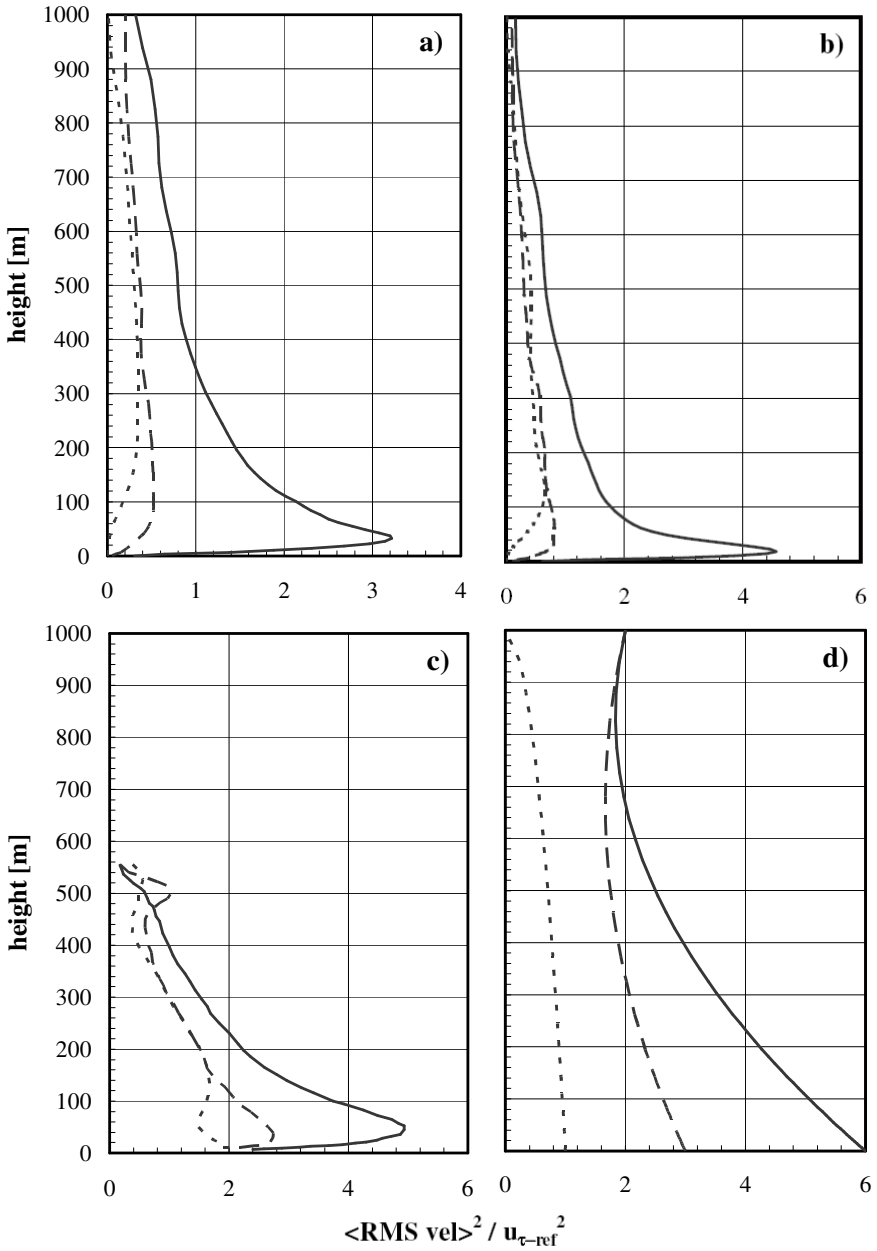

Figure 5.35 – Variances of the velocities normalized with reference friction velocity: solid lines stream-wise component, dashed lines span-wise component, dotted lines vertical component; a) DES 4d with Δx 60 m (resolved scale), b) DES 4d with Δx 30 m (resolved scale), c) baseline model [34] (total = resolved scale + SGS) (normalized with computed u_τ), d) similarity theory.

5.6 SIMULATIONS LES 3D OVER A ROUGH FLAT TERRAIN

5.6.1 A new LES-UDF to use with wall-functions

The only eddies-solving methodology which by default in Fluent allows to deal with rough surfaces is the DES module (based on SA model in Fluent 6.2), which have been tested and whose potentialities in reproducing an ABL have been investigated and presented in the previous section 5.5. Even if the DES model have been tested over a wide range of roughness length, not so satisfactory results have been obtained up to now which led to the idea to explore the possibility of implementation of a user defined function (UDF) to prescribe a SGS eddy viscosity.

Since Fluent allows to implement extra functions to model the SGS eddy-viscosity, an attempt has been done to build a classical Smagorinsky model. The aim of the function was to recalculate the eddy viscosity as wanted and to substitute the one given by the DES model.

Therefore, the first feature required by the testing of the function was to understand if the boundary conditions for rough walls were still enabled when a function is overwriting the calculated eddy-viscosity of the DES model.

The preliminary tests of the new SGS model gave positive results as concerns the application of the wall boundary conditions. Further tests have been carried out in order to quantify the sensitivity of the new model to some features like resolution of the grid both horizontal and vertical, the Smagorinsky constant C_S and roughness parameters.

The typical “errors” of the standard Smagorinsky model for the reproduction the surface layer of an ABL are well documented, for instance in Mason and Thompson (1987) [24] and (1992) [25]. The simulations presented in this section therefore don’t pretend to model correctly the ABL but are more aimed to reproduce the same results obtained by other authors with the Smagorinsky model in order to understand if the whole numerical procedure is properly set.

The Smagorinsky model has been implemented in the new function in its standard form, already described in Chapter 2 and the new LES-UDF tested on a set of structured grids whose main features are listed in Table 5.9; overall the cases performed with the new function were the four listed in Table 5.10.

In the domain 2 the number of vertical divisions has been increased to 60 to keep the expansion ratio under 1,1; the height of the first cell of 0,5 m is meant to be used with a roughness constant RC = E and a roughness height RH = z_0.

In the following paragraphs some features of the obtained flow fields will be described, comparison with the baseline model by Sullivan [34] are also done to assess the correctness of the procedure.

Table 5.9 – Grids' features of the three simulations compared.

	z_0 [m]	Lx, Ly [m]	Lz [m]	Nx, Ny	Nz	N	Δx, Δy [m]	h [m]
Domain 1	0,16	1500	1000	50	50	125 000	30	3,2
Domain 2	0,16	1500	1000	50	60	150 000	30	0,5
Domain 3	0,16	3000	1000	50	50	125 000	60	3,2

Table 5.10 – Cases analyzed for the LES UDF.

	Domain	RH [m]	RC	C_S
Case 1	1	1,17	1	0,1
Case 2	1	1,17	1	0,18
Case 3	3	1,17	1	0,1
Case 4	2	0,16	E	0,18

5.6.2 Wall-shear stress

As for the cases presented in the previous chapter on the DES simulations traces of elongated structures appear in the contour plots of wall-shear stress on the ground, see for instance Figure 5.36 for case 1, the same behaviour has been observed in all the tested cases. Moreover, these traces seem to be "infinite long" because of the periodic conditions and the shortness of the domain in the

stream-wise direction y, anyway passing from the domain of 1.5 km long to the one 3 km the traces of the super-streaks seem to cover still the whole domain.

As commented in the previous section 5.5 for DES simulations, the presence of "super-streaks" is very likely associated with an underestimation of wall-shear stress and the presence of an "overshoot" in the velocity profile, features that were therefore expected to be observed also in the LES simulations, as occurred.

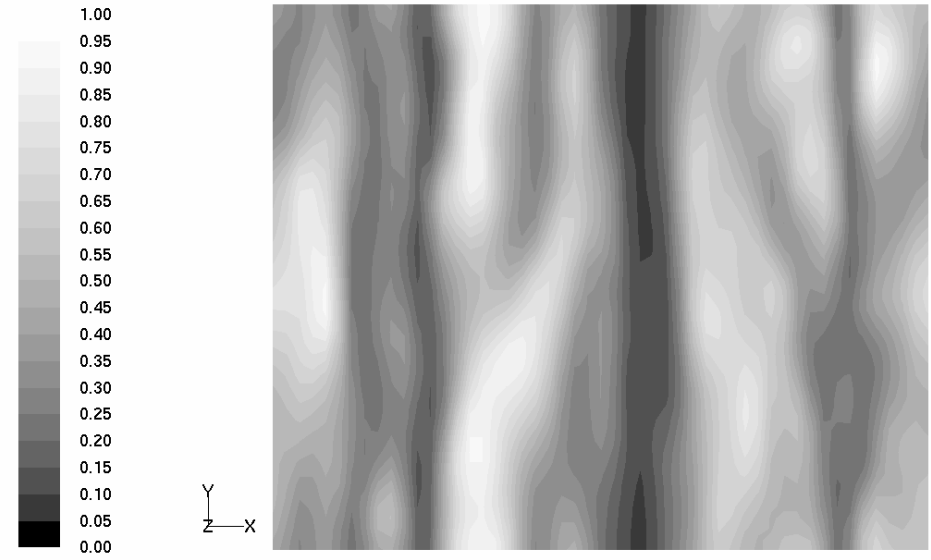

Figure 5.36 – LES-UDF, Contour plot of Wall-Shear Stress [Pa] (Case 1).

By averaging the wall shear stress on the ground it's obtained a value which is generally smaller than both the wall shear stress obtained with RANS SKE simulations and the theoretical value computed taking into account a log-law valid all over the domain. All the computed shear stresses are listed in the table below. From the case 4 it turns out that with an higher vertical resolution and a constant RC higher than one the friction velocity is much better predicted with both the SKE and the LES-UDF method.

Table 5.11 – Wall-shear stress and friction velocities for the cases analyzed with the new LES UDF.

	Mass-flow [kg/s]	$\tau_{w-LOG-LAW}$ **[Pa]**	$u_{\tau-ref}$ **[m/s]**	τ_{w-SKE}	$u_{\tau-ske}$ **[m/s]**	$\langle\tau_w\rangle_{LES}$	u_τ **[m/s]**
Case 1	2,5 10^{+7}	0,664	0,736	0,539	0,663	0,446	0,603
Case 2	2,5 10^{+7}	0,664	0,736	0,539	0,663	0,522	0,653
Case 3	4,883 10^{+7}	0,633	0,719	0,514	0,648	0,347	0,532
Case 4	2,5 10^{+7}	0,664	0,736	0,581	0,689	0,539	0,663

5.6.3 Velocity profiles

Vertical velocity profiles are presented in Figure 5.37, Figure 5.38 and Figure 5.39, normalized forms in Figure 5.40. In Figure 5.37 is shown how the Smagorinsky constant of 0,18 leads to a better velocity profile compared to the default value of Fluent 0,1. A C_S equal to 0,18 is by the way the theoretical value obtained by Lilly in equilibrium conditions and considering an inertial range with -5/3 law.

Figure 5.38 shows how the horizontal resolution influences the stream-wise velocity profile, since the slightly different boundary conditions (assigned mass flow), comparisons with normalized velocities are therefore more significant.

In Figure 5.39 the effects of a higher vertical resolution, especially close to the ground is shown, not satisfactory velocities are obtained within the canopy region, probably a mixing length defined from the wall distance in the cells close to the wall would help to have a velocity profile closer to the log-law above the canopy (inside the canopy a log law it's not expected).

The normalized wind shear, Figure 5.41, clearly shows an overshoot in all the cases studied, the smaller value of overshot is obtained for the case 2 with a maximum around 2,3, only slightly higher than the value obtained with the baseline model by Sullivan *et al.* (1994) [34].

5.6.4 Eddy viscosity profiles

In the SGS eddy-viscosity profiles, Figure 5.42 and Figure 5.43, are clear the effects of the Smagorinsky constant C_S, the eddy viscosity is proportional to the square of C_S and to the square of the filter width Δ. Moreover, unphysical and too high values of eddy-viscosity are predicted close to the wall, therefore the need of a alternative computation close to the wall which could be, for instance, the choice of the minimum value between $\kappa\, z$ and $C_S\, \Delta$ as mixing length as it's implemented in Fluent in its LES module. It would be interesting to see the results of the latter approach even if probably also a stochastic forcing would be necessary to achieve satisfactory results.

The domain vertical refinement doesn't give any improvement as in steady simulations; but likely, coupled with the corrections explained, stochastic forcing and a new mixing length close to the wall, it could produce important improvements.

5.6.5 Velocity variances profiles

The variances of the velocity components, resolved scale, are shown in Figure 5.44-Figure 5.47, the general behaviour is in the range of a neutral ABL, as already observed the friction velocity computed seems too low and consequently amplifying the normalized TKE, values of normalized groups obtained with the reference friction velocity look more realistic.

5.6.6 Turbulent Kinetic Energy vertical profiles

TKE profiles are presented in Figure 5.48, Figure 5.49 and Figure 5.50.

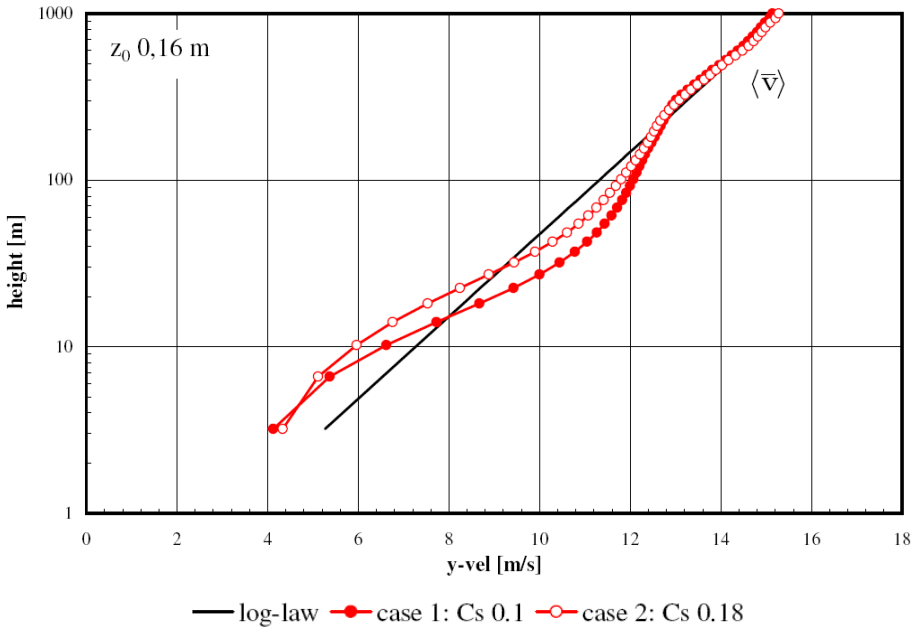

Figure 5.37 – vertical profiles of velocity (Smagorinsky constant effect): case 1 (Cs 0,1) and case 2 (Cs 0,18).

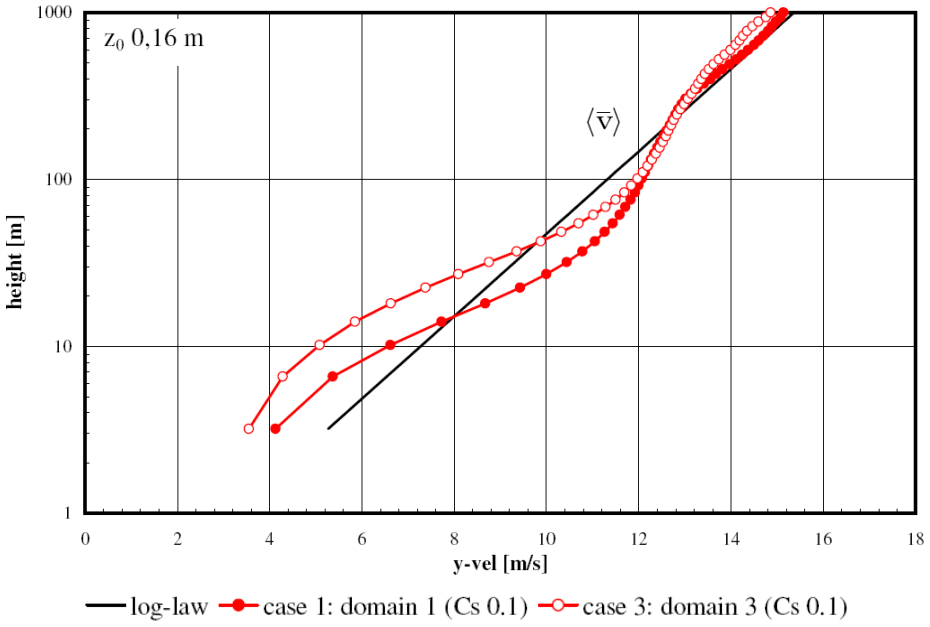

Figure 5.38 – vertical profiles of velocity (resolution effect): case 1 (domain 1, Δx 30 m) and case 3 (domain 3, Δx 60 m).

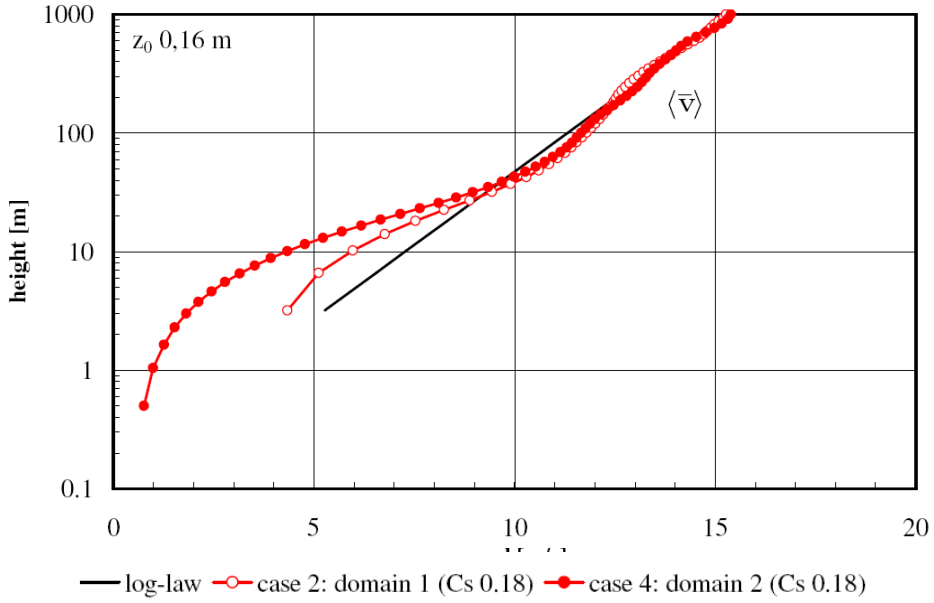

Figure 5.39 – vertical profiles of velocity (vertical resolution effect): case 2 (domain 1, h 3,2 m) and case 4 (domain 2, h 0,5 m).

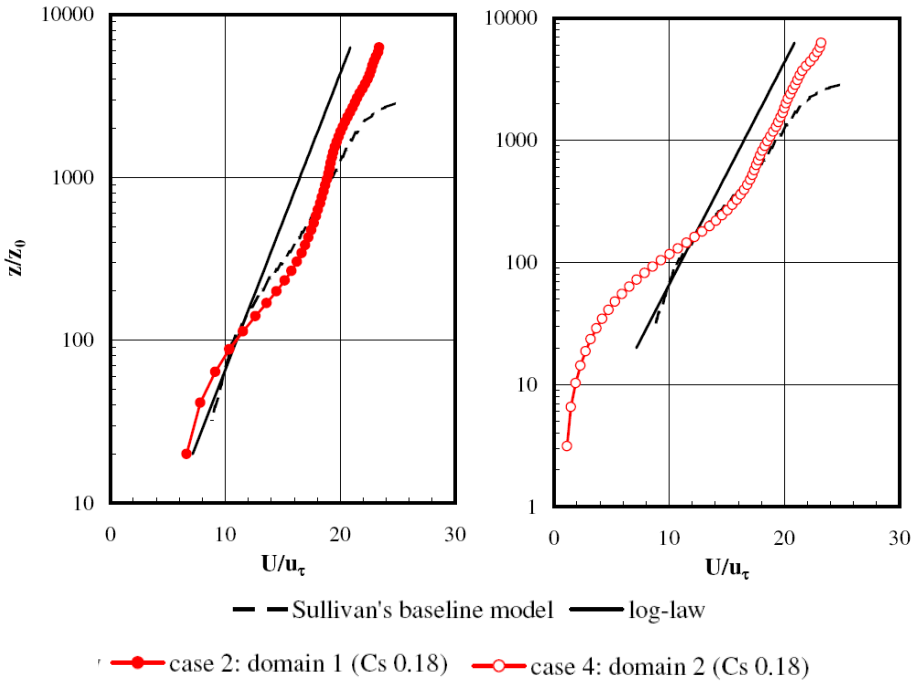

Figure 5.40 – Normalized profiles and comparison with Sullivan's [34] baseline model.

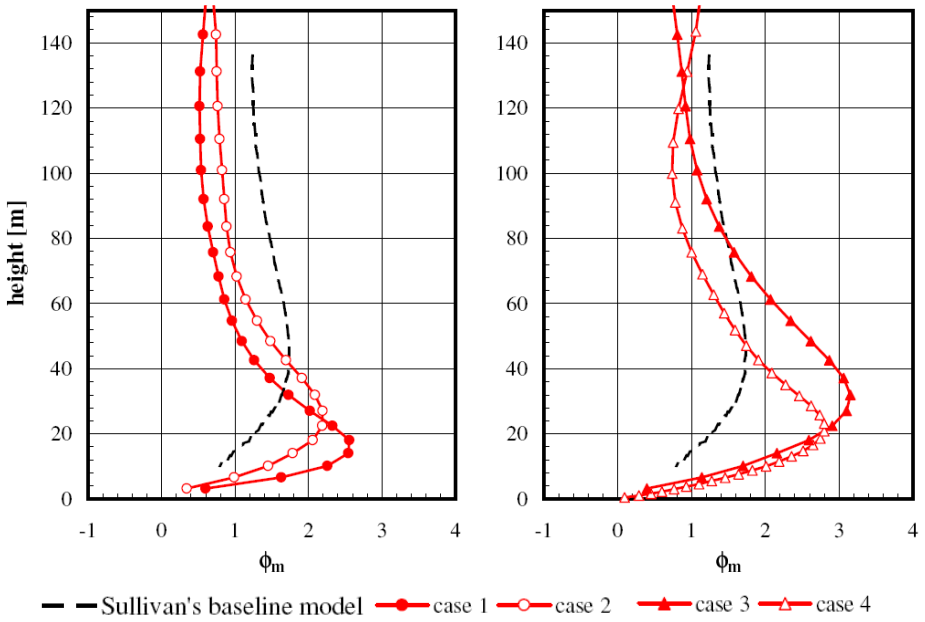

Figure 5.41 - Normalized wind-shear ϕ_m

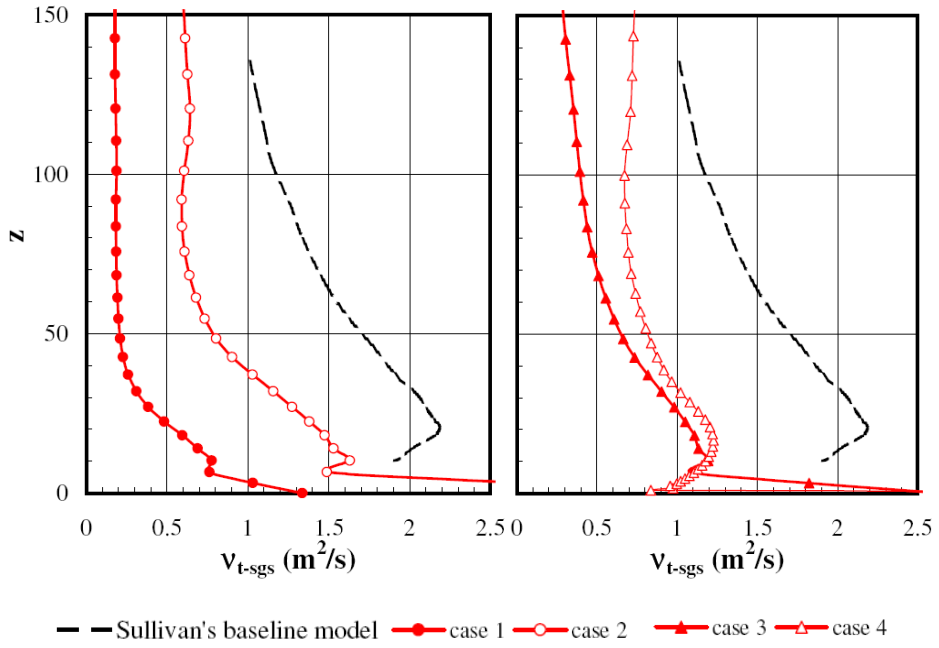

Figure 5.42 – SGS eddy viscosity profiles.

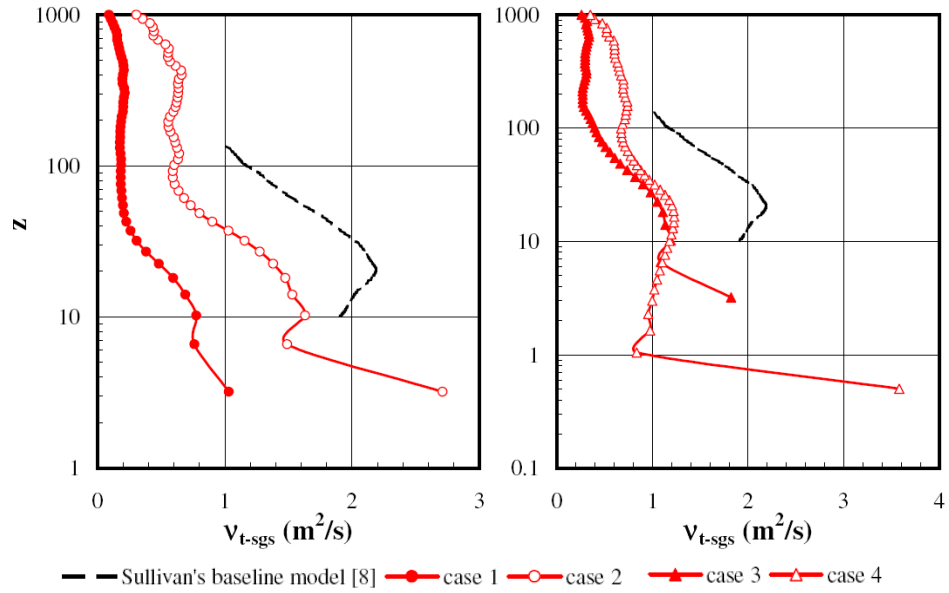

Figure 5.43 – SGS eddy viscosity profiles (lin-log coordinates).

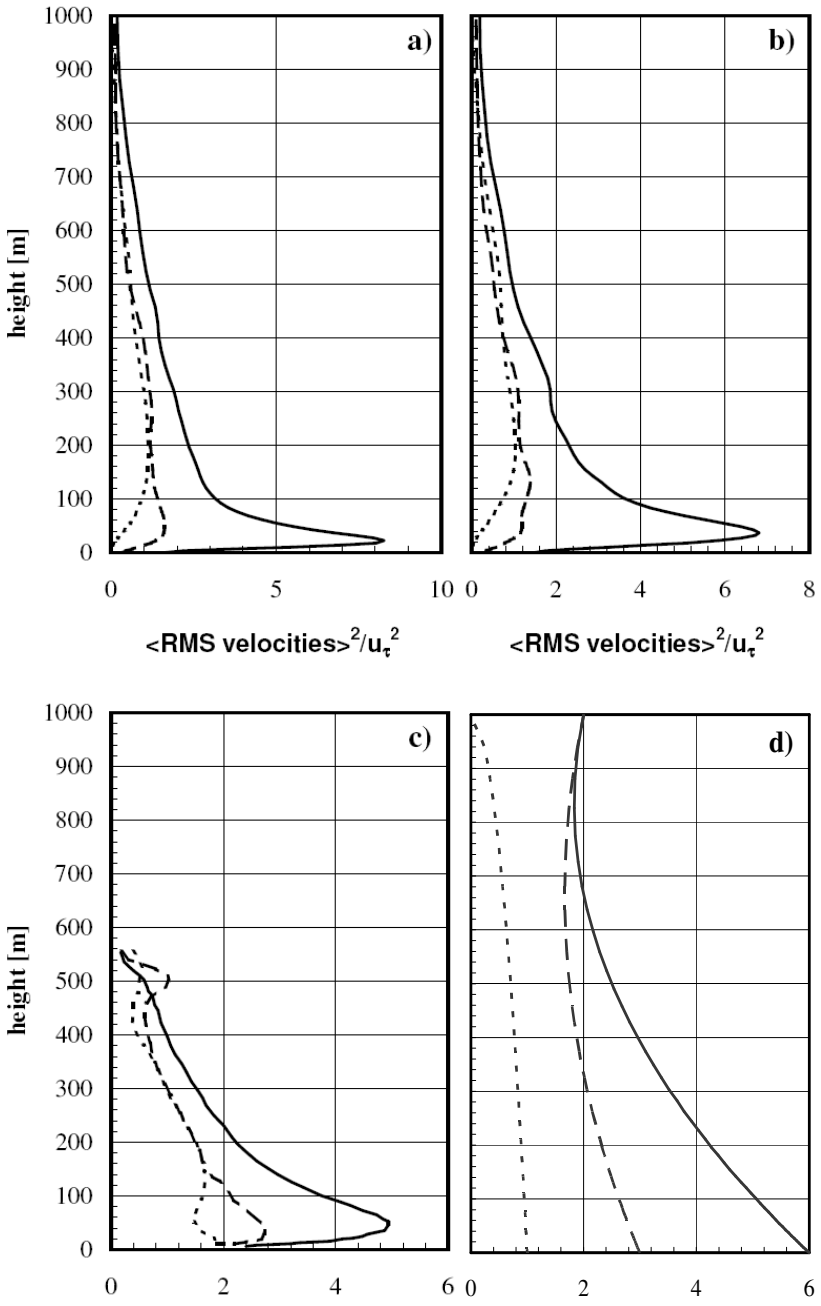

Figure 5.44 – Variances of the velocities normalized with computed friction velocity: solid lines stream-wise component, dashed lines span-wise component, dotted lines vertical component; a) case 1, b) case 2, c) Sullivan's baseline model, d) equations (1.6)-(1.8).

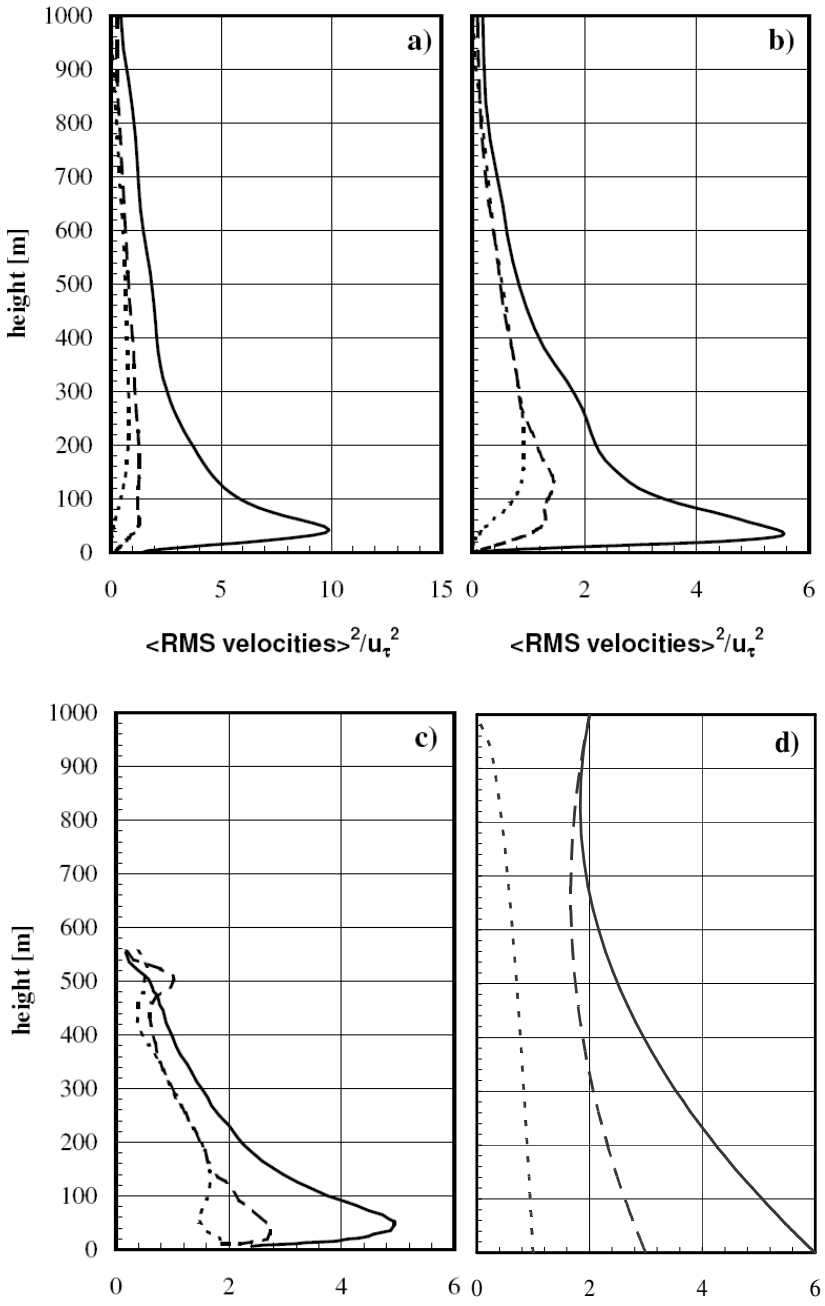

Figure 5.45 – Variances of the velocities normalized with computed friction velocity: solid lines stream-wise component, dashed lines span-wise component, dotted lines vertical component; a) case 3, b) case 4, c) Sullivan's baseline model, d) equations (1.6)-(1.8).

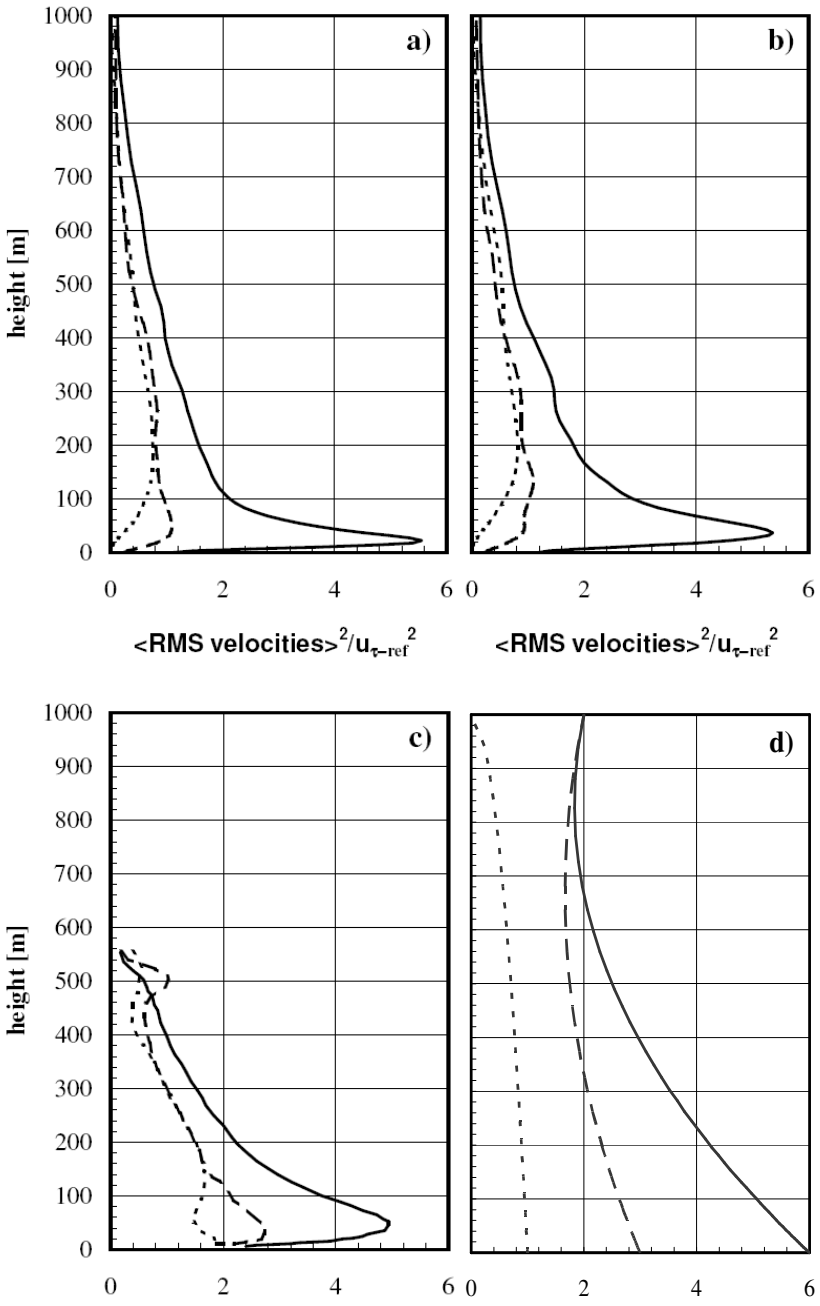

Figure 5.46 – Variances of the velocities normalized with reference friction velocity: solid lines stream-wise component, dashed lines span-wise component, dotted lines vertical component; a) case 1, b) case 2, c) Sullivan's baseline model, d) equations (1.6)-(1.8).

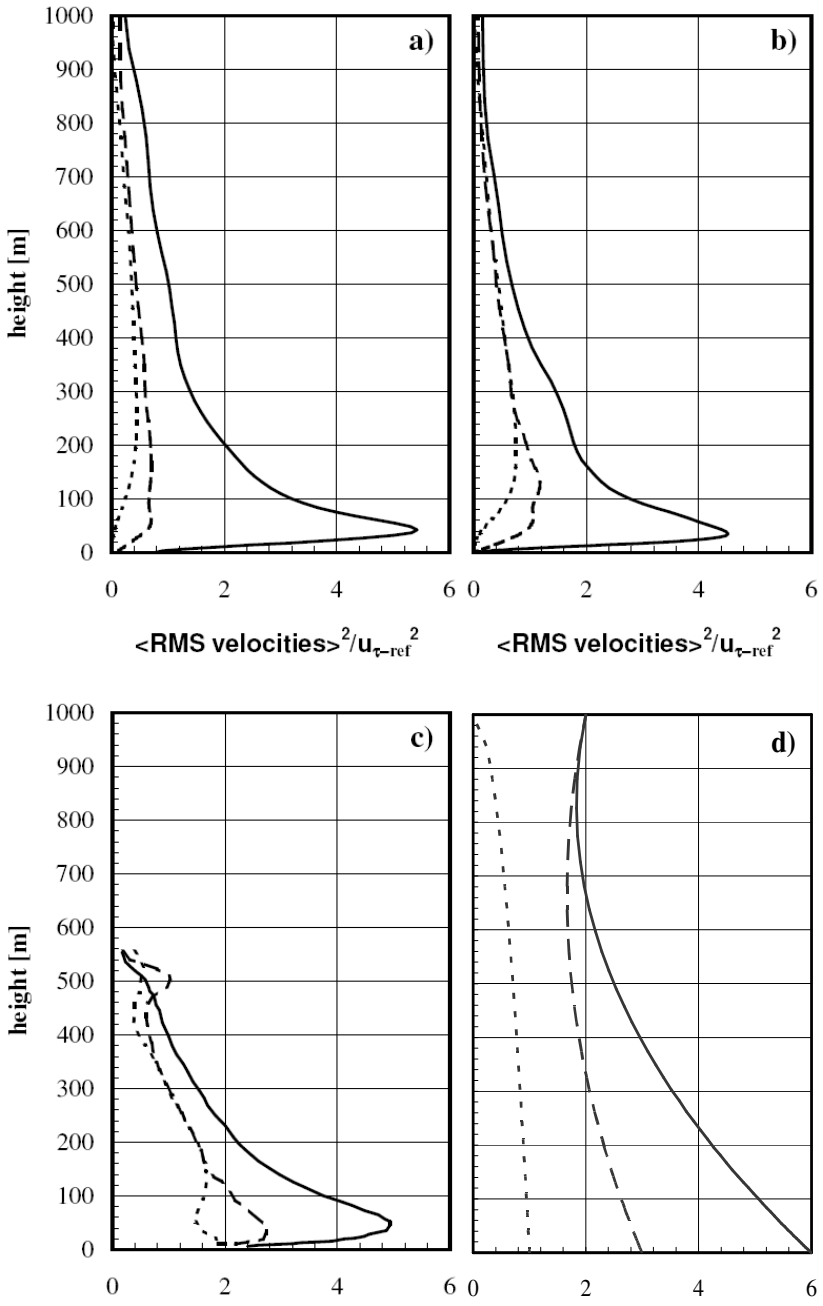

Figure 5.47 – Variances of the velocities normalized with reference friction velocity: solid lines stream-wise component, dashed lines span-wise component, dotted lines vertical component; a) case 3, b) case 4, c) Sullivan's baseline model, d) equations (1.6)-(1.8).

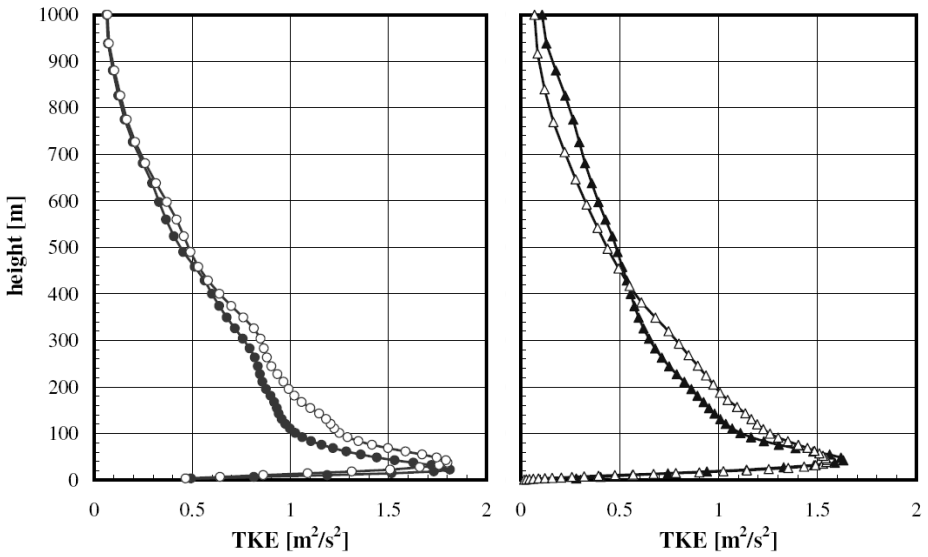

Figure 5.48 – TKE resolved scale vertical profiles.

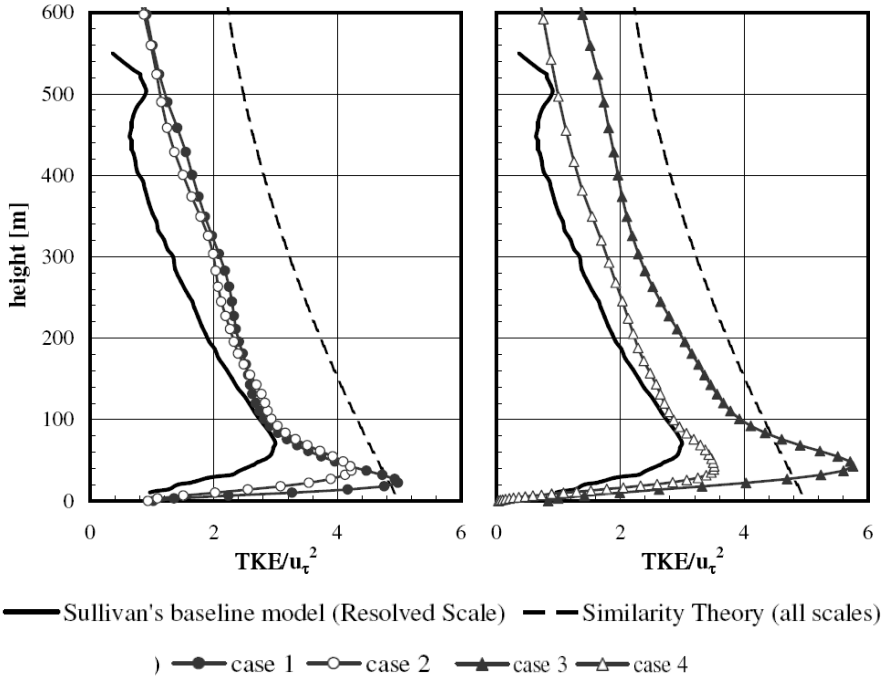

Figure 5.49 – Normalized TKE resolved scale, comparison with baseline model from [34] and similarity theory from definition of TKE (1.9) and equations (1.6)-(1.8).

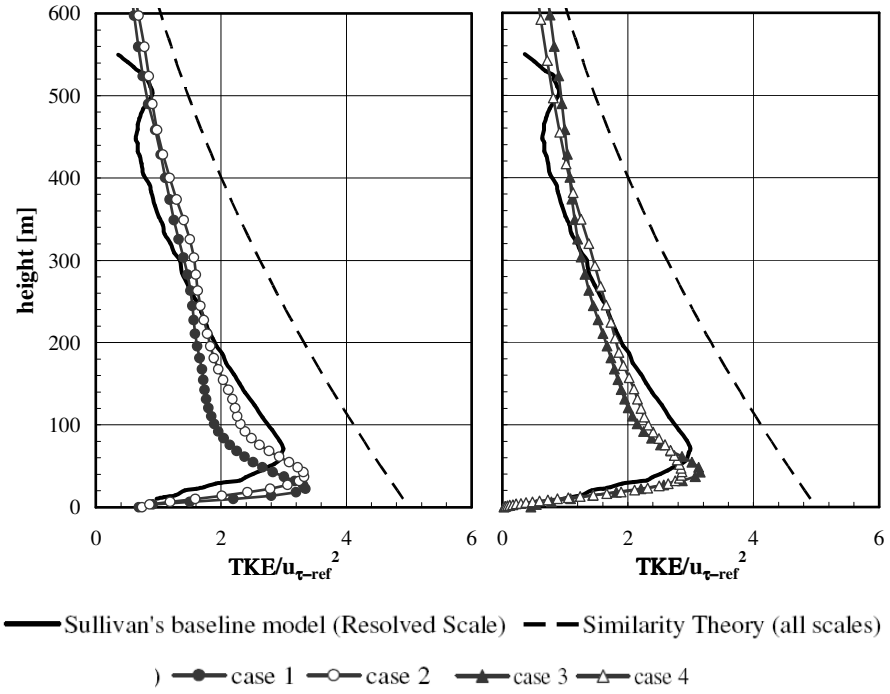

Figure 5.50 – TKE normalized with reference friction velocity (resolved scale), comparison with baseline model from [34] and similarity theory from definition of TKE (1.9) and equations (1.6)-(1.8).

5.7 CONCLUSIONS

The possibility to investigate the ABL flow in neutral stratification with the DES option of the code Fluent 6.2 has been investigated. A setting of parameters which allow a rather acceptable ABL reproduction have been found but further testing is probably required and increasing of the C_{DES} constant, use of discretization schemes different than the first order up-wind for the modified turbulent viscosity have to be tested. Probably, the SA-based DES approach could have some limits in the reproduction of the ABL if no stochastic forcing is implemented. It has to be pointed out that in the newer version of Fluent, the 6.3, two further DES models are available, based on modifications of the k-ε and k-ω, it's worthy also to see how they behave in the reproduction of a neutral ABL.

A new UDF has been implemented which allows the use of the Smagorinsky model coupled with wall-functions, in particular for rough surfaces. The preliminary 3D tests with the new UDF gave results more promising than the ones obtained with the DES approach. In general all the flow-field obtained show an overshoot in the velocity profiles, an underestimation of the wall-shear stress and the presence of super-streaks. All these features bring to think at a stochastic forcing as a possible valid treatment to improve the results of the computations. Moreover, the unnaturally high level of SGS eddy viscosity close to the wall, when the LES-UDF is applied suggests to limit the eddy-viscosity close to the wall, perhaps by choosing the mixing length of the model as the minimum value given by the Smagorinsky model and a value proportional to the wall-distance, i.e. equation (2.27).

A series of future steps have been individuated for the DES/LES analysis of the ABL:

- Use of zonal embedded unstructured grids
- Use of higher order discretization schemes for ν_{sgs} in DES4d
- Implement $Ls=\min(\kappa d;C_s\Delta)$ in the LES-UDF function
- SGS models more advanced than Smagorinsky (WALE, Wong-Lilly, dynamic Smagorinsky, etc.)
- Bigger domains, maybe higher resolution
- Stochastic forcing (synthesized or DNS data), both for DES and WMLES (Wall Modelled LES)
- Simulate the flow (neutral stratification) on a given topography (e.g. Askervein Hill) with DES and WMLES
- Stratification effects, both convective and stratified ABL
- Passive scalar transport, punctual source of scalar (local pollutant source), both for neutral and non-neutral conditions
- Simulate the flow around very complex topographies, (e.g. presence of buildings, steep hills, etc.)
- Introduction of Coriolis force (nesting with meso-scale models)

Chapter 6 FOREST MODELLING WITH WINDSIM

6.1 INTRODUCTION

The roughness of the terrain has be taken into account in CFD simulations by the usage of wall functions, as presented up to this point of the thesis. To apply correctly the wall functions for rough surfaces the centroid of the wall adjacent cells should reside in the surface layer where the logarithmic law is valid, as already introduced in the previous chapters. Hence, when modelling very rough surfaces with wall functions, for instance for values of z_0 higher than 0,1, quite coarse grids have to be drawn. It turns out that for very rough surfaces the flow inside and close to the canopy layer, see the subdivision of the ABL in Figure 1.1, has to be described more accurately and the effects of roughness on the near-wall region cannot only be provided by the boundary conditions. The velocity profile inside a forest canopy is sketched in Figure 6.1.

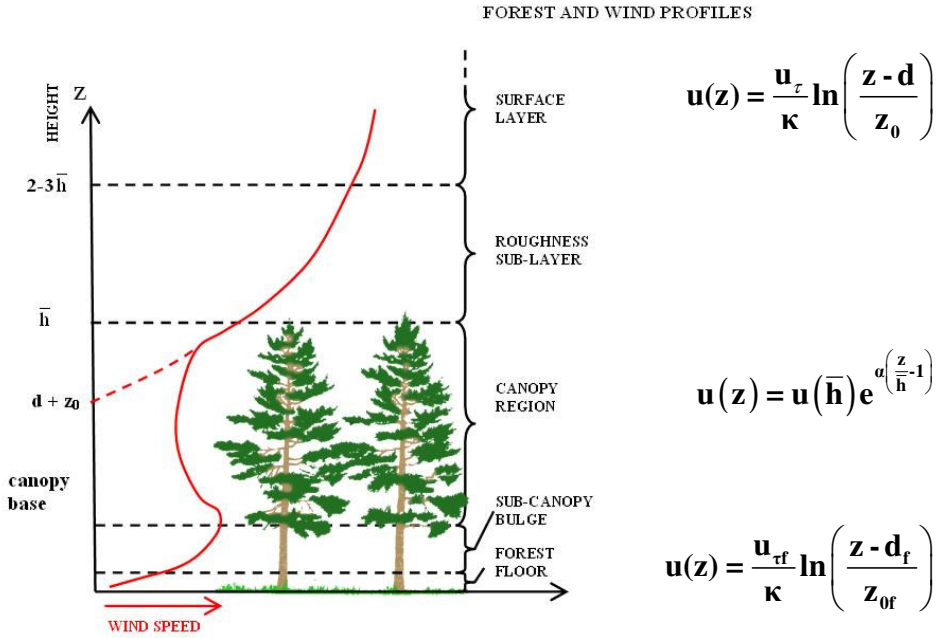

Figure 6.1 – Flow inside and above a forest canopy, wind profiles in the forest sub-regions, graph reconstructed from Gardiner B. (2003) [11].

While the wind profile in the forest floor can be still described with a logarithmic law; in the canopy layer, which is a partially occupied by the fluid, the wind profile diverges from a logarithmic law and re-assumes a logarithmic behaviour only at 2-3 canopy heights, in the surface layer. Trunks, branches and foliage establish a complex system of flexible bodies constituting the forest canopy partially obstructing the flow and extracting momentum from it. Hence a possible modelling could account for the two features: porosity and extraction of momentum from the flow by the canopy itself.

The present chapter deals with the implementation of a canopy model in the CFD code WindSim, a software already introduced in the Chapter 4 which solves the RANS equations by a finite-volume solver named PHOENICS. The studies presented have been partially carried out during the internship of the author at Vector A.S., Tønsberg, Norway, during the period April-June 2005. The development of the canopy model in collaboration with Vector A.S. has continued during the course of the PhD. Part of the results on the canopy model has been already presented in occasion of the WindSim users' meeting in June 2005, while further works have been also presented during the WindSim workshop held in Kassel on the 13th February 2006 and in the poster session at the EWEC 2006 held in Athens, see Gravdahl *et al.* [15].

The versions of the code used during the internship were the 4.4 and the 4.5 and the solver available was of segregated type. Starting from the version 4.6.1 a coupled solver is also available in WindSim, generally less subject to diverge than the segregated one and suggested to be employed when the canopy model is activated. The turbulence is treated with the standard k-ε model with the model's constants that can assume two different sets of values already reported in Table 4.5. All the simulations run with the canopy model were performed with the standard constants of the turbulence model.

The main reason of modelling a forest canopy with numerical tools is motivated by the need of a more precise description of the flow field around wind farms located in the vicinity of areas with high vegetation. When flow simulations When flow simulations over a topography containing woodlands

are needed, the usual approach with wall-functions like the log-law (6.1) for modelling the ABL bears to a poor prediction of wind energy production.

$$u(z) = \frac{u_\tau}{\kappa} \ln\left(\frac{z}{z_0}\right) \qquad \textbf{(6.1)}$$

Therefore the need to model the ABL inside and in the proximity of forest in a more detailed manner. The simplest canopy model could come from the introduction of a displacement length d in the logarithmic law.

$$u(z) = \frac{u_\tau}{\kappa} \ln\left(\frac{z-d}{z_0}\right) \qquad \textbf{(6.2)}$$

The equation (6.2) can be used to describe the ABL over a forested area in the surface layer, above 2-3 canopy heights of altitude, as also sketched in Figure 6.1. A canopy model based on the equation (6.2) is considered in Stangroom (2004) [32] by shifting the wall of a value d and then employing the (6.1) in a CFD model constructed with the finite-volume RANS solver CFX. The concept of the displacement length d is used also in the forest model of the code WAsP and tested for instance by Raftery *et al.* [27] for three validation cases and by using five methodologies to set the parameters d and z_0; their main conclusions were that usually WAsP still describes poorly the flow field around heavy forestry and shows a general tendency to under predict canopy effects, which means an over estimation of the mean terrain velocity.

A more detailed approach in the modelling of a canopy flow can be provided discretizing the canopy with few layers of cells and use sink terms in the momentum RANS equation coupled with a volume porosity in the cells devoted to the canopy flow modelling.

6.2 POROSITY

Two kind of porosities can be set and applied in PHOENICS, and consequently in WindSim, to each cell of a mesh: one concerning the volume of

the cell (β) and a second one concerning the faces (β_S). Both porosities are non-dimensional groups since they describe the fluid fraction of the cell volume or the fluid fraction of the faces bounding the cell.

β – volume occupied by the fluid/volume of the cell (VPOR)
β_S – free area/frontal area of the cell (EPOR, NPOR, HPOR)

For each hexahedral cell of a structured grid four porosities variables can be assigned, one concerning the volume (VPOR) and three concerning areas (EPOR, NPOR, HPOR) bearing in mind that opposite faces have equal porosity β_S.

6.3 MOMENTUM SINKS

The main effect of the porosity variables on the flow is to speed-up the flow passing from a fluid cell to a porous one, in order to satisfy the mass conservation. Therefore, the concept of porosity by itself is not sufficient to describe completely the effects of forestry on wind; consequently the forces exerted by the vegetation on the fluid have to be modelled too, for instance by adding sink terms in the momentum RANS equations (6.3). The sink of momentum in a forest canopy can be modelled by the sum of two terms, one proportional to the velocity and a second one proportional to the square of the velocity as in (6.4). Both equations (6.3) and (6.4) are for unitary porosity.

$$\rho U_i \frac{\partial U_j}{\partial x_i} = \frac{\partial}{\partial x_i}\left[\mu_t \frac{\partial U_j}{\partial x_i}\right] - \frac{\partial P}{\partial x_j} + \rho f_j + S_j \quad \textbf{[N/m}^3\textbf{]} \qquad \textbf{(6.3)}$$

$$S_j = -\rho C1 U_j - \rho C2 \sqrt{U_i U_i}\, U_j \quad \textbf{[N/m}^3\textbf{]} \qquad \textbf{(6.4)}$$

In the case of laminar flow, steady state, negligible advection and diffusion, the source term can be considered only due to molecular viscosity, leading to the Darcy's law which is generally used to model the flow through media with low porosity as the percolation of a fluid through the terrain (a description of

the law is provided in Appendix E). Since the high porosity and the high Reynolds number in the flow inside a forest canopy, the drag forces should be more realistically proportional to the square of the velocity.

6.4 A CANOPY MODEL FOR WINDSIM

A canopy model has been therefore introduced in WindSim. The basic idea of the canopy model is to treat the vegetation (or urban canopy) as a porous media, while sink terms are added in the momentum RANS equation. The canopy forest is completely characterised by the following parameters:

- a ground cover roughness z_{of}
- a volume porosity β
- the height of the canopy h_c ($\overline{h}$ in Figure 6.1)
- two resistive coefficients C1 (1/s) and C2 (m^2/m^3)

The wall functions are therefore still used, and a roughness length still provided, but the z_{of} is now used to describe effect of the forest floor. Hence a logarithmic law as sketched in Figure 6.1 for the forest floor without a displacement length.

$$u(z) = \frac{u_{\tau f}}{\kappa} \ln\left(\frac{z}{z_{0f}}\right) \qquad \textbf{(6.5)}$$

Several layers of cells are meant to model the canopy while the rest of the domain is left to model the flow outside the canopy.

The roughness of the terrain was previously treated in WindSim 4.4 only with the wall functions based on the logarithmic law (6.1), which remains the way to model the roughness of the terrain in those regions where the canopy model is not activated.

The porosity of a forest canopy changes depending on the species of plants, their shape and scatter on the ground, hence the estimation of the porosity of a vegetation canopy is quite difficult and furthermore complicated by the fact that

it changes during seasons and years. An estimation of the porosity of a windbreak can be achieved by optical means, taking black-white pictures of the windbreaks against a bright background; an evaluation of the porosity is therefore obtained by counting the proportion of the white part in the picture.

A list of optical porosities for different species of plants are provided in the Table 6.1 below; they have been estimated by Wei Li and collaborators and published in internet at [41].

In WindSim 4.4 a first approach to solve the flow through a porous media has been achieved by using the both porosities β and β_S and sink terms.

The model is completed with the use of sink terms (drag forces). The total drag force acting on each tree or element of the vegetation can be thought as the sum of two terms, one proportional to the velocity (viscous forces) and a second one proportional to the square of the velocity (pressure forces). As stated in Kaimal and Finnigan (1994) [17] the Reynolds numbers inside a canopy are usually enough high to make dominant the pressure forces and, therefore, a drag force proportional to the square of the velocity can probably describe completely the sink of momentum.

Table 6.1 – Estimations of porosity for several species of trees in winter, from [41]

Specie of tree	**%**
Beech	84
Birch	55
Acacia	40
Mature maple	47
Scots pine	38
Black cherry	77
Lime	54
Ash	48
Spruce	29
Firs	30
Cypresses	15

The canopy model has been firstly tested in 3D simulations for step changes in roughness, from a low roughness area (treated with wall functions) to high roughness (treated with the canopy model) that will be described in the following paragraph.

6.5 WINDSIM SIMULATIONS

The main purpose of the simulations carried out with the code WindSim 4.4 and 4.5 was to test the new canopy model in a sudden change in roughness condition where the inlet zone was set with wall-functions and the rougher with the canopy model. Different approaches were taken into account to solve the canopy layer and compare to experimental and numerical data in literature [17].

A mesh was built for different canopy parameters, a top view of discretised terrain is given in Figure 6.2, the roughness length at the entrance of the domain is 0,03 m, after 2 km from the inlet the flow reaches a vegetation canopy of height as specified in Table 6.3. Hence an internal boundary layer develops starting from the forest edge. A top view of the discretised terrain is shown in Figure 6.2 while dimensions and characteristics of the mesh employed are reported in Table 6.2.

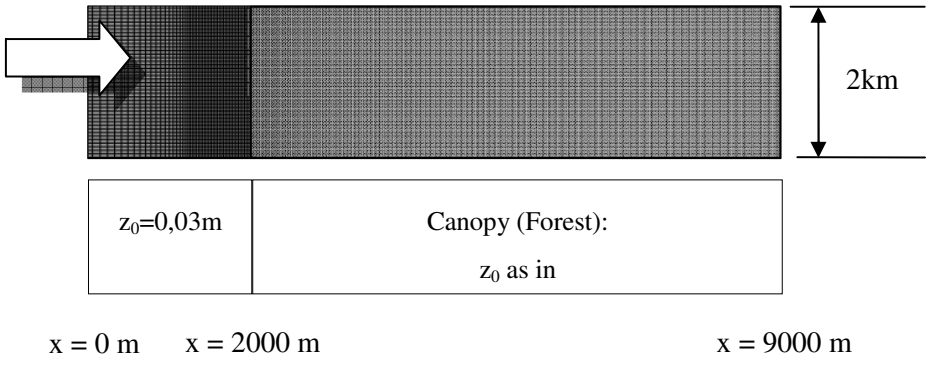

Figure 6.2 – View of the discretised terrain

Table 6.2 – number of cells and dimensions in x (streamwise), y (spanwise) and z (vertical) direction.

Mesh 1		
Nx	**Ny**	**Nz**
117	58	40
Lx	**Ly**	**Lz**
9000 m	2000 m	1000 m

A first series of simulations have been performed with WindSim 4.4. For this version of the code a canopy model was not already available and the whole domain has been meshed vertically with a fixed height distribution factor (HDF), which is the ratio between the height of the wall adjacent cell to the one of the highest cell. The first ten layers of cells starting from the ground and from 2 km from the inlet to the outlet have been used to describe the vegetation canopy.

The simulations run have been named in the following manner:

- Canopy 00: z_0 0,03 m in the whole domain
- Canopy 01: step change in roughness (z_0 0,03 m to 0,6 m) with the logarithmic law
- Canopy 02: canopy model with only porosities
- Canopy 03: canopy model with porosities and drag forces

Table 6.3 – Characteristics of the grids and of the used canopy models with WindSim 4.4.

	Cells in the canopy	**z_{0f}**	**height canopy h_c**	**porosities β and β_S**	**DRAG**
Canopy 00	-	0,03m	-	NO	NO
Canopy 01	-	0,6m	-	NO	NO
Canopy 02	10	0,6m	61,01m	$\beta = 0,5$ $\beta_S = 0,5$	NO
Canopy 03b	10	0,6m	61,01m	$\beta = 0,5$ $\beta_S = 0,5$	C1 =5.965E-5 1/s
Canopy 03c	10	0,6m	61,01m	$\beta = 0,5$ $\beta_S = 0,5$	C1 = 1.0 1/s
Canopy 03e	10	0,6m	61,01m	$\beta = 0,5$ $\beta_S = 0,5$	C1 = 1.0E-02 1/s

For the several used canopy models the most important settings are reported in Table 6.3 and Table 6.4.

Table 6.4 – Same grid's characteristics as in for two further cases (WindSim 4.4).

	Cells in the canopy	**z_{0f}**	**h_c**	**β and β_S**	**DRAG**
Canopy 03f	10	0,6 m	61,01 m	$\beta = 0,5$ $\beta_S = 0,37$	C1 = 0,01 1/s C2 = 0.01 1/m
Canopy 03g	10	0,03 m	61,01 m	$\beta = 0,5$ $\beta_S = 1,0$	C1 = 0,01 1/s

The normalised velocity profile u/u_C is used to compare the numerical results to data. The normalised velocity profile for some experiments are shown in Figure 6.3 together with a normalised momentum flux. The curves are obtained from Kaimal and Finnigan (1994) [17] and from Garratt (1994) [12], and are relative to data from both wind tunnel and real vegetation canopies. Walshe (2004) [40] proposed a canopy model based on resistive forces and the velocity shear and momentum flux profiles obtained by him have been also compared to data extracted from Kaimal and Finnigan (1994) [17] providing good description of the canopy flow, much more precise compared to the pure roughness length model (log-law).

Vertical profiles of velocity are extracted at the point of coordinates x = 7500 m and y = 1000 m where the flow in the canopy is supposed to be fully developed. The normalized velocity profiles obtained are shown in Figure 6.4 for some of the cases run. From the set of simulations run the settings of the Canopy 03f ($\beta = 0,5$; $\beta_S = 0,37$; C1 = 0,01 s^{-1}; C2 = 0,01 m^{-1}) seems to fit better the experimental curves from Bordeaux and Uriarra (pine forest); nevertheless further investigation was needed and this has been done with the newer version of the code, the 4.6.1.

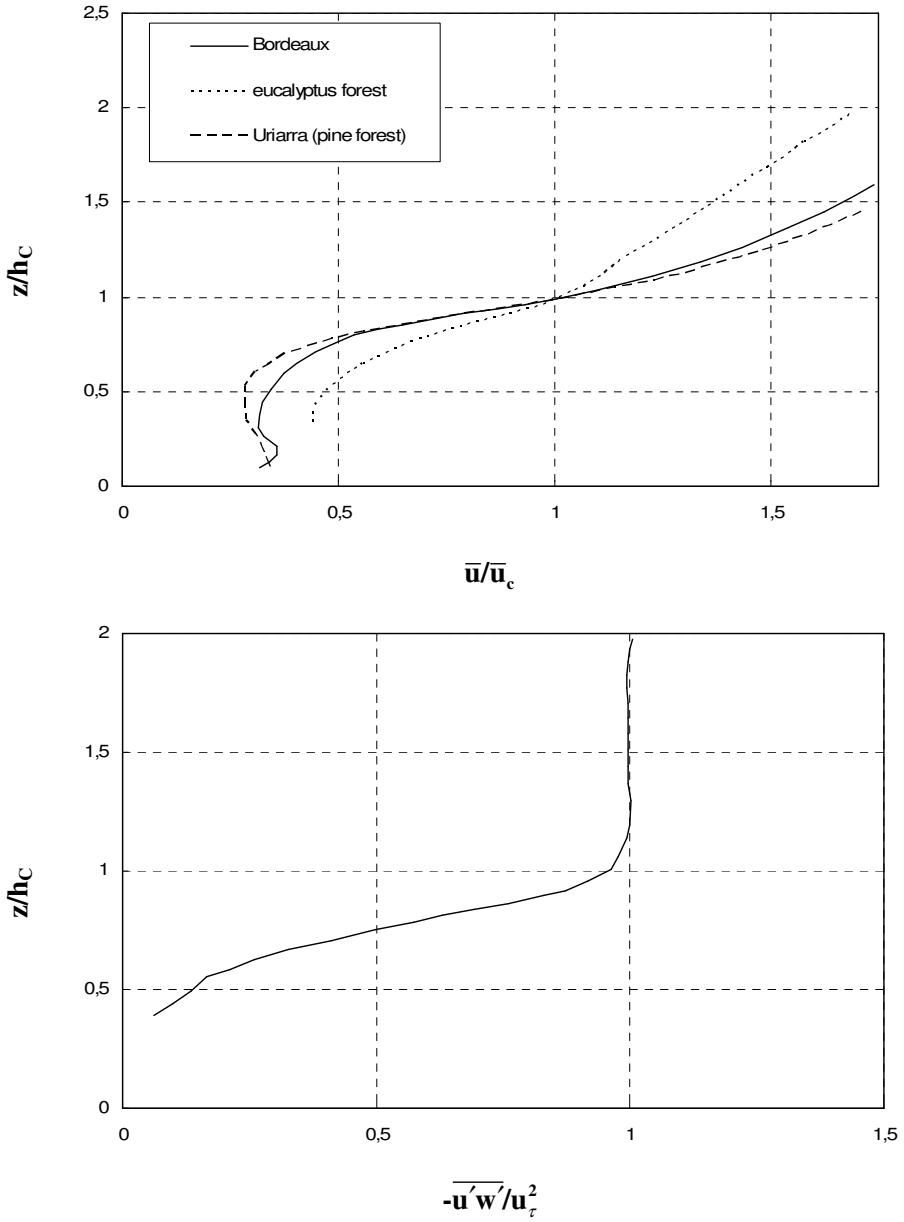

Figure 6.3 – Vertical profiles of normalised wind shear (above) and turbulent momentum flux (below), within and immediately above the canopy for several experiments [17] and [12].

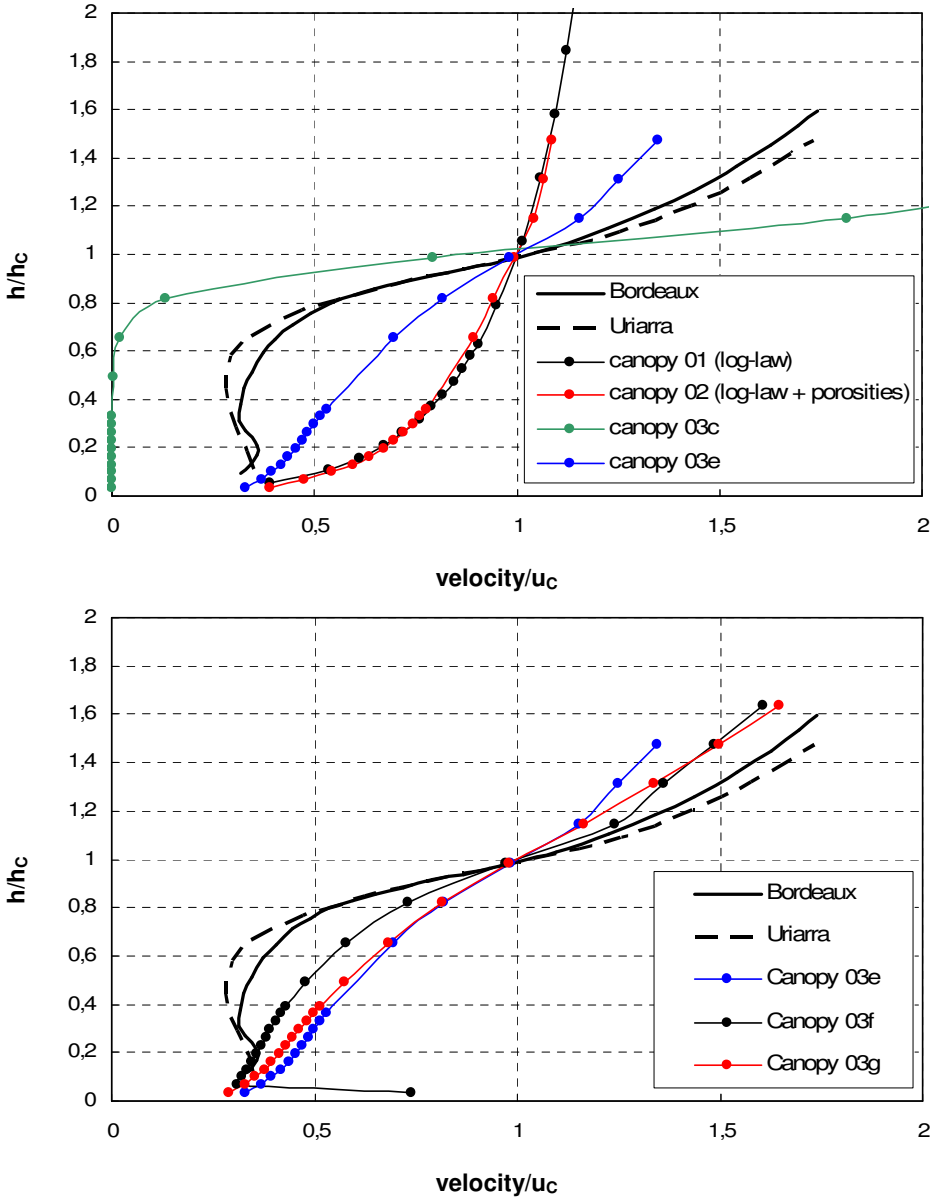

Figure 6.4 – normalised velocity profiles obtained with WindSim 4.4.

The simulations performed with the version 4.6.1 were over a 3D domain, meant to resemble a 2D condition that is not treatable with WindSim. The dimensions of the whole control volume were in fact 0,1 km x 9 km x 1 km, the grid constructed was uniform horizontally and a grading has been set vertically

as also summarised in Table 6.5. The flow condition was still a step change in roughness, the roughness before the forest was set 0,03 m while the forest edge has been placed at 2 km from the inlet.

The settings of the canopy model for some of the simulations performed with the version 4.6 are reported in Table 6.6, whilst in the new version of the code the faces porosities β_S are always left to one. With the new canopy model a layer of porous cells is set at a certain height, for instance 10 m, and the canopy region is discretised vertically in a uniform way while above the canopy the vertical discretization is characterised by a given grading.

The vertical profiles of wind obtained with the most significant simulations of the new series are shown in Figure 6.5 and Figure 6.6; the volume porosity has been set equal to 0,38 in all cases but one since the experimental results named Uriarra are referred to a pine forest (with should have an optical porosity of 38 %). All the reference data have been reported in either Kaimal and Finnigan (1994) [17] and Garratt (1994) [12].

Table 6.5 – number of cells and dimensions in x (streamwise), y (spanwise) and z (vertical) direction.

Mesh 2		
Nx	**Ny**	**Nz**
360	4	35
Lx	**Ly**	**Lz**
9000 m	100 m	1000 m
Δx	**Δy**	**Δz**
25 m	25 m	Variable

Table 6.6 – Grid characteristics of simulations carried out with WindSim 4.6.1.

Cells in the canopy	**z_{0f}**	**h_c**	**β**	**DRAG**
10	0,05 m	10 m	0,50	C1 0,1 1/s
10	0,05 m	10 m	0,38	C1 1,0 1/s
10	0,05 m	10 m	0,38	C1 0,5 1/s
10	0,05 m	10 m	0,38	C1 0,2 1/s
10	0,05 m	10 m	0,38	C1 0,1 1/s
10	0,05 m	10 m	0,38	C1 0,05 1/s
10	0,05 m	10 m	0,38	C2 0,5 1/m
10	0,05 m	10 m	0,38	C2 0,2 1/m
10	0,05 m	10 m	0,38	C2 0,1 1/m
10	0,05 m	10 m	0,38	C2 0,05 1/m

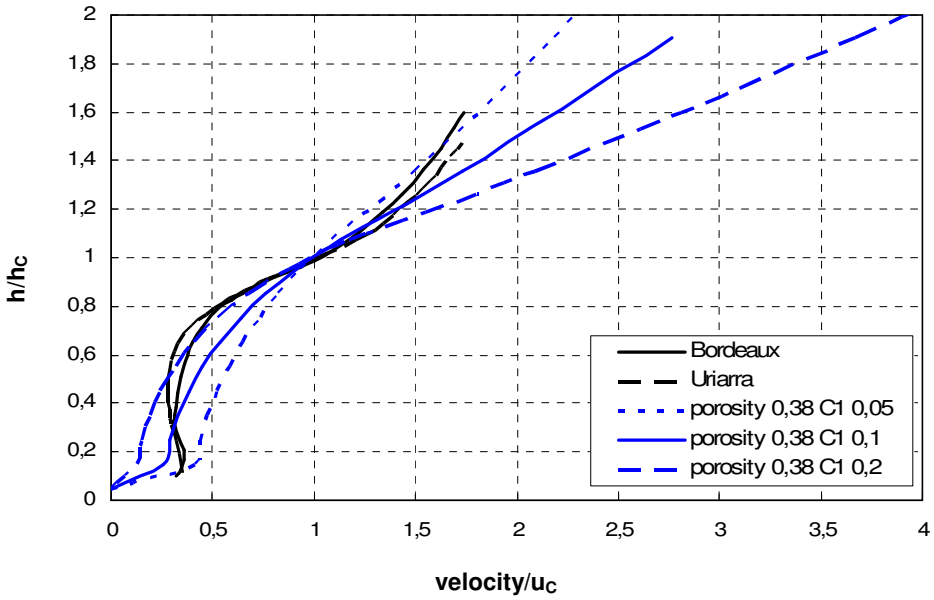

Figure 6.5 – Vertical profiles of wind shear for three cases run with mesh 2 of Table 6.5. (porosity and C1).

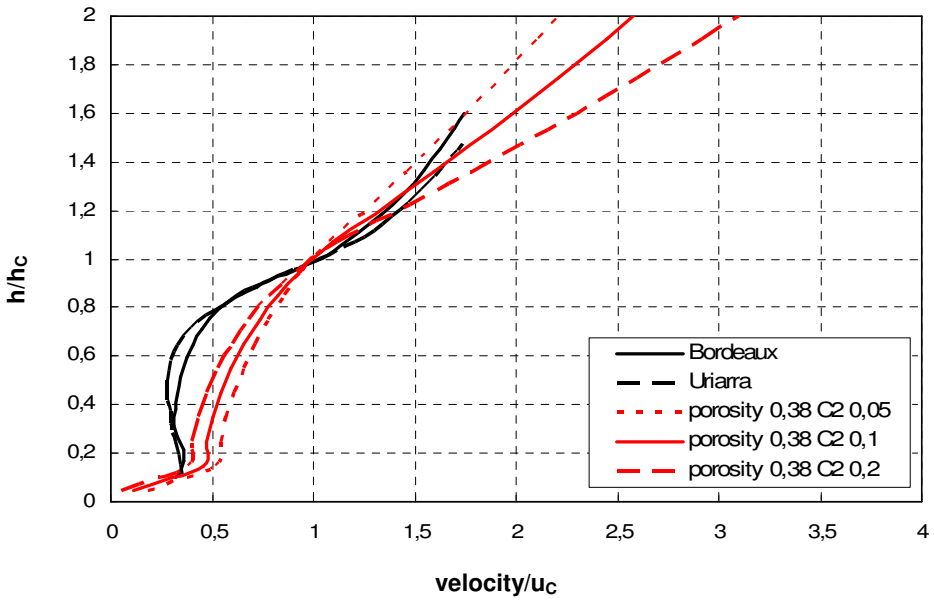

Figure 6.6 – Vertical profiles of wind shear for three cases run with mesh 2 of Table 6.5. (porosity and C2).

If the simulations with porosity 0,38, C1 0,05 1/s and C2 zero is considered acceptable for simulating a pine forest then a set of values of C1 and β are calculated (the followed procedure is presented in Appendix E) and proposed in Table 6.7 for the same species of trees in Table 6.1. The values of C1 and β needs of course to be validated but they provide a good starting point over which refine the settings of the canopy model.

If the constant C2 is whished to be used instead of the C1 it should be noted that a constant C2 almost providing the same effect of a C1 is the one which gives the same drag force; therefore a method to estimate the equivalent C2 constant is to compute the sink term S = C1 U using for U the velocity at $h_C/2$ and imposing the equivalence to S = C2 U^2.

Table 6.7 – Drag coefficient C1estimated for the values of porosity given in Table 6.1 starting from the value for porosity 0,38 used in the computations

Species of tree	**optical porosity (%)**	**C1 (1/s)**
Beech	84	0,008
Black cherry	77	0,012
Birch	55	0,028
Lime	54	0,029
	50	0,033
Ash	48	0,036
Mature maple	47	0,037
Acacia	40	0,047
Scots pine	*38*	*0,050*
Firs	30	0,067
Spruce	29	0,070
Cypresses	15	0,145

CONCLUSIONS

In the course of the present Ph.D. an analysis of the Atmospheric Boundary Layer (ABL) has been carried out with CFD commercial codes. Two different codes have been employed, i.e. Fluent and WindSim, both based on a finite volume solver. The ABL has been always considered with negligible thermal effects, in neutral stability conditions.

The main interest in investigating the ABL with CFD codes resides in the assessment of wind energy by more accurate numerical tools than commonly used. It is worthy to note that different applications may benefit from CFD studies on the ABL, as the assessment of pollutants dispersion, wind loads on structures and pedestrian comfort, just to mention few of them.

The first part of the work has been devoted to the applications of RANS approach to the ABL simulations. Firstly 2D simulations over flat terrains and an isolated 2D bump provided a full set of parameters to be used in the 3D simulations for every kind of terrain roughness. The correct horizontal and vertical resolution and the best discretization schemes were chosen. Secondly, steady RANS 3D simulations over an isolated hill (test case of Askervein) were carried out, allowing a comparison of the result with experimental data. The flow around the hill of Askervein is quite challenging since the difficulties in reproducing the lee side region, in adverse pressure gradient conditions, with flow separation likely to occur.

The object of this part of the work was mainly to test different turbulence models and different set of models' constants. The results showed that turbulence models behave differently in reproducing various aspects of the flow. The k-ε turbulence model, in its RNG version, provided the more correct estimation of the velocity profiles compared to standard and realizable version results. On the contrary, The standard and realizable k-ε models predict better the turbulence level, even if the peak of turbulence that is present in the lee side of the hill is always under predicted.

The RSM model gave generally better predictions of the flow field in most of the simulations, both in terms of velocity and turbulence, with the drawback of a need for bigger computational resources. The differences with k-ε models are enhanced especially in the lee zone of the hill.

A grid refinement study has been conducted showing the strong dependence of the results on the correct grid spacing both in the vertical direction and in the flow direction. It has been shown that finer grid determine better results with a computational effort to be afforded only by parallel processing.

The not very positive results obtained by using the RANS equation are probably due to the possibility that important unsteady phenomena are present in the flow over the Askervein hill, like intermittent separation in the lee side. This could result in a unsteady turbulence that can be only approximately predicted by steady RANS simulations.

In order to overcome the difficulties found with RANS simulations, more sophisticated and challenging methodologies of turbulence treatment have been analysed. The DES and WMLES techniques have been tested on rough flat terrains with the code Fluent 6.2. In particular, since the WMLES was not available in the code, a User-Defined-Function (UDF) has been implemented, where the Smagorinsky-Lilly model is coupled with wall functions for rough surfaces. This LES-UDF (WMLES) model shows better results then those obtained with the SA based DES for a neutral ABL over flat terrains. Still an overshoot in the wind velocity profile is present, which diverges from the logarithmic law. Some trial for grid sensitivity and results from the literature, show that this defect can be cured by further refinement of the grid, i.e. reducing the filter width, and/or with a SGS modelling more advanced than the standard Smagorinsky.

In the framework of assess the capabilities of CFD codes to evaluate the wind energy resources on real sites, a new canopy model has been proposed and tested for the code WindSim. A canopy model was needed to simulate the effects of forestry on the ABL flow. This new approach is based on the usage of porous cells and sink terms in the RANS equations and has been tested in a step

change in roughness over a flat terrain. Results show a good agreement with experimental data, allowing to propose a series of setting parameters for different types of woodlands and providing guidelines for forest modelling.

REFERENCES

[1] **Anderson J.D., Degrez G., Dick E., Grundmann R. (1995).** *Computational Fluid Dynamics*, John Wendt F. (Editor). Springer

[2] **Bardina, J., Ferziger, J. H. & Reynolds, W. C. (1983).** *Improved turbulence models based on large eddy simulation of homogeneous, incompressible, turbulent flows.* Technical Report TF-19. Department of Mechanical Engineering, Stanford University, Stanford, California

[3] **Beljaars A.C.M., Walmsley J.L., Taylor P.A. (1987).** *A mixed spectral finite-difference model for neutrally stratified boundary-layer flow over roughness changes and topography.* Boundary Layer Meteorology, vol. 38, pp. 273-303

[4] **BWEA**. Workshop on the influence of trees on wind farm energy yield. Technical report, BWEA-British Wind Energy Association, 2004. Workshop held at The Arthouse Hotel (Glasgow, Scotland), 17th March 2004. http://www.bwea.com/planning/trees.html

[5] **Castro F.A., Palma J.M.L.M., Lopes Silvia A. (2003).** *Simulation of the Askervein flow. Part 1: Reynolds averaged Navier-Stokes equations (k-ε turbulence model).* Boundary-Layer Meteorology, vol 107, pp. 501-530

[6] **Cebeci T. and Bradshaw. P. (1977).** *Momentum Transfer in Boundary Layers. Hemisphere.* Publishing Corporation, New York.

[7] **Chow F. K. (2004).** *Subfilter-scale turbulence modelling for large-eddy simulation of atmospheric boundary layer over complex terrain.* Ph.D. Thesis, Stanford University.

[8] **Crasto G., Cambuli F., Mandas N., Cau G. (2004).** *Simulazione numerica degli effetti fluidodinamica di una collina artificiale per la protezione di un parco carbone.* Proceedings of the 59th ATI Congress. (in Italian)

[9] **Crasto G. (2006).** *Investigation of the atmospheric boundary layer applying large eddy simulation.* Diploma Course 2005-06 final project's thesis, von Karman institute for fluid dynamics, Belgium.

[10] Fluent 6.2 User's Guide

[11] **Gardiner B. (2003).** *Airflow Over Forests and Forest Gaps.* Presentation at the workshop BWEA [4]

[12] **Garratt J.R. (1994).** *The atmospheric boundary layer.* Cambridge atmospheric and space science series.

[13] **Germano, M., Piomelli, U., Moin, P. & Cabot, W. H. (1991).** *A dynamic subgrid-scale eddy viscosity model.* Physics of Fluids 3 (7), pp. 1760-1765

[14] **Grant, A.L.M..** *Observations of boundary layer structure made during the 1981 KONTUR experiment.* Quart. J. Roy. Meteor. Soc., Vol. 112, pp 825-841.

[15] **Gravdahl A.R., Crasto G., Quinn S., Mandas N., Cambuli F. (2006).** *Canopy modelling with a CFD code.* EWEC, Athens, 2006.
pdf document at:
http://www.windsim.com/documentation/papers_presentations/main.html

[16] **Guénot D., Aupoix B. (2003).** *Etude de l'approche DES (Detached Eddy Simulation) pour prévoir les écoulements instationnaires à grande échelle.* 16eme Congrès Français de Mécanique, Nice, 1-5 September 2003.

[17] **Kaimal J.C., Finnigan J.J. (1994).** *Atmospheric boundary layer flows: Their structure and measurement.* Oxford University Press, New York, NY.

[18] **Kim H.G., Lee C.M., Lim H.C., Kyong N.H. (1997).** *An experimental and numerical study on the flow over two-dimensional hills.* Journal of Wind Engineering and Industrial Aerodynamics, vol. 66, pp. 17-33

[19] **Kim S.E. (2004).** *Large eddy simulation using unstructured meshes and dynamic subgridscale turbulence models.* Technical Report AIAA-2004-2548, American Institute of Aeronautics and Astronautics, 34th Fluid Dynamics Conference and Exhibit.

[20] **Kraichnan R. (1970).** *Diffusion by a Random Velocity Field.* Physics of Fluids, vol. 11, pp. 21-31.

[21] **Leroy J. (1999).** *Wind field simulations at Askervein Hill.* Technical Report, Vector CFD Consulting.

[22] **Lilly (1992).** *A proposed modification of the Germano subgrid-scale closure method.* Physics of Fluids 4 (3), pp. 633-635.

[23] **Mandas N., Cambuli F., Crasto G., Cau G. (2004).** *Numerical simulation of the Atmospheric Boundary Layer (ABL) over complex terrains.* EWEC 2004, London, November 2004.

[24] **Mason P.J. and Thompson D.J. (1987).** *Large-eddy simulations of the neutral-static-stability planetary boundary layer.* Quart. J. Roy. Meteor. Soc., Vol. 113, pp 413-443.

[25] **Mason P.J., Thomson D.J. (1992).** *Stochastic backscatter in large-eddy simulations of boundary layers.* Journal of Fluid Mechanics, vol. 242, pp 51-78.

[26] **Piomelli U., Balaras E., Pasinato H., Squires K.D. and Spalart P.R. (2003).** *The inner-outer layer interface in large-eddy simulations with wall-layer models.* Int. J. Heat Fluid Flow, vol. 24, pp. 538-550.

[27] **Raftery P., LeBlanc M., Manning J. (2004).** *WAsP Validation Study of Forestry Effects.* Presented at the Workshop [1].

[28] **Shur M., Spalart P. R., Strelets M. and A. Travin (1999).** *Detached-Eddy Simulation of an Airfoil at High Angle of Attack.* In 4th Int. Symposium on Eng. Turb. Modeling and Experiments, Corsica, France.

[29] **Smagorinsky J. (1963).** *General circulation experiments with the primitive equations.* Monthly Weather Review, vol. 91, pp. 99-152.

[30] **Smirnov R., Shi S., and Celik I. (2001).** *Random Flow Generation Technique for Large Eddy Simulations and Particle-Dynamics Modeling.* Journal of Fluids Engineering, vol. 123, pp. 359-371.

[31] **Spalart P.R., Jou W-H, Strelets M., Allmaras S.R. (1997).** *Comments on the feasibility of LES for wings, and on hybrid RANS/LES approach.* 1st AFSOR International Conference on DNS/LES, Aug. 4-8 1997, Ruston.

[32] **Stangroom P. (2004).** *CFD Modelling of Wind Flow Over Terrain***.** Civil Engineering. Nottingham, University of Nottingham

[33] **Stull R.B. (1988).** *An Introduction to Boundary Layer Meteorology.* Kluwer Accademic Publisher

[34] **Sullivan P.P., Mc Williams J.C., Moeng Chin-Hoh (1994).** *A subgrid-scale model for Large-Eddy simulation of planetary boundary-layer flows.* Boundary-Layer Meteorology, Vol. 71, 1994, pp 247-276.

[35] **Taylor P.A., Teunissen H.W. (1983).** *ASKERVEIN 82: Report on the September/October 1982 Experiment to Study Boundary-Layer Flow Over Askervein, South Uist***.** Research Report MSRB-83-8, Atmospheric Environment Service, Downsview, Ontario, Canada

[36] **Taylor P.A., Teunissen H.W. (1985).** *The Askervein Hill Project: Report on September/October 1983 Main Field Experiment***.** Internal Rep. MSRB-84-6, Atmospheric Environment Service, Downsview, Ontario, Canada

[37] **Taylor P.A., Teunissen H.W. (1986).** ***The Askervein Project:*** *overview and background data***.** Boundary Layer Meteorology, vol. 39, pp. 15-39

[38] **Tennekes, H. (1982):** *Similarity relations, scaling laws and spectral dynamics.* Atmospheric Turbulence and Air Pollution Modeling (F.T.M. Nieuwstadt and H. van Dop, Eds.).Reidel, Hingham, MA, pp. 37-68

[39] **Troen I., Lundtang Petersen E. (1989).** *European Wind Atlas***.** Risø National Laboratory, Denmark.

[40] **Walshe J. (2004).** *Effects of Forestry – A CFD resistive volume model.* POWERGEN Power Technology Center.

[41] **Wei Li, Fan Wang, Simon Bell.** http://www.sbe.hw.ac.uk/research/buildingeng/wind_modelling/gui_windbk.html

[42] **Wong V. C., Lilly D. K. (1994).** *A comparison of two dynamic subgrid closure methods for turbulent thermal-convection.* Physics of Fluids 6 (2), pp. 1016-1023.

[43] **Zang, Y., Street, R. L., Koseff, J. R. (1993).** *A dynamic mixed subgrid-scale model and its application to turbulent recirculating flows.* Physics of Fluids 5 (12), pp. 3186-3196.

APPENDIX A. MODIFICATION OF SKE MODEL'S CONSTANTS.

The constant C_μ is computed taking into account measures of turbulent kinetic energy at a given height, in conditions of neutral stratification and fully developed boundary layer the vertical profile of TKE can be described by equation (3.2) considering the height of the ABL equals to the eight of the domain, for instance 1000 m.

If k_{10} is the TKE measured at 10 m height than is C_μ is given by:

$$C_\mu = \frac{u_\tau^4}{k_{10}^2}\left[1-\left(\frac{10\,m}{\delta_{ABL}}\right)\right]^4$$

Given the transport equation for k:

$$\frac{\partial}{\partial t}(\rho k)+\frac{\partial}{\partial x_i}(\rho k u_i)=\frac{\partial}{\partial x_i}\left(\left(\mu+\frac{\mu_t}{\sigma_k}\right)\frac{\partial k}{\partial x_i}\right)+\mathrm{G}_k-\rho\varepsilon$$

For a steady flow:

$$\frac{\partial}{\partial x_i}(\rho k u_i)=\frac{\partial}{\partial x_i}\left(\left(\mu+\frac{\mu_t}{\sigma_k}\right)\frac{\partial k}{\partial x_i}\right)+\mathrm{G}_k-\rho\varepsilon$$

And fully developed flow (2D):

$$0=\frac{\partial}{\partial y}\left(\left(\mu+\frac{\mu_t}{\sigma_k}\right)\frac{\partial k}{\partial y}\right)+\mathrm{G}_k-\rho\varepsilon$$

$$0=\frac{\partial}{\partial y}\left(\mu\frac{\partial k}{\partial y}\right)+\frac{\partial}{\partial y}\left(\frac{\mu_t}{\sigma_k}\frac{\partial k}{\partial y}\right)+\mathrm{G}_k-\rho\varepsilon$$

$$0=\mu\frac{\partial^2 k}{\partial y^2}+\frac{1}{\sigma_k}\frac{\partial}{\partial y}\left(\mu_t\frac{\partial k}{\partial y}\right)+\mathrm{G}_k-\rho\varepsilon$$

$$\frac{\mu_t}{\sigma_k}>>\mu \text{ implies } 0=\frac{1}{\sigma_k}\frac{\partial}{\partial y}\left(\mu_t\frac{\partial k}{\partial y}\right)+\mathrm{G}_k-\rho\varepsilon$$

And since the first term of the RHS of the equation is negligible compared to both the destruction and production terms it follows $\mathrm{G}_k=\rho\varepsilon$.

Transport equation for ε:

$$\frac{\partial}{\partial t}(\rho\varepsilon)+\frac{\partial}{\partial x_i}(\rho\varepsilon u_i)=\frac{\partial}{\partial x_i}\left(\left(\mu+\frac{\mu_t}{\sigma_\varepsilon}\right)\frac{\partial\varepsilon}{\partial x_i}\right)+C_{1\varepsilon}\mathrm{G}_k\frac{\varepsilon}{k}-C_{2\varepsilon}\rho\frac{\varepsilon^2}{k}$$

For steady flow:

$$\frac{\partial}{\partial x_i}(\rho\varepsilon u_i)=\frac{\partial}{\partial x_i}\left(\left(\mu+\frac{\mu_t}{\sigma_\varepsilon}\right)\frac{\partial\varepsilon}{\partial x_i}\right)+C_{1\varepsilon}\mathrm{G}_k\frac{\varepsilon}{k}-C_{2\varepsilon}\rho\frac{\varepsilon^2}{k}$$

Fully developed boundary layer:

$$0=\frac{\partial}{\partial y}\left(\left(\mu+\frac{\mu_t}{\sigma_\varepsilon}\right)\frac{\partial\varepsilon}{\partial y}\right)+C_{1\varepsilon}\mathrm{G}_k\frac{\varepsilon}{k}-C_{2\varepsilon}\rho\frac{\varepsilon^2}{k}$$

$$\frac{\mu_t}{\sigma_\varepsilon}>>\mu\quad 0=\frac{\partial}{\partial y}\left(\frac{\mu_t}{\sigma_\varepsilon}\frac{\partial\varepsilon}{\partial y}\right)+C_{1\varepsilon}\mathrm{G}_k\frac{\varepsilon}{k}-C_{2\varepsilon}\rho\frac{\varepsilon^2}{k}$$

The eddy viscosity with the algebraic equation $\mu_t=\rho C_\mu\frac{k^2}{\varepsilon}$ that can be substituted in the transport equation for the TDR:

$$0=\frac{\partial}{\partial y}\left(\frac{\rho C_\mu k^2}{\sigma_\varepsilon\varepsilon}\frac{\partial\varepsilon}{\partial y}\right)+C_{1\varepsilon}\mathrm{G}_k\frac{\varepsilon}{k}-C_{2\varepsilon}\rho\frac{\varepsilon^2}{k}$$

$$0=\frac{\rho C_\mu k^2}{\sigma_\varepsilon}\frac{\partial}{\partial y}\left(\frac{1}{\varepsilon}\frac{\partial\varepsilon}{\partial y}\right)+C_{1\varepsilon}\mathrm{G}_k\frac{\varepsilon}{k}-C_{2\varepsilon}\rho\frac{\varepsilon^2}{k}$$

And considering the previous equilibrium hypothesis $\mathrm{G}_k=\rho\varepsilon$:

$$0=\frac{\rho C_\mu k^2}{\sigma_\varepsilon}\frac{\partial}{\partial y}\left(\frac{1}{\varepsilon}\frac{\partial\varepsilon}{\partial y}\right)+C_{1\varepsilon}\rho\frac{\varepsilon^2}{k}-C_{2\varepsilon}\rho\frac{\varepsilon^2}{k}$$

$$(C_{2\varepsilon}-C_{1\varepsilon})\rho\frac{\varepsilon^2}{k}=\frac{\rho C_\mu k^2}{\sigma_\varepsilon}\frac{\partial}{\partial y}\left(\frac{1}{\varepsilon}\frac{\partial\varepsilon}{\partial y}\right)$$

$$(C_{2\varepsilon}-C_{1\varepsilon})\frac{\varepsilon^2}{k}=\frac{C_\mu k^2}{\sigma_\varepsilon}\frac{\partial}{\partial y}\left(\frac{1}{\varepsilon}\frac{\partial\varepsilon}{\partial y}\right)$$

$$\frac{\partial}{\partial y}\left(\frac{1}{\varepsilon}\frac{\partial\varepsilon}{\partial y}\right)=-\frac{1}{\varepsilon^2}\left(\frac{\partial\varepsilon}{\partial y}\right)^2+\frac{1}{\varepsilon}\frac{\partial^2\varepsilon}{\partial y^2}$$

Considering the TDR inversely proportional to the wall distance,

$$\varepsilon(y)=\frac{u^{*3}}{\kappa y}$$

$$\frac{\partial\varepsilon(y)}{\partial y}=\frac{u^{*3}}{\kappa}\left(-\frac{1}{y^2}\right)=-\frac{\varepsilon}{y}$$

$$\frac{\partial^2\varepsilon(y)}{\partial y^2}=\frac{u^{*3}}{\kappa}\left(\frac{2}{y^3}\right)=\frac{2\varepsilon}{y^2}$$

hence:

$$\frac{\partial}{\partial y}\left(\frac{1}{\varepsilon}\frac{\partial\varepsilon}{\partial y}\right)=-\frac{1}{\varepsilon^2}\left(\frac{\partial\varepsilon}{\partial y}\right)^2+\frac{1}{\varepsilon}\frac{\partial^2\varepsilon}{\partial y^2}=-\frac{1}{\varepsilon^2}\left(-\frac{\varepsilon}{y}\right)^2+\frac{1}{\varepsilon}\frac{2\varepsilon}{y^2}=-\frac{1}{y^2}+\frac{2}{y^2}=\frac{1}{y^2}$$

That can be substituted in the transport equation for TDR,

$$\left(C_{2\varepsilon}-C_{1\varepsilon}\right)\frac{\varepsilon^2}{k}=\frac{C_\mu k^2}{\sigma_\varepsilon}\frac{\partial}{\partial y}\left(\frac{1}{\varepsilon}\frac{\partial\varepsilon}{\partial y}\right)$$

$$\Downarrow$$

$$\left(C_{2\varepsilon}-C_{1\varepsilon}\right)\left(\frac{u^{*3}}{\kappa y}\right)^2=\frac{C_\mu k^3}{\sigma_\varepsilon}\frac{1}{y^2}$$

$$\left(C_{2\varepsilon}-C_{1\varepsilon}\right)\frac{u^{*6}}{\kappa^2}=\frac{C_\mu k^3}{\sigma_\varepsilon}$$

In proximity of walls the TKE is given by $k=\frac{u^{*2}}{\sqrt{C_\mu}}$ which leads to:

$$\left(C_{2\varepsilon}-C_{1\varepsilon}\right)\frac{u^{*6}}{\kappa^2}=\frac{C_\mu}{\sigma_\varepsilon}\frac{u^{*6}}{C_\mu^{3/2}}$$

$$\left(C_{2\varepsilon}-C_{1\varepsilon}\right)\frac{1}{\kappa^2}=\frac{1}{\sigma_\varepsilon}\frac{1}{\sqrt{C_\mu}}$$

And finally a relation is found linking the constant Cm the difference $C_{2\varepsilon} - C_{1\varepsilon}$ and the turbulent Prandtl number for TDR.

$$C_{2\varepsilon}-C_{1\varepsilon}=\frac{\kappa^2}{\sqrt{C_\mu}\cdot\sigma_\varepsilon}$$

APPENDIX B. DERIVATION OF FORMULA (2.33).

Let's consider equations (1.3) and (2.32) reported below,

$$\frac{U(z)}{u_\tau} = \frac{1}{\kappa}\ln\left(\frac{z}{z_0}\right) \qquad (1.3)$$

$$u^+ = \frac{1}{\kappa}\ln\left(y^+\right) + B - \Delta B \qquad (2.32)$$

Now, using the definition of wall coordinates and the relation linking E to B,

$u^+ = \frac{u}{u_\tau}$; $y^+ = \frac{\rho\, y\, u_\tau}{\mu}$ Wall coordinates, $B = \frac{1}{\kappa}\ln(E)$ the (2.32) becomes:

$$\frac{u}{u_\tau} = \frac{1}{\kappa}\ln\left(\frac{\rho\, y\, u_\tau}{\mu}\right) + \frac{1}{\kappa}\ln(E) - \Delta B$$

And in fully-rough regime ($K_S^+ > 90$)

$$\frac{u}{u_\tau} = \frac{1}{\kappa}\ln\left(\frac{\rho\, y\, u_\tau}{\mu}\right) + \frac{1}{\kappa}\ln(E) - \frac{1}{\kappa}\ln\left(1 + C_S K_S^+\right)$$

Since the product $C_S K_S^+$ is expected to be much greater than 1 it follows:

$$\frac{u}{u_\tau} \approx \frac{1}{\kappa}\ln\left(\frac{\rho\, y\, u_\tau}{\mu}\right) + \frac{1}{\kappa}\ln(E) - \frac{1}{\kappa}\ln\left(C_S K_S^+\right)$$

$$\frac{u}{u_\tau} \approx \frac{1}{\kappa}\ln\left(\frac{\rho\, y\, u_\tau}{\mu}\right) + \frac{1}{\kappa}\ln(E) - \frac{1}{\kappa}\ln\left(C_S\, \frac{\rho\, K_S\, u_\tau}{\mu}\right)$$

$$\frac{u}{u_\tau} \approx \frac{1}{\kappa}\ln\left(\frac{E\, y}{C_S\, K_S}\right)$$

Comparing the last expression to the (1.3) and considering that y and z are the wall normal coordinate in both cases results the equation (2.33).

$$\frac{1}{z_0} \approx \frac{E}{C_S\, K_S} \text{ or } C_S\, K_S \approx E\, z_0$$

APPENDIX C. FURTHER 2D DES CASES ON ROUGH WALLS

Both the sensitivity to the model constant C_{DES} and the four settings listed in Table 5.1 have been tested on rough walls. Velocity and SGS eddy-viscosity profiles are shown in Figure 6.7 and Figure 6.8. The constant C_{DES} influences clearly the position of the interface URANS/LES and the value of the SGS eddy-viscosity.

In Figure 6.9 and Figure 6.10 are plotted velocity profiles obtained with the four settings of Table 5.1.

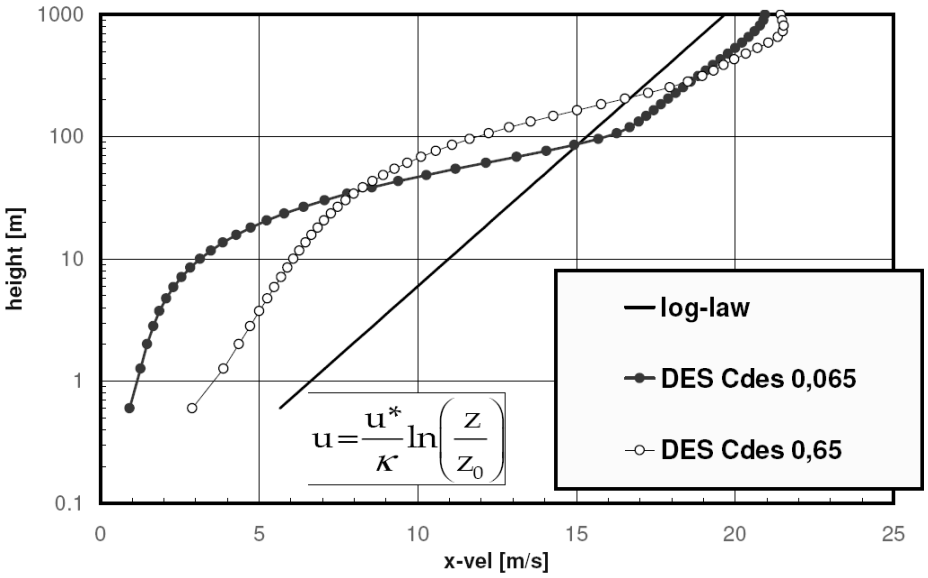

Figure 6.7 – vertical profiles of velocity, sensitivity to the C_{DES} constant.

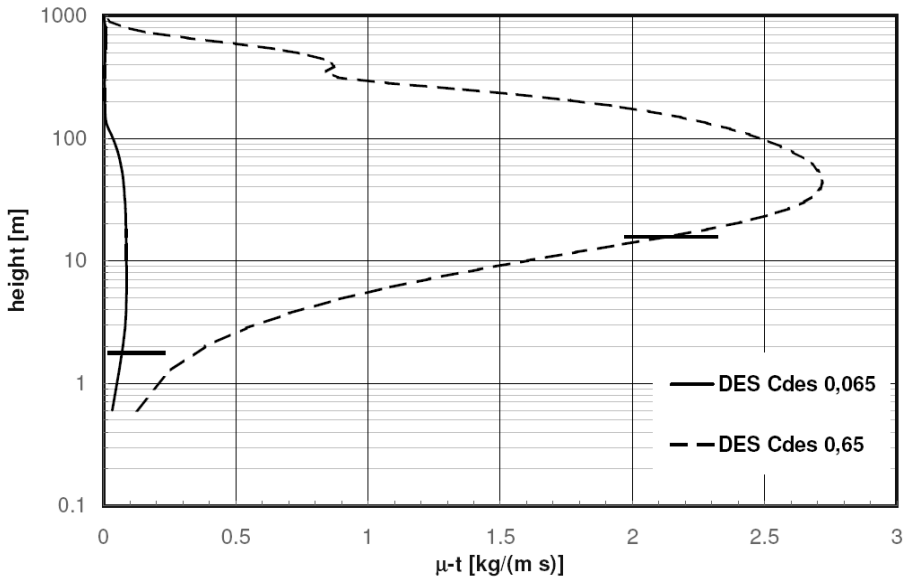

Figure 6.8 – vertical profiles of SGS eddy viscosity, sensitivity to the C_{DES} constant.

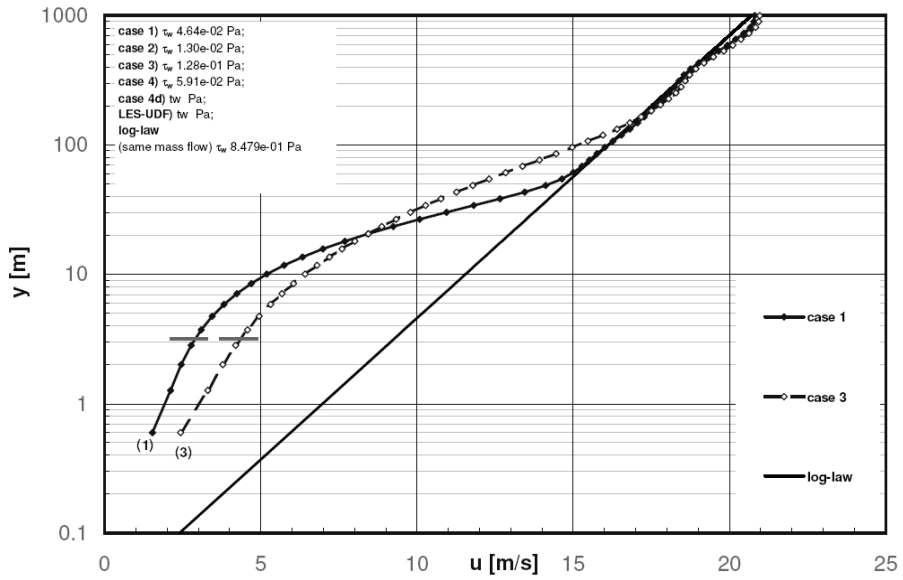

Figure 6.9 – velocity profiles for DES case 1 and 3.

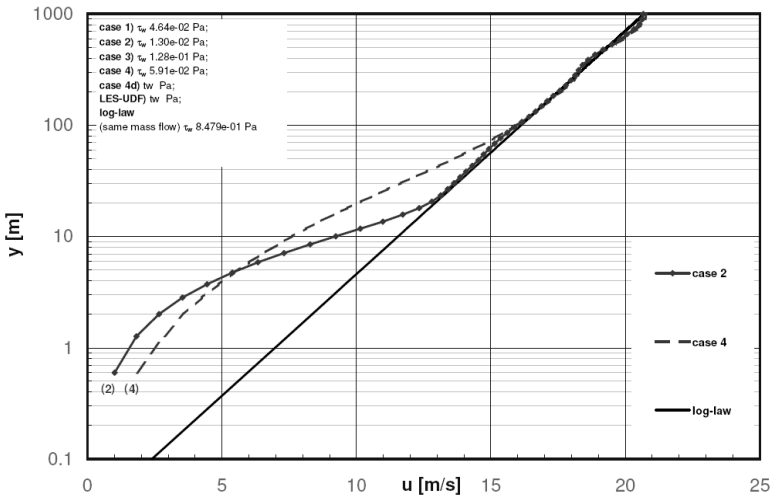

Figure 6.10 – velocity profiles for DES case 2 and 4.

APPENDIX D. LES-UDF TEXT

```
/************************************************************
UDF that specifies a standard Smagorinsky-Lilly SGS model

by Giorgio Crasto (DC 2005-2006) - 27th April 2006
************************************************************/

#include "udf.h"

DEFINE_TURBULENT_VISCOSITY(user_mu_t,c,t)
{
  real S;
  real Cs = 0.1;    /* Smagorinsky constant */
  real mu_t;
  real rho;
  rho = C_R(c,t);

/* S = sqrt (2 ( Sij * Sij ) ) */

#if RP_3D
  S = sqrt((
             (C_U_G(c,t)[1]+C_V_G(c,t)[0])*(C_U_G(c,t)[1]+C_V_G(c,t)[0])+
             (C_U_G(c,t)[2]+C_W_G(c,t)[0])*(C_U_G(c,t)[2]+C_W_G(c,t)[0])+
             (C_V_G(c,t)[2]+C_W_G(c,t)[1])*(C_V_G(c,t)[2]+C_W_G(c,t)[1])
             )+
            2*(
              (C_U_G(c,t)[0])*(C_U_G(c,t)[0])+
              (C_V_G(c,t)[1])*(C_V_G(c,t)[1])+
              (C_W_G(c,t)[2])*(C_W_G(c,t)[2])
              )) ;
#else
```

```
  S = sqrt((
            (C_U_G(c,t)[1]+C_V_G(c,t)[0])*(C_U_G(c,t)[1]+C_V_G(c,t)[0])
            )+
           2*(
             (C_U_G(c,t)[0])*(C_U_G(c,t)[0])+
             (C_V_G(c,t)[1])*(C_V_G(c,t)[1])
             )) ;
#endif

#if RP_3D
  mu_t = rho*pow(Cs,2.0)*pow(C_VOLUME(c,t),2.0/3.0)*S;
#else
  mu_t = rho*pow(Cs,2.0)*C_VOLUME(c,t)*S;
#endif

  /* real L_s = min;  mixing length */

  return mu_t;
}
```

APPENDIX E. COMPUTATION OF DRAG COEFFCIENTS C1 OF TABLE 6.7

First of all the optical porosity of the porous medium (Pine forest) has been considered equal to the volume porosity β. The value of C1 0,05 1/s is considered acceptable for the pine forest.

Now taking into account the definition of permeability by the Darcy's law itself:

$$\alpha = \frac{q \mu L}{A \Delta P}$$

Where, given a tube of flow of length L and cross sectional area A in a porous region, as sketched in Figure 11:

α	[m^2]	is the permeability;
q	[m^3/s]	is the flow rate;
μ	[Pa s]	is the dynamic viscosity;
ΔP	[Pa]	is the pressure drop along the length L

The ratio of the flow rate q to the cross sectional area A yields the Darcy's velocity or superficial velocity, while considering the porosity of the medium the interstitial or actual velocity, always space averaged, is given by the ratio of the superficial velocity to the porosity β.

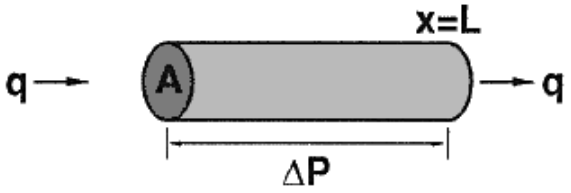

Figure 11 – sketch of a tube of flow in a porous media for the definition of the Darcy's law.

$U_{DARCY} = \frac{q}{A}$ Darcy's (or superficial) velocity

$U = \frac{U_{DARCY}}{\beta} = \frac{q}{\beta A}$ actual (or interstitial) velocity

A relation is proposed in order to link the permeability α to the porosity of the medium β:

$$\alpha = C\frac{\beta^2}{1-\beta^2}. \qquad \textbf{(AE.1)}$$

Where the following relation defining the drag coefficient C1 holds:

$$C1 = \frac{\beta\mu}{\rho\alpha}$$

Being:

α	[m^2]	the permeability;
β	[-]	the porosity;
μ	[Pa s]	the dynamic viscosity;
ρ	[kg/m^3]	the density;

According to the proposed equation when the porosity equals one (fluid cell) the permeability is infinite and drag coefficient zero, when the porosity is zero (solid cell) also the permeability equals zero and the drag coefficient is infinite.

Since for a pine forest (β = 0,38) the constant C1 is found to be around 0,05 1/s and assuming valid the equation (AE.1) the constant C is then calculated equal to 6,9529E-04 m^2, hence the values of C1 proposed in Table 6.7.